# Chiral description and physical limit of pseudoscalar decay constants with four dynamical quarks and applicability of quasi-Monte Carlo for lattice systems

D I S S E R T A T I O N

zur Erlangung des akademischen Grades

doctor rerum naturalium
(Dr. rer. nat.)
im Fach Physik

eingereicht an der
Mathematisch-Naturwissenschaftlichen Fakultät I
Humboldt-Universität zu Berlin

von
**Dipl.-Phys. Andreas Ammon, geb. Nube**

Präsident der Humboldt-Universität zu Berlin:
Prof. Dr. Jan-Hendrik Olbertz

Dekan der Mathematisch-Naturwissenschaftlichen Fakultät I:
Prof. Stefan Hecht, Ph.D.

Gutachter/innen:
1. Dr. habil. Karl Jansen
2. Prof. Dr. Michael Müller-Preußker
3. Prof. Constantia Alexandrou

**Tag der mündlichen Prüfung:** 13. Februar 2014

*Ich widme diese Arbeit*
*denen, die mir den Rücken freihielten, ...*
*... aber auch jenen, die mich ständig davon abhielten*

## Abstract

In this work, masses and decay constants of pseudoscalar mesons, like the pion or the $D_s$-meson, are determined in the framework of quantum chromodynamics (QCD), which is quantised through the path integral. As those quantities require a non-perturbative treatment of the path integral, we apply the lattice-QCD approach, a lattice regularised form of QCD, which is able to accomplish this.

Corresponding to this, we present our lattice-QCD calculation in the first part of this work as one of the first with four different sea quarks flavours, namely the up, down, strange and charm quark, leading to more realistic simulations of the strong interaction in comparison with simulations involving only two or three sea quark flavours. For the discretisation of the Dirac operator on the lattice we use the twisted mass approach, exhibiting the advantageous feature of $O(a)$-improvement. This amazing property leads to the cancellation of $O(a)$ discretisation effects in the lattice spacing $a$ for all physical observables.

For the estimation of the lattice spacing $a$ in our simulations we determined the pion mass $M_\pi$ and the decay constant $f_\pi$ in dependence of the average up/down quark mass and extrapolated $f_\pi$ to the physical point, identified by the ratio $f_\pi/M_\pi$ taking on its physical value. This extrapolation was performed using chiral perturbation theory ($\chi$PT) formulae [1], describing the specific discretisation effects of the twisted mass formulation. The determined results of $a(\beta = 1.9) = 0.0899(13)\,\text{fm}$, $a(\beta = 1.95) = 0.0812(11)\,\text{fm}$ and $a(\beta = 2.1) = 0.0624(7)\,\text{fm}$ are $\approx 5\%$ larger than previous determinations [2]. The high precision of our data enables us to study to a certain extent the range of up/down quark masses in which $\chi$PT at next-to-leading order correctly describes lattice-QCD results for $f_\pi$. We found that our data is described up to pion masses of about 300 MeV, or equivalently five times the physical average up/down quark mass. This is in good agreement with results obtained in [3].

The decay constant $f_{D_s}$ of the $D_s$-meson (a pseudoscalar meson consisting of a strange and a charm quark) is originally measured in units of $a$ in our lattice simulations. It is converted to physical units with the previously determined results for the lattice spacings. The physical limit of $f_{D_s}$ is studied, using formulae from heavy meson chiral perturbation theory. Our final result $f_{D_s} = 248.9(5.3)$ MeV lies slightly above previous lattice determinations [4] [5] and still about $2\sigma$ below the experimental average [6].

The basic observables required for the determination of meson masses and decay constants are pseudoscalar correlations functions. The neutral pion correlation function contains so-called disconnected contributions, which are hard to measure in practise due to large stochastic fluctuations. We suggest a new approach based on the quasi-Monte Carlo (QMC) method for the stochastic approximation of such contributions, which should theoretically be able to improve the asymptotic error behaviour to $O(N^{-1})$ in contrast to $O(N^{-\frac{1}{2}})$ found for conventional Monte Carlo methods, where $N$ is the number of samples.

This improved error behaviour of the QMC approach involves the potential to enormous reductions of computing resources, if this method could be applied to lattice-QCD simulations at some point. Hence, in the second part of this work, we point out important prerequisites necessary for the application of QMC for the stochastic estimation of disconnected contributions, and suggest that this method

could in general be applied to basically all fermionic observables involving disconnected parts, such as quark contents of the nucleon and flavour singlet quantities. An explicit application of QMC is demonstrated at the example of the harmonic oscillator, where we verified a perfect error scaling of $O(N^{-1})$. Going further to the anharmonic oscillator, we still find a strongly improved asymptotic error behaviour of $O(N^{-\frac{3}{4}})$. Next steps are discussed on the way to an establishing of the QMC method in lattice field theory.

## Zusammenfassung

In dieser Arbeit werden Massen und Zerfallskonstanten von pseudoskalaren Mesonen, wie z. B. dem Pion oder dem $D_s$-Meson, im Rahmen der Quantenchromodynamik (QCD) berechnet. Da diese Größen eine nicht störungstheoretische Behandlung des Pfadintegrals, das zur Quantisierung der Theorie verwendet wird, erfordern, wird die Methode der Gitter-QCD, eine gitter-regularisierte Form der QCD, angewendet um diese zu berechnen.

Im ersten Teil der Arbeit soll zu diesem Thema eine der ersten Gitter-QCD-Rechnungen vorgestellt werden die vier verschieden See-Quark-Arten, das Up-, Down-, Strange- und Charmquark, bei der Simulation des Eichfelds berücksichtigt. Dies führt zu einer wesentlich realistischeren Simulation der starken Wechselwirkung als vergleichbare Rechnungen mit nur zwei oder drei verschiedenen Quark-Arten. Die Diskretisierung der Fermionwirkung erfolgt mittels Twisted-Mass-Diracoperator. Dieser Ansatz bietet den außergewöhnlichen Vorteil der sog. $O(a)$-Verbesserung, welche wiederum dazu führt, dass Terme von $O(a)$ im Gitterabstand $a$ in allen physikalischen Observablen verschwinden.

Zur notwendigen Bestimmung des Gitterabstands $a$ der Gitter-Simulationen wurden Pion-Massen $M_\pi$ und -Zerfalsskonstanten $f_\pi$ in Abhängigkeit der gemittelten Up- und Down-Quark-Masse bestimmt und zum physikalischen Punkt, der durch den physikalischen Werte des Verhältnisses $f_\pi/M_\pi$ bestimmt ist, extrapoliert. Neuerlich entwickelter Formeln aus der chiralen Störungstheorie, die die speziellen Deskretisierungseffekte des Twisted-Mass-Formalismus berücksichtigen, ermöglichen eine solche Extrapolation. Die bestimmten Werte des Gitterabstands, $a(\beta = 1.9) = 0.0899(13)\,\mathrm{fm}$, $a(\beta = 1.95) = 0.0812(11)\,\mathrm{fm}$ und $a(\beta = 2.1) = 0.0624(7)\,\mathrm{fm}$, liegen etwa fünf Prozent über denen vorheriger Bestimmungen [2]. Die hohe Genauigkeit der Daten ermöglicht es in gewissem Umfang die Anwendbarkeit bezüglich des Bereiches der Up-/Down-Quark-Massen der Formeln aus der chiralen Störungstheorie (in nächst-führender Ordnung) zu überprüfen. Das Ergebnis dieser Untersuchung weist darauf hin, dass die Daten für die Pion-Zerfallskonstante bis zu Pionmassen von etwa 300 MeV, bzw. etwa bis zum Fünffachen der mittleren physikalischen Up- und Down-Quark-Masse beschrieben werden. Dieses Ergebnis stimmt gut mit anderen Untersuchungen überein [3].

Die Zerfallskonstante $f_{D_s}$ des $D_s$-Mesons (pseudoskalares Meson bestehend aus je einem Strange- und Charm-Quark) wird zunächst in Einheiten von $a$ bestimmt. Mit Hilfe der vorher bestimmten Ergebnisse des Gitterabstands kann diese in physikalischen Einheiten ausgedrückt werden. Zur Untersuchung des physikalischen Grenzwertes von $f_{D_s}$ werden Formeln der chiralen Störungstheorie für schwere Mesonen (vgl. heavy meson chiral perturbation theory) eingesetzt. Das Endergebnis dieser Betrachtung $f_{D_s} = 248.9(5.3)$ MeV liegt ein wenig über vorherigen Bestimmungen [4] [5] und immernoch etwa zwei Standardabweichungen unter dem Mittel aus experimentellen Werten [6].

Pseudoskalare Korrelationsfunktionen sind die grundlegenden Observablen der QCD, wenn es um die Bestimmung von Meson-Massen und -Zerfallskonstanten geht. Die dem ungeladenen Pion entsprechende Korrelationsfunktion enthält sog. unverbundene Beiträge, die die Berechnung dieser Größe durch die starken, statisch bedingten Schwankungen schwierig gestalten. In dieser Arbeit wird eine neue Methode der stochastischen Näherung solcher unverbundenen Beiträge vorgestellt, welche auf

der sog. Quasi-Monte-Carlo-Methode (QMC-Methode) beruht. Mit dieser Methode sollte es zumindest theoretisch möglich sein das asymptotische Fehlerverhalten auf $O(N^{-1})$ (im Gegensatz zu $O(N^{-\frac{1}{2}})$ für übliche Monte-Carlo-Methoden) zu verbessern, wenn $N$ Stichproben zugrunde gelegt werden.

Ein derartig verbessertes Verhalten des Fehlers könnte zu gewaltigen Einsparungen in der Rechenzeit führen, wenn die QMC-Methode letztlich auch auf Gitter-QCD-Simulationen angewendet werden könnte. Daher soll im zweiten Teil dieser Arbeit zunächst dargestellt werden, welche weiteren Schritte nötig sind um die QMC-Methode auf die Berechnung von unverbunden Beiträgen anzuwenden. Darüberhinaus wird darauf hingewiesen, dass diese Methode prinzipiell auf jegliche Art fermionischer Observablen, wie z.B. Quark-Inhalte des Nukleon und Flavour-Singulett-Zustände, angewendet werden kann die insbesondere unverbundene Beiträge enthalten. Eine direkte Anwendung der QMC-Methode soll anhand des harmonischen und anharmonischen Oszillators vorgeführt werden. Für den harmonischer Oszillator wurde tatsächlich das bestmögliche Fehlerverhalten von $O(N^{-1})$ gefunden. Im Fall des anharmonischen Oszillators konnte ebenfalls ein deutlich verbessertes asymptotische Verhalten des Fehlers von $O(N^{-\frac{3}{4}})$ festgestellt werden. Es werden weitere Schritte besprochen, die auf eine breitere Anwendung der QMC-Methode für gitterregularisierte Quantenfeldtheorien abzielen.

# Contents

**Introduction** **1**

**1. Theoretical basis** **5**
1.1. Twisted mass lattice-QCD . . . 5
1.1.1. Twisted mass fermion action . . . 5
1.1.2. Symmetries of the twisted mass fermion action . . . 7
1.1.3. Mixed action setup . . . 10
1.2. Observables . . . 10
1.2.1. The physical basis . . . 11
1.2.2. Interpolating fields for pions . . . 12
1.2.3. Estimation of disconnected contributions to the neutral pion correlator . . . 13
1.2.4. Strange and charmed mesons . . . 16
1.2.5. Meson masses and decay constants . . . 16
1.2.6. The Sommer scale $r_0$ . . . 18
1.3. Meson masses and decay constants in the chiral limit . . . 18
1.3.1. Results of continuum $\chi$PT . . . 19
1.3.2. Results of twisted mass Wilson $\chi$PT . . . 20
1.3.3. Chiral behaviour of $f_{D_s}$ . . . 21
1.4. Analysis methods . . . 22
1.4.1. Error analysis of correlated observations . . . 22
1.4.2. Curve fitting and $\chi^2$-minimisation . . . 25
1.4.3. The p-value . . . 25
1.4.4. Implementation as R-Package . . . 27

**2. Setting the lattice scale** **29**
2.1. Simulation parameters . . . 30
2.2. Relative scale setting with $r_0$ . . . 31
2.3. Analysis of the charged pseudoscalar correlator . . . 34
2.4. Scale setting from chiral fits to $f_\pi$ and $M_\pi$ . . . 37
2.4.1. Construction of the $\chi^2$ function . . . 37
2.4.2. Results . . . 39

**3. Determination of $f_{D_s}$ in the physical limit** **53**
3.1. Tuning of the sea strange and charm quark mass . . . 54
3.2. Measurement of meson masses and decay constants . . . 56
3.3. Extrapolation of $f_{D_s}$ to the physical point . . . 57

**4. Lattice simulations with quasi-Monte Carlo: an applicability study** **67**
4.1. Quasi-Monte Carlo samples are "more uniform" . . . . . 68
4.2. The harmonic and anharmonic oscillator on the lattice . . . . . 72
4.2.1. Observables . . . . . 74
4.3. Gaussian sampling in the QMC approach . . . . . 75
4.3.1. Generation algorithm for lattice paths . . . . . 75
4.4. Numerical results . . . . . 76
4.4.1. Harmonic oscillator . . . . . 77
4.4.2. Anharmonic oscillator . . . . . 78
4.5. Outlook and conclusions . . . . . 82

**Conclusions** **85**

**Danksagung** **87**

**A. Conventions** **89**
A.1. Euclidean gamma matrices . . . . . 89
A.2. Generators of $SU(2)$ . . . . . 89
A.3. Notation . . . . . 90
A.3.1. Covariant vectors . . . . . 90
A.3.2. Covariant unit vectors . . . . . 90
A.3.3. Fermion fields . . . . . 90

**B. Tables of measured masses and decay constants of pseudoscalar mesons** **91**
B.1. Pion Masses and Decay Constants . . . . . 91
B.2. Unitary Kaon and D-meson masses . . . . . 92

**C. Fit parameters of chiral fits to $\Phi_{D_s}$ and $R_1$** **93**

**D. Calculation of the error behaviour of $\chi^2_\lambda$** **95**

**Bibliography** **107**

# Introduction

The investigation of quantum chromodynamics (QCD) as the candidate theory for the description of the strong interaction, which is one of four fundamental forces in our universe in the context of the standard model, is a very important task. QCD allows the theoretical prediction of values for a large manifold of physical quantities which appear almost in our everyday life, like the proton mass, but also more elaborate observables, such as hadronic contributions to the muon anomalous magnetic moment, that can only be determined from highly specialised experiments at particle accelerators.
Due to the confinement of quarks, a unique but yet to be proven feature of QCD, the calculation of certain observables like meson masses, meson decay constants and the previously mentioned quantities require a non-perturbative approach, which does not rely on an expansion in the strong coupling constant $\alpha_s$. At distances of $O(1\text{ fm})$ this coupling constant becomes so large (of $O(1)$) that a series arising from a perturbative expansion would not converge anymore.
A very powerful non-perturbative method that has been established since several decades is the lattice regularisation of QCD in Euclidean space, commonly referred to as lattice-QCD. This is a very computation-intense approach, and therefore strongly relies on well developed computer hardware, software and numerical algorithms.
An important aspect of a lattice-QCD calculation is the lattice geometry, and especially the number of lattice points. Two conditions have to be taken into account. First, due to the finite lattice spacing $a$ the simulated physical spatial volume $V = L^3$ is restricted by the finite number of lattice points[1]. If we imagine a particle represented through a plane wave, with (Compton-)wavelength $\lambda$, it should be straightforward to understand the requirement that the spatial extent $L$ should be several times larger than $\lambda$ to correctly reflect the dynamics of this particle. As the pion is the lightest stable particle (with the largest Compton wavelength $\lambda_\pi \sim (M_\pi)^{-1}$) in QCD[2] it should govern the selection of $L$. Typically, $L$ should be at least four times larger[3] than $\lambda_\pi$: $\frac{L}{\lambda_\pi} > 4$. The other important requirement is the smallness of the lattice spacing $a$, as this strongly influences the size of discretisation effects and is crucial for studying and taking the limit $a \to 0$, the continuum limit, which is absolutely mandatory to obtain physical results. Demonstrating these requirements at a specific example with $a = 0.1$ fm, we find that the number of lattice points $\frac{L}{a}$ should be at least 48, when a pion mass of $M_\pi = 140$ MeV should be simulated. Such lattice sizes have been entirely unfeasible to simulate in the past, and hence, one could only do simulations with unphysically large pion masses. This however, required an extrapolation of the results to the physical pion

[1] being $L/a$ in one spatial direction for a Cartesian lattice.
[2] neglecting effects from other fundamental forces
[3] We will motivate this choice later in chapter 2.

mass of $M_\pi \approx 140$ MeV. Advances in computer hardware and simulation algorithms made it possible to simulate larger and larger physical volumes, such that only today high statistics runs at physical pion masses and reasonably small lattice spacings $a$ can be performed.

Another important aspect making a lattice-QCD simulation more realistic is the consideration of more than only the two light quark flavours, up and down. If one investigates for example mesons containing a strange and a charm quark, like the $D_s$-meson, it seems an obvious question whether virtual strange and charm quark loops could also lead to significant contributions to the dynamics inside such a meson, and hence, to its basic properties like the mass or its decay constant.

This work addresses several topics with respect to the aforementioned aspects. New theoretical results from chiral perturbation theory ($\chi$PT) [1], specially suited for our lattice fermion action, will be used to better describe our data (meson mass and decay constant) with respect to the dependence on the pion mass[4] and the lattice spacing[5] $a$, and enables us to perform an improved extrapolation to the physical pion mass. Furthermore, we will determine the decay constant of the $D_s$-meson in a setup involving, additionally to the up and down quark, also virtual strange and charm quark loops contributing to the strong interaction processes inside hadrons. Furthermore, also a contribution to the algorithmic development, that has been so important for the advances in this field until now, should be presented in this work. Hence, we suggest a new approach, involving the application of an innovative Monte Carlo like technique, the quasi-Monte Carlo method, for the calculation of disconnected diagrams that arise from certain observables like the neutral pion mass and many other interesting quantities (see below). The possible profits that could be obtained from a successful realisation of this proposal motivates us to investigate the quasi-Monte Carlo Method in more detail, although this will happen at the example of clearer models.

According to the previous discussion, the thesis is structured as follows.

In the first part of this thesis, to which basically chapters 1 to 3 are dedicated, we present the determination of meson masses and decay constants, in particular also the $D_s$-meson decay constant, from a lattice-QCD simulation with four dynamical quark flavours, the up, down, strange and charm quark. To our knowledge this is one of the first approaches carrying out this kind of investigation for such a physical situation. From the side of algorithmic developments, presented mainly in chapter 4 and in a smaller part in section 1.2.3 of chapter 1, we started to investigate a Monte Carlo like technique, the quasi-Monte Carlo method (QMC), which is theoretically able to improve the asymptotic error behaviour of observables stemming form such a simulation to $O(N^{-1})$, when $N$ is the number of observations. This is in great contrast to conventional Monte Carlo methods where only rates of $O(N^{-\frac{1}{2}})$ can be achieved. Practically this means that one would need only a *tenth* of the samples to achieve an additional digit of accuracy under optimal conditions. To make it even more clear - this improvement does not lead to a fixed factor speedup but a speedup factor growing like $\sqrt{N}$ with the number of samples.

[4] or equivalently the average up/down quark mass

[5] such dependencies could arise from discretisation effects

Hence, it should be obvious that the QMC approach has the potential for tremendous reductions in computing time, if it can eventually be applied to lattice-QCD.
Among the different possibilities to discretise the Dirac operator on the lattice we have chosen the twisted mass approach, which has the intriguing feature of automatic $O(a)$-improvement at maximal twist[6]. A basic introduction to this approach is given in chapter 1, including the simulation of mass-degenerate (up and down quark) and non-mass-degenerate (strange and charm) quarks (sec. 1.1) and the discussion of subtleties involved in the formulation of pseudoscalar meson correlation functions. Observables important in the context of this work, namely various pseudoscalar meson correlation functions, the corresponding masses and decay constants, and the Sommer scale $r_0$ are discussed in section 1.2. In connection with the discussion about the neutral pion correlation function, involving the evaluation of so-called dis-connected contributions, we suggest a new method for the stochastic approximation of these disconnected contributions to this quantity. This is a method involving the application of the QMC approach (sec. 1.2.3). Furthermore, we introduce formulae from $\chi$PT and heavy meson chiral perturbation theory (HM-$\chi$PT), which we use to describe our data in dependence of the average up/down quark mass, and allow us to extrapolate to the physical point (sec. 1.3). At the end of this chapter we also discuss a basic but very important set of statistical and numerical methods for the analysis of our data. These are basically two different error analysis methods for correlated data sets, the method of least-squares, the p-value and a fast minimisation technique suitable to efficiently perform fits of curve (sec. 1.4).
Another important aspect of nature is the lightness of the up and down quark compared to the other quarks which are at least $\approx 27$ times heavier. In $\chi$PT, an effective field theory describing QCD in the limit of small quark masses and small momenta, the mass of the pion is directly related to the masses of the up and down quark. Today, it is possible to perform simulations with a physical pion mass[7] of 134.8 MeV [3] (and hence physical up and down quark masses). As the lattice spacing $a$ can be obtained from the pion decay constant $f_\pi$ at the physical pion mass (or moreover at the point where the ratio $f_\pi/M_\pi$ takes on its physical value), $a$ is determined almost trivially if the lattice simulation is carried out directly *at* the physical point. This was demonstrated in [3], and did not require any chiral extrapolation[8] for the reason we just mentioned. This is different, however, in our case, as our data comes only down to $\approx 2.5$ times the physical average up/down quark mass. Hence, we discuss in chapter 2 our procedure for the scale setting based on chiral extrapolations through $\chi$PT descriptions of the pion mass and decay constant. While doing this, we motivate in hindsight the importance of simulations with up/down quark masses at the physical point by demonstrating the difficulties of such an extrapolation.
As indicated above, our setup allows the consideration of the strange and charm quark mass as sea quarks. With this we aim at a more realistic simulation of the strong interaction physics inside pseudoscalar mesons and other hadrons, which could lead to

[6] the term "maximal twist" will be explained in chapter 1

[7] This is not the experimental pion mass. As our setup does not consider quantum electrodynamics and a mass splitting between up and down quarks this pion mass is corrected for these effects [7].

[8] an extrapolation in the average up/down or equivalently in the squared pion mass

significant contributions for example to the decay constant $f_{D_s}$ of the $D_s$-meson that have been neglected in previous determinations with only up and down ($N_f = 2$, [4]) or up, down and strange ($N_f = 2 + 1$, [5]) quarks. We will discuss in chapter 3 the measurement of various pseudoscalar meson masses and decay constants (sec. 3.2), which are then used for the continuum and chiral extrapolation of $f_{D_s}$ (sec. 3.3) after we outlined the tuning of the sea strange and charm quark mass (sec. 3.1).
Chapter 4 is then devoted to explicit applications of the QMC method, where we initiate our investigations with simple models, namely the quantum mechanical harmonic and anharmonic oscillator. We review the respective lattice actions in section 4.2, followed by a straightforward algorithm for the direct sampling of harmonic oscillator lattice paths. This knowledge will be used to apply the QMC method directly for the calculation of observables (sec. 4.4). Finally, we come back to a discussion about the next important steps towards the application of the QMC method in lattice-QCD.
In a final conclusion (pp. 85) we summarise our findings for all the topics discussed in this work.

# 1. Theoretical basis

## 1.1. Twisted mass lattice-QCD

The calculation of masses and decay constants of pseudoscalar mesons requires a non-perturbative treatment of QCD, because such properties become important in a regime where the strong coupling constant is large. Correspondingly, one has to apply a non-perturbative regularisation scheme during the quantisation of QCD. A very successful approach performing this is lattice-QCD, and is based on the path integral quantisation. Although the basic idea to discretise space-time is very straightforward, there are some subtleties about the choice of the discretisation of the lattice-Dirac operator.
In this work we are using the twisted mass lattice approach for the formulation of the fermion action. This approach has the intriguing property of automatic $O(a)$-improvement for physical observables. This only comes at the expense of the tuning of just one parameter. The purpose of this section is the introduction of the three twisted mass actions, which are used for the description of two mass-degenerate (up/down sea-quark), two mass-non-degenerate (charm/strange sea-quark) and two freely selectable valence quarks (describing the constituents of the investigated mesons).

### 1.1.1. Twisted mass fermion action

The lattice-QCD approach requires naturally the introduction of a lattice. This can be, in the most general case, a set of points with connections to nearest neighbours in four-dimensional space-time. However, in this work we use a rather convenient choice, namely an equidistant Cartesian lattice on a four-dimensional hypercube with extent $T$ in time direction and lengths $L_{x,y,z}$ in the spatial directions. This lattice has $N_0$ and $N_{1,2,3}$ number of points in time and space direction. The discrete set of lattice points $\mathcal{X}$ can be expressed through the following expression:

$$\mathcal{X} = \{x = a(n^0, n^1, n^2, n^3) \mid n^\mu \in \{0, \ldots, N_\mu - 1\}\} \,, \tag{1.1}$$

where $a = \frac{T}{N_0} \equiv \frac{L_x}{N_1} \equiv \frac{L_y}{N_2} \equiv \frac{L_z}{N_3}$ is the distance between two neighbouring points. We imply anti-periodic (periodic) boundary conditions in time (spatial) direction for the fermion fields. The action for two mass-degenerate quark flavours, describing the up and down quarks in our setup, is then given by:

$$S_F^{(tm),l} = a^4 \sum_{x,y \in \mathcal{X}} \bar{\chi}^l(x) K^{(tm),l}(x,y) \chi^l(y) \,. \tag{1.2}$$

In this expression $K^{(tm),l}$ is the Wilson twisted mass Dirac operator:

$$K^{(tm),l}(x,y) = D_W(x,y)\tau^0 + (m_0\tau^0 + i\mu_q\gamma_5\tau^3)\delta_{x,y}\ , \quad \text{with} \tag{1.3}$$

$$D_W(x,y) = \sum_\mu \gamma_\mu \frac{1}{2a}\left(\delta_{x+a\hat{\mu},y} - \delta_{x-a\hat{\mu},y}\right) - \frac{r}{2a}\left(\delta_{x+a\hat{\mu},y} + \delta_{x-a\hat{\mu},y} - 2\delta_{x,y}\right). \tag{1.4}$$

$m_0$ and $\mu_q$ are the bare and the twisted quark mass in units of the lattice spacing and $r$ the Wilson parameter, which is usually and actually set to one. $\gamma_\mu$ are the Euclidean gamma matrices and are given in appendix A.1. $\tau^0$ and $\tau^3$ are the zeroth and the third Pauli matrix, defined in section A.2, and both act in flavour space. As the up and down quark masses are identical in our setup we will refer to them as light quarks in the following. Hence, we also put the index "l" on the action, the kernel $K$, and the fermion fields $\chi$. The unit vectors $\hat{\mu}$ and $\hat{\nu}$ are defined with other conventions in section A.3.

The untwisted subtracted quark mass $m_q = m_0 - m_{cr}$ is obtained by additive renormalison with $m_{cr}$, as described in [8] . $m_{cr}$ can be defined as the point where the PCAC mass vanishes. The PCAC (partially conserved axial current) mass appears in a Ward identity relating the pseudoscalar and the axial current and can be considered as a rather simple quantity to compute in an actual lattice simulation.
The actual (unrenormalised) mass of the simulated quarks is controlled by the two mass parameters $m_q$ and $\mu_q$ in form of the so called polar mass:

$$M = \sqrt{m_q^2 + \mu_q^2}\ . \tag{1.5}$$

This results in the fact that the overall quark mass can be split up freely on $\mu_q$ and $m_q$ (in quadrature). Now, the motivation for using twisted mass-QCD goes back to the observation that discretisation effects[1] of $O(a)$ in all physical observables do vanish when $m_q$ is set to zero [8], at least within an accuracy of $O(a)$ [9]. The vanishing of $O(a)$ terms in observables is highly desirable when one wants to study the continuum limit ($\lim_{a\to 0}$) of them. The freedom in the choice of $m_q$ and $\mu_q$, given a fixed polar mass $M$, can be exploited to choose $\mu_q = M$ and $m_q = 0$, meaning that the actual quark mass is described completely by the twisted mass term.
Correspondingly, in all simulations, the parameter $m_0$ can be tuned to $m_{cr}$ for the $O(a)$-improvement to take effect. As indicated before, such a tuning can be performed through the measurement of the PCAC mass and is very straightforward. Our criterion for a proper tuning is the requirement

$$\frac{m_{PCAC}}{\mu_q} < 0.1\ , \tag{1.6}$$

meaning that $m_{PCAC}$, the PCAC mass, has to be a tenth of the twisted mass. If this has been achieved, one is in the situation of maximal twist, and the action (1.2) describes a doublet of quarks, each with a mass of $\mu_R = \mu_q Z_\mu$, $Z_\mu = Z_P^{-1}$ being the twisted quark

[1] discretisation effects linear in the lattice spacing

mass renormalisation factor, and $Z_P$ the renormalisation factor[10] of the pseudoscalar density[2] $P$.
For the description of the charm and strange quark, we slightly modify (1.2), and define the action for a doublet with two different quark masses:

$$S_F^{(tm),h} = a^4 \sum_x \bar{\chi}^h(x) K^{(tm),h} \chi^h(x) \ , \tag{1.7}$$

$$K^{(tm),h} = D_W(x,y)\tau^0 + i\mu_\sigma \gamma_5 \tau^3 + \mu_\delta \tau^1 \ . \tag{1.8}$$

It can be shown that the critical mass parameter $m_{cr}$ is the same as for the light quark action (1.2) [10]. The simulated renormalised strange ($\mu_s$) and charm ($\mu_c$) quark masses are:

$$\mu_s = \frac{1}{Z_P}\mu_\sigma - \frac{1}{Z_S}\mu_\delta \quad \text{and} \tag{1.9a}$$

$$\mu_c = \frac{1}{Z_P}\mu_\sigma + \frac{1}{Z_S}\mu_\delta \ , \tag{1.9b}$$

with $Z_S$ being the renormalisation constant of the scalar density, also described in [10]. Compared to the light quarks the strange and charm quarks are much heavier. This is the reason why they are often referred to as heavy quarks (hence the superscript $h$ in (1.7)).
The gauge field on the lattice is implemented as parallel transporters $U_\mu(x) \in SU(3)$, defined on the link between two neighbouring lattice sites $x$ and $x + a\hat{\mu}$. For the gauge action we choose the Iwasaki gauge action [11]. The fermion actions (1.2) and (1.7) can be made gauge invariant by the following replacements:

$$\bar{\chi}(x)(r - \gamma_\mu)\chi(x + a\hat{\mu}) \quad \rightarrow \quad \bar{\chi}(x)U_\mu(x)(r - \gamma_\mu)\chi(x + a\hat{\mu}) \ , \tag{1.10}$$

$$\bar{\chi}(x)(r + \gamma_\mu)\chi(x - a\hat{\mu}) \quad \rightarrow \quad \bar{\chi}(x)U_\mu^\dagger(x - a\mu)(r + \gamma_\mu)\chi(x - a\hat{\mu}) \ . \tag{1.11}$$

In the next section we will discuss two important symmetries of continuum QCD, which are broken unintentionally in the lattice theory with twisted mass quarks, as it was indicated already in the introduction.

### 1.1.2. Symmetries of the twisted mass fermion action

The discussion in this section will be very important in the following and is based in significant parts on this review [10] about "Twisted mass lattice QCD" by A. Shindler. Especially the problem of kaon-D-meson mixing and the mixing with the parity-even partners, the $K_0^*$ and the $D_0^*$, as well as the pion-mass-splitting, a problem we are faced with in lattice QCD simulations with twisted mass quarks, is directly related to the topic of this section. In conjunction with this, we motivate the so called mixed action setup, discussed in 1.1.3 as a way out of the flavour mixing in the heavy quark sector, which leads to the aforementioned unwanted mixing of the various mesons states.

[2] $P$ will be defined in section 1.2.

The knowledge about the symmetries of the fermion action is important for the construction of operators suitable for the measurement of physical particle properties like meson masses and decay constants. Such operators should be constructed to represent conserved quantum numbers (e.g. isospin, parity or angular momentum) of the regularised continuum theory.
Conversely, if a quantum number like strangeness or charm, for example, would not be conserved on the lattice, a mixing between the kaon and the D-meson states, represented by pseudoscalar densities with the corresponding quark content, could occur. These kaon or D-meson states are then not the physical ones, because such a mixing is not observed in nature, and we refer to them as lattice-kaon or lattice-D-meson state. Within a suitable scheme (see [12]) one can perform a diagonalisation in the space of these lattice states to recover the physical states from the condition that the physical states should not mix among each other. The physical kaon state would then be a linear combination of the lattice-kaon and lattice-D-meson state.
Note that in addition not only the flavour symmetry, but also parity is not conserved. Correspondingly, the space of states from which the physical states are extracted has to involve the parity-even (scalar) states additionally.

### Flavour symmetry

The massive continuum QCD Lagrangian describing two mass-degenerate quark flavours is invariant under the non-singlet vector transformation

$$SU_V(2) = \begin{cases} \chi(x) \to e^{-i\frac{\pi}{4}\gamma_5\tau^3} e^{i\sum_{a=1,2,3}\frac{\alpha_a^V}{2}\tau_a} e^{i\frac{\pi}{4}\gamma_5\tau^3}\chi(x) \\ \bar{\chi}(x) \to \bar{\chi}(x) e^{i\frac{\pi}{4}\gamma_5\tau^3} e^{-i\sum_{a=1,2,3}\frac{\alpha_a^V}{2}\tau_a} e^{-i\frac{\pi}{4}\gamma_5\tau^3} \\ (\alpha_1^V, \alpha_2^V, \alpha_3^V)^T \in \mathbb{R}^3 \, . \end{cases} \tag{1.12}$$

It is obtained from the vector transformation in the physical basis [3]

$$SU_V(2) = \begin{cases} \psi(x) \to e^{i\sum_{a=1,2,3}\frac{\alpha_a^V}{2}\tau_a}\psi(x) \\ \bar{\psi}(x) \to \bar{\psi}(x) e^{-i\sum_{a=1,2,3}\frac{\alpha_a^V}{2}\tau_a} \end{cases} \quad (\alpha_1^V, \alpha_2^V, \alpha_3^V)^T \in \mathbb{R}^3 \, , \tag{1.13}$$

by a transformation (see eqn. (1.17)) to the twisted basis fields $\chi$, the fields we used to construct the twisted mass action. We will discuss the physical basis in more detail in subsection 1.2.1.

The vector symmetry is not respected by the twisted mass actions (1.2) and (1.7). Although, it is important to note that (1.2), the action describing the light quarks, is

[3] which is the vector transformation in their standard form

invariant under a reduced vector transformation:

$$[U_V(1)]_3 = \begin{cases} \chi \to e^{-i\frac{\pi}{4}\gamma_5\tau^3} e^{i\frac{\alpha^V}{2}\tau_3} e^{i\frac{\pi}{4}\gamma_5\tau^3}\chi \\ \bar{\chi} \to \bar{\chi} e^{i\frac{\pi}{4}\gamma_5\tau^3} e^{-i\frac{\alpha^V}{2}\tau_3} e^{-i\frac{\pi}{4}\gamma_5\tau^3} \end{cases} \quad , \quad \alpha^V \in \mathbb{R} \, , \tag{1.14}$$

resulting in the conservation of the third component of the isospin.

### Parity symmetry

Another important symmetry of continuum QCD is the parity symmetry. On the lattice the parity transformation can be defined as

$$\mathcal{P} = \begin{cases} U_0(x_0, \mathbf{x}) \to U_0(x_0, -\mathbf{x}), U_k(x_0, \mathbf{x}) \to U_k^{-1}(x_0, -\mathbf{x} - a\hat{k}) \\ \chi(x_0, \mathbf{x}) \to \gamma_0 \chi(x_0, -\mathbf{x}) \\ \bar{\chi}(x, \mathbf{x}) \to \bar{\chi}(x_0, -\mathbf{x})\gamma_0 \end{cases} . \tag{1.15}$$

This transformation however, is not conserved in the given form by the twisted mass actions. But one can define modified versions of (1.15) involving discrete flavour rotations and sign changes of the twisted mass parameters $\mu_q$, $\mu_\sigma$ and $\mu_\delta$, that leave the actions (1.2) and (1.7) invariant. For details see [10].

### Consequences

From the remnant vector symmetry $[U(1)]_3$ one can deduce, that the charged and the neutral pion sector do not mix with each other but they can acquire different masses. An indication for this could be seen in the fact that the charged pions are described by pseudoscalar densities whereas the neutral one is described by the scalar density[4].
It was indicated before that one has to expect a mixing of $K^\pm$, $D^\pm$, $K_0^*$ and $D_0^*$ lattice states. Now we saw in more detail that this is originated in the breaking of parity and flavour symmetry. Several techniques have been developed to reconstruct quantitatively the mixing mechanism and with this the physical kaon and D-meson states, allowing a determination of their masses and decay constants. The results can be found in [12]. In this work we want to use a different approach however, which will be discussed in the next section.
Finally, it is important to note that the breaking of certain symmetries is just a discretisation effect, and should not lead to any other than the continuum fermion action of QCD (with two light, a strange and a charm quark) in the limit $a \to 0$. It was shown [10] that these discretisation effects are only present at $O(a^2)$ and higher orders, such that any terms of $O(a)$ are absent in all physical observables, meson masses and decay constants being among them.

[4] When mentioning densities we refer to corresponding densities constructed from the quark fields $\chi$ in the twisted basis. The relation of the twisted and the physical basis will be discussed below in subsection 1.2.1.

The mixing of $\pi^+$ and $\pi^-$ does not signal a problem, because their properties are identical from the QCD point of view. It is the mass offset of the neutral pion from the charged ones what disturbs, for example, the precise description of the quark mass and finite volume dependence of the pion mass in chiral fits. But recently more suitable $\chi$PT formulae have been developed describing exactly the special form of discretisation effects of the twisted mass action. This makes it possible to better describe the lattice data with respect to the pion mass splitting.
A cure for the strange-charm mixing will be presented in the next subsection.

### 1.1.3. Mixed action setup

In this section, we want to describe an approach for avoiding the flavour mixing of heavy quarks in the valence[5] sector.
In a unitary setup one would introduce external currents coupling to the fermion fields in the actions (1.2) and (1.7) for the construction of fermionic operators for the description of mesons, baryons or any other kind of hadrons. As mentioned in the last section, such operators would lead to undesired mixing effects with other operators representing different particles with different quantum numbers or the same particle in an excited state. In order to avoid such undesired effects one can introduce a different action designed solely for the description of valence quarks. Such a description should be flavour-diagonal and hence, should not lead to any flavour mixing effects apriori. An action with this property for two valence quarks would be defined as

$$S_F^{(tm),f} = a^4 \sum_x \bar{\chi}(x) \left[ (D_W(x,y) + m_0)\tau^0 + i\gamma_5 \begin{pmatrix} \mu_1 & 0 \\ 0 & -\mu_2 \end{pmatrix} \right] \chi(y) \,, \tag{1.16}$$

with the field $\chi = (q_1, q_2)^T$ describing two quark flavours with freely selectable masses $\mu_1$ and $\mu_2$. The case of maximum twist is achieved by using the same critical mass as in the sea quark action (1.2). With a suitable choice of the quark masses it is possible to construct interpolating fields suitable for the measurement of masses and decay constants for a range of mesons, among them the $\pi^\pm$ ,the $K^\pm$ , the $D^\pm$ and the $D_s^\pm$.
As the previously defined twisted mass actions (1.2) and (1.7) the observables measured with this action are automatically $O(a)$-improved, as it was shown in [13], where also other properties and details of this action are discussed. The specific strategy for the construction of pseudoscalar meson annihilation and creation operators will be discussed in the next section.

## 1.2. Observables

In this section we want to summarise the important observables which are needed in following parts of this work. Meson correlation functions are necessary for the measure-

[5] Valence quarks are the constituents of hadrons. They are the counterparts to the sea quark fields, which only appear in the fermion action in the Boltzmann factor inside the path integral.

ment of meson masses and decay constants, and are discussed in subsection 1.2.2. In this context we will take a closer look at the determination of the neutral pion-correlation function in subsection 1.2.3. This consideration will guide us to the second major topic of this work, addressed in chapter 4, where we suggest a new method, the quasi-Monte Carlo-approach(QMC), for the numerical evaluation of disconnected diagrams. We will demonstrate the new approach for two toy models, namely the quantum mechanical harmonic and anharmonic oscillator. In subsection 1.2.6 we will introduce the Sommer scale $r_0$, which will be used to determine ratios of lattice scales among our different lattices. This is necessary for the extraction of precise lattice scales from $\chi$PT fits (see section 1.3).

### 1.2.1. The physical basis

The measurement of properties of physical particles requires the construction of operators having a non-vanishing projection on the states describing such particles. Suitable operators are so called interpolating fields, and have to be formulated in terms of the fermion fields $\psi$ in the physical basis. This is a basis formally defined for the light fermion fields as

$$\psi^l = \begin{pmatrix} u^{(phys)} \\ d^{(phys)} \end{pmatrix} = e^{i\frac{\pi}{4}\gamma_5\tau^3}\chi^l \tag{1.17}$$

$$\bar{\psi}^l = (\bar{u}^{(phys)}, \bar{d}^{(phys)}) = \bar{\chi}^l e^{i\frac{\pi}{4}\gamma_5\tau^3} \ . \tag{1.18}$$

In continuum QCD this transformation with the corresponding transformation of the Dirac operator, would define the transition from the twisted mass fermion action (at maximal twist) to the ordinary fermion action where the twisted mass term is absent and replaced by the standard quark mass term $m\bar{\psi}\psi$. On the lattice the situation is slightly different. The axial rotation (1.17) does not only transform the mass terms into each other, but also parts of the lattice Dirac operator, namely the Wilson term responsible for the removing of doublers[6]. Hence, the lattice action obtained after the transformation does not only differ in the mass terms, but also in the discretisation of the Dirac operator. At this point we will not go further into the details of the results of the axial rotation at finite lattice spacing. The reader may be referenced to [8] and [10] for further reading. We want to continue with the definition of operators responsible for the creation and annihilation of mesons.
The interpolating fields for pseudoscalar mesons are basically given by the pseudoscalar density $\mathcal{P}^a$, but for completeness we also mention other important quark field bilinears, like the scalar $\mathcal{S}^0$, the vector $\mathcal{V}^a_\mu$ and the axial vector current $\mathcal{A}^a_\mu$:

$$\mathcal{S}^0(x) = \bar{\psi}^l(x)\psi^l(x) \quad , \qquad \mathcal{P}^a(x) = \bar{\psi}^l(x)\gamma_5\frac{\tau^a}{2}\psi^l(x) \ , \tag{1.19}$$

$$\mathcal{V}^a_\mu(x) = \bar{\psi}^l(x)\gamma_\mu\frac{\tau^a}{2}\psi^l(x) \quad , \qquad \mathcal{A}^a_\mu(x) = \bar{\psi}^l(x)\gamma_\mu\gamma_5\frac{\tau^a}{2}\psi^l(x) \ , \tag{1.20}$$

[6] For a description of the fermion doubling problem see for example [14], "the Rothe".

defined for $a = 1, 2, 3$. The corresponding densities in the twisted basis, $S^0$, $P^a$, $V^a_\mu$ and $A^a_\mu$ are defined in the same way

$$S^0(x) = \bar{\chi}^l(x)\chi^l(x) \quad , \qquad P^a(x) = \bar{\chi}^l(x)\gamma_5\frac{\tau^a}{2}\chi^l(x) \; , \tag{1.21}$$

$$V^a_\mu(x) = \bar{\chi}^l(x)\gamma_\mu\frac{\tau^a}{2}\chi^l(x) \quad , \qquad A^a_\mu(x) = \bar{\chi}^l(x)\gamma_\mu\gamma_5\frac{\tau^a}{2}\chi^l(x) \; , \tag{1.22}$$

and also for $a = 1, 2, 3$. Finally, one can express $\mathcal{P}^a$ in terms of $P^a$ and $S^0$:

$$\mathcal{P}^a(x) = \begin{cases} P^a(x) & (a = 1, 2) \\ \frac{i}{2}S^0(x) & (a = 3) \end{cases} \tag{1.23}$$

### 1.2.2. Interpolating fields for pions

For the description of the pions we have chosen the interpolating fields[7] in the following formula:

$$\mathcal{P}^+(x) = \mathcal{P}^1(x) - i\mathcal{P}^2(x) \tag{1.24}$$

$$\mathcal{P}^-(x) = \mathcal{P}^1(x) + i\mathcal{P}^2(x) \tag{1.25}$$

$$\tilde{\mathcal{P}}^3(x) = \sqrt{2}\mathcal{P}^3(x) \; , \tag{1.26}$$

representing the charged pions, $\pi^+$ and $\pi^-$, and the neutral pion $\pi^0$ respectively. These interpolating fields can be written directly in terms of the up and down component of twisted basis field $\chi^l = (u, d)^T$:

$$\mathcal{P}^+(x) = \bar{d}(x)\gamma_5 u(x) \tag{1.27}$$

$$\mathcal{P}^-(x) = \bar{u}(x)\gamma_5 d(x) \tag{1.28}$$

$$\tilde{\mathcal{P}}^3(x) = \frac{i}{\sqrt{2}}(\bar{u}(x)u(x) + \bar{d}(x)d(x)) \; . \tag{1.29}$$

The charged and the neutral pion correlation function (correlator) is defined as:

$$C_{\pi^\pm}(x_0) = -\sum_{\vec{x}}\langle 0|\mathcal{P}^+(x)\mathcal{P}^-(0)|0\rangle \tag{1.30}$$

$$C_{\pi^0}(x_0) = -\sum_{\vec{x}}\langle 0|\tilde{\mathcal{P}}^3(x)\tilde{\mathcal{P}}^3(0)|0\rangle \; . \tag{1.31}$$

The sum over the spatial components performs the projection on zero meson momentum (cf. rest mass). In the next subsection we will look in more detail at the numerical evaluation of the neutral pion correlator (1.31).

[7] A very good review on the construction of interpolating fields was given in this reference [15].

### 1.2.3. Estimation of disconnected contributions to the neutral pion correlator

In this subsection we want to take a closer look to the neutral pion correlator, for which it is in practice quite difficult to obtain a precise estimate. This originates from the fact that $C_{\pi^0}$ involves disconnected contributions visible in the explicit expression for $C_{\pi^0}$ in terms of the light fermion propagator

$$C_{\pi^0}(x_0) = \frac{1}{2}\sum_{\vec{x}} \left\{4\,\mathrm{Re}\,\mathrm{Tr}[S^u(x,x)]\,\mathrm{Re}\,\mathrm{Tr}[S^u(0,0)] - 2\,\mathrm{Re}\,\mathrm{Tr}\left[S^u(x,0)S^u(0,x)\right]\right\} \ . \quad (1.32)$$

The trace is taken over the spinor and colour indices. The up quark propagator $S^u$ is obtained from the upper left component in the flavour structure decomposition of the full fermion propagator.

$$S^{(tm),l} = (K^{(tm),l})^{-1} = \begin{pmatrix} D_W + m_0 + i\mu\gamma_5 & 0 \\ 0 & D_W + m_0 - i\mu\gamma_5 \end{pmatrix}^{-1}_{\text{flavour}} \quad (1.33)$$

$$\equiv \begin{pmatrix} S^u & 0 \\ 0 & S^d \end{pmatrix} . \quad (1.34)$$

The light quark propagator $S^{(tm),l}$ is the inverse of the twisted mass Dirac operator (1.3). Instead of the origin ($x = (0,0,0,0)$) as reference point in the correlator (1.32) one could have chosen any other point with zero time component $y = (0,\vec{y})$. We can account for this fact by averaging over all possible choices:

$$C_{\pi^0}(x_0) = \frac{1}{2}\frac{1}{V}\sum_{\vec{x}} 4\,\mathrm{Re}\,\mathrm{Tr}[S^u(x,x)]\sum_{\vec{y}}\mathrm{Re}\,\mathrm{Tr}[S^u((0,\vec{y}),(0,\vec{y}))] \quad (1.35)$$

$$-\frac{1}{2}\frac{1}{V}\sum_{\vec{x},\vec{y}} 2\,\mathrm{Re}\,\mathrm{Tr}\left[S^u(x,(0,\vec{y}))S^u((0,\vec{y}),x)\right] \ ,$$

where $V = N_1N_2N_3$ is the number of lattice points of the spatial volume. The first term is the disconnected contribution representing two closed fermion loops at different space-time points. At tree-level of perturbation theory, there would be no source of correlation from such a term. In the interacting theory however, there could be interactions stemming purely from the gluon field in the space around the fermion loops which would connect the loops.

If the disconnected contribution in (1.35) has to be estimated, one is faced with two major sources of statistical fluctuations. Usually the propagators appearing in (1.35) can not be calculated directly but have to be estimated stochastically. This introduces naturally a certain stochastic noise. The second source of noise comes from the fluctuation of the gauge field itself, and cannot be avoided. Thus, it is desirable to reduce the statistical errors from the stochastic approximation of the propagators as much as possible, and at least as much as the fluctuations arising from the gauge fields.

A typical approach for the stochastic estimation of $S^u(x,y)$ is the following:

$$\tilde{S}^R(x,y) = \frac{1}{R}\sum_{r=1}^{R}\sum_{z} S(x,z)\xi^r(z)\left(\xi^r(y)\right)^* \ . \tag{1.36}$$

We dropped the superscript $u$ on $S$ here and in the following, because $S$ could be also the down quark propagator or any other kind of propagator that needs to be estimated. $\tilde{S}^R$ represents the stochastic estimate of $S$ based on $R$ samples. $\xi^r(x)$ are $R$ complex random vectors, also called sources, with stochastically independent components of unit variance obeying the following relation:

$$\lim_{R\to\infty}\frac{1}{R}\sum_{r=1}^{R}\xi^r(x)\left(\xi^r(y)\right)^* = \delta_{x,y} \ . \tag{1.37}$$

This property is also referred to as white noise because the power spectrum, obtained from a four-dimensional Fourier transformation, of the vectors $\xi^r$ shows the presence of all possible modes with equal amplitudes[8] (on average). Apart from the mentioned requirements, the probability density function (PDF) of each source component can be chosen freely. In some approaches one tries to find clever choices for the PDF, exhibiting faster convergence rates (as the normal distribution for example) when the limit in equation (1.37) is taken.

But there is a general problem, intrinsic to almost every conventional stochastic approximation method, that we want to discuss in the following.

To simplify the discussion we consider a d-dimensional positive definite Hermitian matrix[9] $M$ instead of the propagator. $M$ can be written in terms of its positive eigenvalues $\lambda_k$, in decreasing order ($\lambda_1 > \ldots > \lambda_d$) and orthonormal eigenvectors $v^k$:

$$M_{i,j} = \sum_{k=1}^{d}\lambda_k v_i^k (v_j^k)^* \tag{1.38}$$
$$i,j = 1,\ldots,d \ .$$

Now, we can construct a unitary transformation $V$ by taking the eigenvectors $v$ as the columns of $V$. Then $V$ can be simply express as $V_{i,j} = v_i^j$, and equation (1.38) could also be written as $M = V\Lambda V^\dagger$, if $\Lambda$ is a diagonal matrix constructed from all eigenvalues $\lambda_i$ in the order corresponding to the eigenvectors in $V$.

If we approximate $M$ stochastically as in (1.36) under the usage of (1.38) we obtain:

$$\tilde{M}_{i,l}^R = \frac{1}{R}\sum_{r=1}^{R}(V\Lambda V^\dagger)_{i,j}\xi_j^r(\xi_l^r)^* \ , \text{with} \tag{1.39}$$

[8] like a mixture of light with all possible frequencies and equal intensities (as perceived by our eyes) appears as white light

[9] Such a matrix could be constructed as $M = S^\dagger S$ from the fermion propagator $S$.

with the random vectors $\xi_j^r$ fulfilling the relation

$$\lim_{R\to\infty} \frac{1}{R} \sum_{r=1}^{R} \xi_j^r \, (\xi_k^r)^* = \delta_{j,k} \; , \tag{1.40}$$

analogous to (1.37). As a toy problem we want to consider the trace of $M$, respectively the trace of its stochastic approximation $\tilde{M}^R$, a problem constructed to exhibit some similarity to the estimation of disconnected contributions to the neutral pion correlation function (1.35).

$$\mathrm{Tr}\tilde{M}^R = \sum_i \tilde{M}_{i,i}^R \tag{1.41}$$

$$= \frac{1}{R} \sum_{r=1}^{R} \sum_k \Lambda_{k,k} \sum_j V_{j,k}^* \xi_j^r \sum_i (\xi_i^r)^* V_{i,k} \tag{1.42}$$

$$= \frac{1}{R} \sum_{r=1}^{R} \sum_k \Lambda_{k,k} (V^\dagger \xi^r)_k (V^\dagger \xi^r)_k^* \tag{1.43}$$

The sum over $i$ and $j$ can be interpreted as a unitary transformation of the vectors $\xi^r$ as explained in the last step. Hence, we obtain with the definition $\xi^{'r} = V^\dagger \xi^r$

$$\mathrm{Tr}\tilde{M}^R = \frac{1}{R} \sum_{r=1}^{R} \sum_k \lambda_k \xi_k^{'r} (\xi_k^{'r})^* = \frac{1}{R} \sum_{r=1}^{R} \sum_{k=1}^{d} \lambda_k |\xi_k^{'r}|^2 \; . \tag{1.44}$$

As a unitary transformation leaves (1.40) invariant, this relation is also fulfilled by the transformed vectors $\xi^{'r}$, resulting in the fact that the components of $\xi^{'r}$ will be statistically independent (uncorrelated) if the components of $\xi^r$ were statistically independent. (1.44) can be interpreted as a stochastic evaluation of the expectation value of a weighted $\chi^2$-distribution, which is defined as follows

$$\chi_\lambda^2 = \lambda_1 X_1^2 + \lambda_2 X_2^2 + \ldots \lambda_d X_d^2 \; . \tag{1.45}$$

In this formulation of the problem we can directly trace back the origin of the overall stochastic fluctuation of $\chi_\lambda^2$ to the fluctuations of the individual variables $X_i$.

In a standard Monte Carlo evaluation all variables are sampled independently of each other such that no regard is taken to the overall fluctuation of the quantity of interest. Moreover, the generation of new samples happens independently of all the previously generated samples. Hence, it often occurs that new samples are generated close to existing samples. These two effects could be taken as an explanation for the rather slow convergence rate of the statistical error of $\chi_\lambda^2$. A detailed calculation, which can be found in the appendix D, reveals that the asymptotic error behaviour of $\chi_\lambda^2$ is proportional to $\frac{1}{\sqrt{R}}$ if one uses $R$ stochastic samples $(\xi^r)_{r=1\ldots R}$.

Quite recently, we started to investigate [16] a new approach for the sampling in the $d$-dimensional space, namely the quasi-Monte Carlo (QMC) technique. For general re-

views on this topic see for example [17] [18]. Within this approach the set of generated samples is distributed more uniformly[10] over the sampled region, and therefore addresses exactly the aforementioned effects which led to the slow error convergence. It can be shown that the QMC method can improve the asymptotic error behaviour to $O(\frac{1}{R})$ in the present case described above for Gaussian variables $X_i$ and the problem of stochastically estimating $\chi^2_\lambda$.
We will illustrate a bit more the differences between standard Monte Carlo and quasi-Monte Carl sampling in chapter 4 and will investigate the application of the QMC approach for two interesting physical models, namely the quantum mechanical harmonic and anharmonic oscillator, which do both take profit of the beneficial properties.
For the moment, we want to come back to the discussion of interpolating fields for mesons containing strange and charm quarks.

### 1.2.4. Strange and charmed mesons

As mentioned earlier, we will use the mixed action setup approach for the description of the kaon, the D-meson and the $D_s$-meson. The underlying valence quark action was discussed in subsection 1.1.3 . The interpolating fields are constructed quite similarly as in subsection 1.2.2. Any meson is represented by the pseudoscalar densities

$$\mathcal{P}^+_{mixed}(x) = \bar{q_2}\gamma_5 q_1 \quad \text{and} \tag{1.46}$$
$$\mathcal{P}^-_{mixed}(x) = \bar{q_1}\gamma_5 q_2 \ . \tag{1.47}$$

The corresponding correlation function is

$$C_{mixed}(x_0) = -\sum_{\vec{x}} \langle 0|\mathcal{P}^+_{mixed}(x)\mathcal{P}^-_{mixed}(0)|0\rangle \ . \tag{1.48}$$

This correlator depends on the quark mass values $\mu_1$, representing the up(down)[11] or strange quark mass, and $\mu_2$, representing the strange or charm quark mass, in the valence quark action (1.16). We list in the table 1.1 how the certain mesons are mapped to the quark masses one has to use to obtain them.

### 1.2.5. Meson masses and decay constants

Pseudoscalar meson masses and decay constants are obtained theoretically from the infinite time behaviour and practically from the large time behaviour of pseudoscalar correlators. What can be considered as sufficiently large times will be discussed in

[10] The consequences of the improved uniformity of QMC samples will be illustrated in chapter 4. For the detailed mathematical meaning of this property the reader is referred to the literature, for example [17] and [18], as the discussion of this goes far beyond the scope of this work.
[11] The actual formulation does not distinguish between up and down quark, coming from the fact that electric charge and mass-non-degeneracy is disregarded.

| meson | $\mu_1$ | $\mu_2$ |
|---|---|---|
| $\pi^{\pm}$ | $m_{up/down}$ | $m_{up/down}$ |
| $K^{\pm}$ | $m_{up/down}$ | $m_{strange}$ |
| $D^{\pm}$ | $m_{up/down}$ | $m_{charm}$ |
| $D_s^{\pm}$ | $m_{strange}$ | $m_{charm}$ |

Table 1.1.: This table shows the mapping of mesons to quark mass values $\mu_1$ and $\mu_2$ in the valence quark action (1.16). $m_{up/down}$, $m_{strange}$ and $m_{charm}$ correspond to the up/down, strange and charm quark mass.

chapter 2, section 2.3. Generally, one can consider a pseudoscalar correlator

$$\begin{aligned} C_{\mathcal{PP}}(x_0) &= \sum_{\vec{x}} \langle 0|\mathcal{P}^{\dagger}(x)\mathcal{P}(0)|0\rangle \\ &= \sum_{\vec{x}} \sum_{n} \frac{1}{2E_n} \langle 0|\mathcal{P}^{\dagger}(x)|n(p)\rangle\langle n(p)|\mathcal{P}(0)|0\rangle \end{aligned} \tag{1.49}$$

with a pseudoscalar density $\mathcal{P}(x)$ describing a certain pseudoscalar meson $\mathcal{M}$ of mass $M_{\mathcal{M}}$. This expression has been rewritten (second line of (1.49)) with the insertion of a complete set of states $|n(p)\rangle$ with a certain four-momentum $p = (E_n, p_x, p_y, p_z)^T$ and the same quantum numbers as the operator $\mathcal{P}$. The sum over all spatial lattice points $\vec{x}$ performs the projection to zero spatial momentum $\vec{p} = (p_x, p_y, p_z) = (0, 0, 0)$. In the limit of large times, depicted by $\lim_{t\to\infty}$, only the projection to the ground state $|\mathcal{M}\rangle$, the meson $\mathcal{M}$, survives. On the other hand, $f_{\mathcal{M}}$, the decay constant of the pseudoscalar meson $\mathcal{M}$, is define in the framework of QCD through

$$\langle 0|\mathcal{A}_{\mu}(x)|\mathcal{M}(p)\rangle = -if_{\mathcal{M}}p_{\mu}e^{-ipx} \,, \tag{1.50}$$

with $\mathcal{A}_{\mu}$ chosen to represent the correct isospin, strangeness and charm quantum number corresponding to the meson $\mathcal{M}$. With support of the PCAC relation, valid also for a quark doublet with different masses $\partial_{\mu}\mathcal{A}_{\mu} = (\mu_1 + \mu_2)\mathcal{P}$. One can reexpress (1.49) as

$$C_{\mathcal{PP}}(x_0) = \lim_{x_0\to\infty} \frac{(m_{\mathcal{M}}^2 f_{\mathcal{M}})^2}{2m_{\mathcal{M}}(\mu_1 + \mu_2)^2} e^{-x_0 M_{\mathcal{M}}} \,, \tag{1.51}$$

taking the zero momentum projection into account. The meson mass and decay constant can be extracted from a fit of the form of (1.52), with parameters $A$ and $B$ to be determined. It follows however from the periodicity of the lattice, that the pseudoscalar correlator on the lattice is rather described by formula (1.53).

$$C_{\mathcal{PP}}(x_0) \sim Ae^{-Bx_0} \tag{1.52}$$

$$C_{\mathcal{PP}}(x_0) \sim A(e^{-Bx_0} + e^{B(x_0-T)}) \tag{1.53}$$

Finally, we want to discuss a gauge field observable that has the dimension of a length and is highly sensitive to the lattice scale, namely $r_0$. It allows to build up dimensionless quantities, where the explicit scale dependence has been eliminated, and which can hence be compared across different lattice scales.

### 1.2.6. The Sommer scale $r_0$

The Sommer scale $r_0$ [19] is a physical length, which can be determined in a straightforward way in a lattice-QCD simulation. It is defined through the distance at which the force $F(r)$ between a static[12] quark-anti-quark pair with distance $r$ acquires a predefined value. $r_0$ is defined through the following condition

$$r_0^2 F(r_0) = 1.65 \; . \tag{1.54}$$

The force $F$ is determined from the (dimensionless)[13] potential $V(r)$ by $F(r) = -V'(r)$. The potential $V(r)$ is determined from Wilson loops $W(r,t)$ which are basically averages over products of closed loops of gauge links (see for example [14],[20]) along rectangles with spatial extent $r$ and time extent $t$. From the asymptotic time behaviour

$$W(r,t) \overset{t\to\infty}{\sim} e^{-tV(r)} \tag{1.55}$$

one can extract the potential at a discrete set of distances[14]. The force is basically the derivative of the potential. As such a derivative cannot be evaluated on a point-wise defined function, one has to perform an interpolation of $V(r)$ in the region around $r_0$, and then takes the derivative of this interpolation. A typical heuristic model suitable for such applications is given by

$$V(r) = -\frac{c}{r} + \sigma r \; . \tag{1.56}$$

A fit to this function gives estimates for $C$ and $\sigma$ and one can calculate $r_0$. Practically, we will use $r_0$ for the determination of lattice scale ratios, which are required to compare physical observables like masses in lattice units from simulations with different lattice spacings. This is a necessary prerequisite for the chiral fits that we will perform in chapter 2. The corresponding formulae will be presented in the next section.

## 1.3. Meson masses and decay constants in the chiral limit

The lattice simulations on which this work is based have been carried out with light quark masses 2.5 to 11 times larger than the physical average up/down quark mass. It is necessary therefore, to extrapolate any results to the physical point, which can be defined by the physical ratio of the pion mass and decay constant. This procedure is

[12] meaning that the quarks are not moving because their mass goes to infinity
[13] In the following we will assume that all quantities are expressed in units of the lattice spacing.
[14] The lattice geometry only allows a finite set of spatial and time-like separations.

particularly important for the scale setting. In the following subsections we will give an overview of the most important chiral perturbation theory ($\chi$PT) predictions describing the chiral behaviour of pion masses and decay constants.

### 1.3.1. Results of continuum $\chi$PT

Chiral perturbation theory is an effective field theory describing the interactions of particles which would arise as Goldstone bosons of QCD with massless quarks. These Goldstone bosons emerge when the chiral symmetry (of massless QCD) is broken spontaneously. Experiments indicate that nature is described by QCD with non-vanishing quark masses. This can be taken into account by an expansion in terms of the quark masses and small momenta, and allows the description of quantities at finite quark masses. It is however unclear to which point such an expansion is valid. We will consider anyhow only the up and down quark as light enough to be described by $\chi$PT. This is what is commonly called $SU(2)$-$\chi$PT because one considers a two-flavour chiral symmetry in contrast to $SU(3)$-$\chi$PT where also the strange quark is considered as light. Quite recently, in the works [3] and [21], an explicit verification of the validity range of $\chi$PT with respect to the light quark mass $m_{ud}$ has been carried out and it was found that the $\chi$PT expression for the pion decay constant at next-to-leading order (NLO) is valid up to 5 times the physical light[15] quark mass, or equivalently up to pion masses of $M_\pi = 300$ MeV. The next-to-leading order (NLO) expressions for $f_\pi$ and $M_\pi^2$ are [22]

$$f_\pi = f_0(1 - 2\xi \ln \frac{\chi_\mu}{\Lambda_4^2} + O(\xi^2)) \tag{1.57a}$$

$$M_\pi^2 = \chi_\mu(1 + \xi \ln \frac{\chi_\mu}{\Lambda_3^2} + O(\xi^2)) \; . \tag{1.57b}$$

We are using the normalisation in which $f_\pi = 130.4$ MeV. $\chi_\mu = 2Bm_{ud}$ is the squared leading-order (LO) pion mass. $\xi = \frac{\chi_\mu}{(4\pi f_0)^2}$ is the expansion parameter in SU(2)-$\chi$PT. $B$,$f_0$ and $\Lambda_{3,4}$ are low energy constants (lec) meaningful only in the context of the effective field theory. They can be determined by fitting appropriate data[16], obtained for example from a lattice simulation, to the formulae (1.57). $f_0$ is the pion decay constant in the chiral limit ($m_{ud} \to 0$). $B$ and $f_0$ can be related to the chiral condensate:

$$\Sigma = Bf_0^2 = -\langle \bar{q}q \rangle \tag{1.58}$$

which is the order parameter of chiral symmetry breaking in QCD.

#### Finite size effects

In an actual lattice calculation one is restricted in the number of lattice points. Furthermore, one can only simulate at a finite lattice spacing. Both restrictions limit the

[15] assuming that up and down quark have the same mass

[16] data allowing to acquire information about the light quark mass dependence of the pion mass and decay constant

maximal size of the physical volume of the simulation. Correspondingly, all quantities are obtained with a dependence on the length $L$ of the spatial volume $V = L^3$. This dependence can be described as well in the framework of $\chi$PT. The relative shift of the pion mass and decay constant to NLO is given by [23]:

$$R_{M_\pi} = \frac{M_\pi^2(L)}{M_\pi^2} = 1 + \xi \tilde{g}_1(L, \xi) \tag{1.59}$$

$$R_{f_\pi} = \frac{f_\pi(L)}{f_\pi} = 1 - 2\xi \tilde{g}_1(L, \xi)\ . \tag{1.60}$$

$M_\pi(L)$ and $f_\pi(L)$ are the corresponding quantities at finite volume. $\tilde{g}_1$ is a function defined in [23]. The formulae presented in this subsection can only describe the effect of explicit breaking of chiral symmetry by the quark masses. In our lattice action we have additional terms breaking chiral and isospin symmetry. Although these terms vanish in the continuum limit, they lead to finite contributions at non-vanishing lattice spacing. We will present formulae taking into account these effects in the next subsection.

### 1.3.2. Results of twisted mass Wilson $\chi$PT

The presence of chiral symmetry and isospin symmetry breaking terms in the lattice-QCD Lagrangian results in a breakup of the mass degeneracy of the isospin triplet $(\pi^-, \pi^0, \pi^+)$ and $O(a^2)$-terms in the chiral expansion. A remnant of the chiral symmetry in the light sector (see section about symmetries) ensures the symmetry of the charged sector $(\pi^+, \pi^-)$. The neutral pion however, could acquire a mass different from the charged ones. This results in the fact that the LO expression for the charged and neutral pion mass is different:

$$M_\pm^2 = \chi_\mu \tag{1.61}$$

$$M_0^2 = \chi_\mu + 2c_2 a^2\ . \tag{1.62}$$

$\chi_\mu$ is defined as in the previous subsection. $c_2$ is an additional low energy constant which was first determined for our lattice setup in [24]. It is intersting to note that the NLO expressions for the *charged* pion quantities $f_{\pi^\pm}$ and $m_{\pi^\pm}$ contain also (exclusively) the LO *neutral* pion mass as expansion parameter. Oliver Bär derived explicitly the following formulae in his work [1]:

$$f_{\pi^\pm} = f_0 \left(1 - \frac{1}{(4\pi f_0)^2}\left(M_\pm^2 \ln \frac{M_\pm^2}{\Lambda_4^2} + M_0^2 \ln \frac{M_0^2}{\Lambda_4^2}\right) + C_f a^2\right) \tag{1.63}$$

$$M_{\pi^\pm}^2 = M_\pm^2 \left(1 + \frac{M_0^2}{(4\pi f_0)^2} \ln \frac{M_0^2}{\Lambda_3^2} + C_{M_\pm} a^2\right)\ . \tag{1.64}$$

$B$ (in $\chi_\mu$), $f_0$ and $\Lambda_{3,4}$ are the same low energy constants as in (1.57). He also derived an expression for the neutral pion mass which was measured in our simulations, enabling

us to check explicitly the correct description of this quantity.

$$M_{\pi^0}^2 = M_\pm^2 \left(1 + \frac{1}{(4\pi f_0)^2}\left(2M_\pm^2 \ln\frac{M_\pm^2}{\Lambda_3^2} - M_0^2 \ln\frac{M_0^2}{\Lambda_3}\right)\right) + 2c_2 a^2 \left(1 - 4\frac{M_0^2}{(4\pi f_0)^2}\ln\frac{M_0^2}{\Xi^2} + C_{M_0} a^2\right) \tag{1.65}$$

The constants $C_{M_\pm}$, $C_{M_0}$ and $C_f$ account for the $O(a^2)$ chiral symmetry breaking effects. We will see in chapter 2 how the formulae above perform in the description of our lattice data and help in the extrapolation to the physical point. This is a cornerstone in our scale determination as we have to determine as exact as possible the point where $f_\pi/M_\pi$ attains its physical value.

#### Finite size effects

Again one can study how the formulae (1.63) to (1.65) can be modified for describing the physics in a finite volume. In the same work where these formulae where derived the author suggest to do the following replacements in any of the chiral logarithms

$$\ln\frac{M^2}{\Lambda^2} \to \ln\frac{M^2}{\Lambda^2} + \tilde{g}_1(ML)\ . \tag{1.66}$$

for accounting of finite size effects at NLO of $\chi$PT. $M$ stands for $M_\pm$ or $M_0$ and $\Lambda$ for $\Lambda_{3,4}$ or $\Xi$.
In the last part of this section we will show how the discretisation effects and the chiral behaviour of the $D_s$ meson decay constant can be described for obtaining its value in the physical limit.

### 1.3.3. Chiral behaviour of $f_{D_s}$

$SU(2)$ heavy meson chiral perturbation theory (SU(2)-HM-$\chi$PT) approach is used for the chiral extrapolation of our lattice data for $f_{D_s}$ to the physical point. This approach has already been applied to data from simulations with two dynamical quarks (see [4] and [25]).
It is useful to consider the quantity $\Phi_{D_s} = f_{D_s}\sqrt{M_{D_s}}$ for which the first two terms of the expansion in HM-$\chi$PT are a constant and $M_{D_s}^{-1}$, the inverse $D_s$-meson mass. Furthermore one has to incorporate discretisation effects, the chiral extrapolation in the light quark mass and dependencies on the valence strange quark mass. One can establish the following formula describing all the aforementioned effects:

$$\Phi_{D_s} = D_1\left[1 + D_2\xi + D_a a^2 + D_{ah} a^2 M_{D_s}^2\right] + \frac{D_3}{M_{D_s}}\ . \tag{1.67}$$

$D_1$,$D_2$ and $D_a$ are considered linear functions of $\xi_{ss} = \frac{2Bm_s}{(4\pi f_0)^2}$, a variable proportional to the strange quark mass $m_s$. $D_3$ is as ordinary scalar parameter, and has to be determined from the lattice data. The advantage of this description is the rather flat chiral behaviour.

The weak point is the necessity for a precise knowledge of the discretisation artifacts. Another possibility, avoiding this problem, is the consideration of the quantity $R_1 = \frac{f_{D_s}\sqrt{M_{D_s}}}{f_K}$ which one aims to describe by the following formula:

$$R_1 = D_1 \left(1 + A_1 a^2 + A_2 a^2 M_{D_s}\right) \left(1 + \frac{3}{4}\xi \ln \xi + D_2 \xi\right) + \frac{D_3}{M_{D_s}} \,, \tag{1.68}$$

from [25]. $D_1$ and $D_2$ contain again a linear dependence on the strange quark mass. An advantage of this approach is the probable cancellation or at least smallness of discretisation effects. On the other hand $f_K$ strengthens the chiral behaviour of $R_1$, making it necessary to describe the dependence on the light quark mass more accurately. The results of the two extrapolation strategies will be used to check the consistency and the systematic error of the extrapolation result.

## 1.4. Analysis methods

### 1.4.1. Error analysis of correlated observations

The hybrid Monte Carlo algorithm (HMC), used widely in the lattice-QCD community to evaluate the path integral, is a Markov chain-Monte Carlo method. It lies in the nature of this algorithm to produce samples of certain observables which are correlated among each other in Monte Carlo-time. For example, one has to analyse $n$ observations $(x_i)_{i=1\ldots n}$ of an observable $x$, described as a random variable with mean $\mu$. $\mu$ can be estimated with the average estimator

$$\bar{x} = \frac{1}{n}\sum_{i=1}^{n} x_i \,. \tag{1.69}$$

The true error of the estimate is simply $|\bar{x} - \mu|$ . In lack of the knowledge of $\mu$ one can utilise the standard error for an approximation instead

$$\Delta\bar{x} = \sqrt{\frac{\mathrm{Var}(\bar{x})}{n}} = \frac{1}{\sqrt{n}}\sqrt{\sum_{i,j=1}^{n} \mathrm{Cov}(x_i, x_j)} \,. \tag{1.70}$$

When all observations have the same variance $\sigma$ and are not correlated, such that

$$\mathrm{Cov}(x_i, x_j) = \sigma^2 \delta_{ij} \;;, \tag{1.71}$$

one arrives at the simple expression for the error

$$\Delta\bar{x} = \frac{\sigma}{\sqrt{n}} \,. \tag{1.72}$$

On the other hand, if the covariance of the measurements does not vanish and (1.71) is correspondingly not fulfilled one underestimates the error by using (1.72). Basically

two different approaches have been developed to correctly calculate the error estimate (1.70). Both methods exploit the fact that all measurements have the same variance and that their covariance decays, often exponentially, with Monte Carlo time.

### Autocorrelation function based estimators

The first family of methods, one of them called the Γ-method, discussed in [26] and used frequently in the lattice community, directly tries to estimate the covariance matrix from the input data. In [27] it was already explained in detail how the variance of the mean estimator $\sigma^2(\bar{x})$ could be estimated from the correlation function $c_t$:

$$\sigma^2(\bar{x}) \approx \left\langle \frac{c_0 + 2\sum_{t=1}^{T}(1-\frac{t}{n})c_t}{n - 2T - 1 + \frac{T(T+1)}{n}} \right\rangle , \tag{1.73}$$

where

$$c_t = \frac{1}{n-t}\sum_{k=1}^{n-t}(x_k - \bar{x})(x_{k+t} - \bar{x}) \tag{1.74}$$

is an estimator of $\mathrm{Cov}(x_k, x_{k+t})$. The $\approx$ sign is due to neglecting a contribution, called $\Delta_t$ in [27], to the bias of $c_t$ with respect to $\sigma_t^2$.
The value of the indices correspond to the Monte Carlo time within the Markov chain. Let us assume that the mapping of the index to the Monte Carlo time is one to one. Then the parameter $T$ is the maximum time separation over which two observations are correlated. Correspondingly, one can truncate the sum over $c_t$ after $t = T$. This however requires the knowledge about a quantity that is to be estimated.
Anyhow, it was pointed out that the estimation (1.73) performs best when $T$, similar to the window width in [26], is much smaller than the sample size but several times larger than the correlation time $\tau$, the time at which the covariance decays to $e^{-1}$ times the variance of a single observation like if the $\sigma_t$ could be modeled as $\sigma_t^2 = \sigma_0^2 e^{-t/\tau}$. Thus the correct tuning of the parameter $T$ as well as the availability of enough data is vital to a reasonable determination of the error with correlation function based error estimators.

### Blocking based methods

A rather different approach, also used quite commonly in the lattice and condensed matter community, is offered by blocking based methods. A good introduction can be found in the work [27], whereas [28] gives a rather profound review on this topic.
Nevertheless, we will try to illustrate the basic idea behind this approach at this point. Statistically correlated measurements could be interpreted as existing redundancies in the set of measured values. A very efficient and straightforward approach to reduce redundancy is the combination of several, at least two, potentially redundant variables to a single one. How this combination has to be performed depends on the statistics under consideration. In the case of the average one simply performs the combination by averaging over a subset of successive samples.

Assuming, for example, that we have $n$ measurements $(x_i)$ we can form $b$ new variables $x'_j$ by grouping $d$ measurements to one block $B_j = \{x_{d(j-1)+1}, \ldots, x_{dj}\}$, such that all $n = d \times b$ measurements belong to one of the blocks. The new variables are obtained by averaging over all measurements of a block.

$$x'_j = \frac{1}{d} \sum_{i=\in B_j}^{d} x_i \; \forall j = 1 \ldots b \tag{1.75}$$

As shown in [27] one can take the standard error calculated from $x'_j$ as a lower bound for the true error.

$$\sigma(\bar{x}) \geq \sqrt{\frac{1}{b(b-1)} \sum_j (x'_j - \bar{x})^2} \tag{1.76}$$

By repeating this blocking procedure, giving smaller and smaller sets of variables less and less correlated, one eventually removes any redundancy and obtains a better estimation of the true error. The relative error of $\sigma(\bar{x})$ is then $\approx \frac{1}{\sqrt{2(b-1)}}$. The blocking method in its present form can only be applied to primary quantities – quantities that can be estimated directly by averaging the observed samples. But it can be slightly modified to operate also on derived quantities, like meson masses or the static quark-anti-quark potential. Let us consider a derived quantity $y = f(x)$ calculated from the function $f$, $x$ being a primary quantity. Now one constructs sets of blocks $S_j = \bigcup_{k=1\neq j}^{n} B_k$ containing all but the $j'th$ block and takes the average over these sets giving new variables $x''_j$. Then, one can perform an analysis on $f_j = f(x''_j)$ to extract the error of $y$. This is called the jackknife method.

A similar method is the blocked bootstrap method. The bootstrap method without blocking is reviewed in [29]. The extension to the blocked version is straightforward. Instead of systematically leaving out one block one creates new sets by means of re-sampling. Each of the sets is constructed by random picking of blocks of length $b$ until one has a set with the same amount of data points as the original data set $(x_i)$. Then, one evaluates $y = f(x)$ on the mean over each of the sets. The standard deviation of $y$ estimated from this procedure should correspond to the error of $y$. One can resample as many data sets as one requires to stabilise the error estimate.

The blocked bootstrap and the jackknife method are very similar and can be considered as approximations to each other. Thus, it is a matter of choice which method is given the precedence.

Conclusively, one can say that blocking based methods offer a robust error estimation in the sense that one does not need to tune any parameters. The block size just needs to be increased until one gets consistent errors. And if this can not be achieved one is warned about the fact, that the available statistics might be too small to estimate the error correctly, which usually leads to an underestimation of the error. On the other hand, it was argued in [26] that correlation function based methods can lead to more precise results than certain blocking based methods when enough statistics is available.

### 1.4.2. Curve fitting and $\chi^2$-minimisation

Many physical quantities can not be measured directly from a lattice simulation. They often appear as parameters $(\beta_i)_{i=1\ldots k}$ in functions $y = f_\beta(x)$ describing the functional relation of an other quantity $y$ with respect to $x$. The parameters are determined from a fitting procedure of $f$ to a set of $n$ samples $(x_i, y_i)$ with uncertainties $(0, \sigma(y_i))$ by a minimisation of a $\chi^2$-function[17]

$$\chi^2(\beta_1, \ldots, \beta_k) = \frac{1}{2} \sum_{i=1}^{n} \left( \frac{y_i - f_\beta(x_i)}{\sigma(y_i)} \right)^2 , \tag{1.77}$$

which is assumed to be a smooth function of the parameters $\beta$ with smooth first and second order derivatives. This problem can only be considered to be determined if the number of samples $n$ is larger than, or at least equal to, the number of free parameters $k$[18].

### 1.4.3. The p-value

As we will use it quite often in the next two chapters, we want to shortly introduce the p-value at this point. The p-value, $p$ in this subsection, is an alternative way to represent the $\chi^2$-value and the number of degrees of freedom (dof) of a fit. Mathematically it is defined as:

$$p = 1 - F_n(\chi^2) \tag{1.78}$$

for fits based on the minimisation of a $\chi^2$-function (as discussed in the previous subsection), where $\chi^2$ corresponds to the value at the minimum of the $\chi^2$-function determined during the fitting procedure for a fit with $n$ dof. $F_n$ is the cumulative distribution function of the $\chi^2$-distribution with $n$ dof, and can be expressend through $P(s, x)$, the regularised incomplete Gamma function:

$$F_n(x) = P(\frac{n}{2}, \frac{x}{2}) . \tag{1.79}$$

$p \in [0, 1]$ can be seen as the probability that one would obtain an even larger $\chi^2$ value than the given one when the same fit is repeated with a different data set. Hence, a too small p-value indicates that it is very unlikely that one could obtain a worse $\chi^2$ value and hence the only reason for this is simply that the model one used to describe the data must be wrong.
If one uses the correct fit model to describe the data the p-value should be distributed almost uniformly in $[0, 1]$, and one has to select, based on certain criteria, what could be the smallest value (on average) one could obtain from a single draw in the interval $[0, 1]$. A very consequent person will say $p > 0.5$. But the problem with this choice would be

[17] often referred to as least-squares

[18] $f$ might have other parameters which are known a priori. Such parameters do not belong to the set of free parameters.

that even if one uses the correct model, one would reject 50% of all fits, hence, 50% of all correct estimations of the parameters. In the most cases one cannot effort to perform *six* to *seven* independent lattice simulations, which would be necessary to achieve a confidence of $\approx 99\%$ that at least one fit was accepted[19]. Hence, a more common choice is a 95% confidence, which corresponds to the criterion $p > 0.05$. In this way the p-value represents a very objective quantity which can be used to accept or reject a fit on a confidence level basis. This is especially helpful for small numbers of dof $n$ where one could allow much larger ratios of $\chi^2/n$ at 95% confidence, for example $\chi^2/n < 3$ for $n = 2$, as compared to larger $n$ where $\chi^2/n$ should be much closer to one, for example $\chi^2/n < 1.4$ for $n = 40$. To get a better feeling for the p-value, we have plotted the maximally allowed $\chi^2$/dof for three different confidence levels in figure 1.1. This little

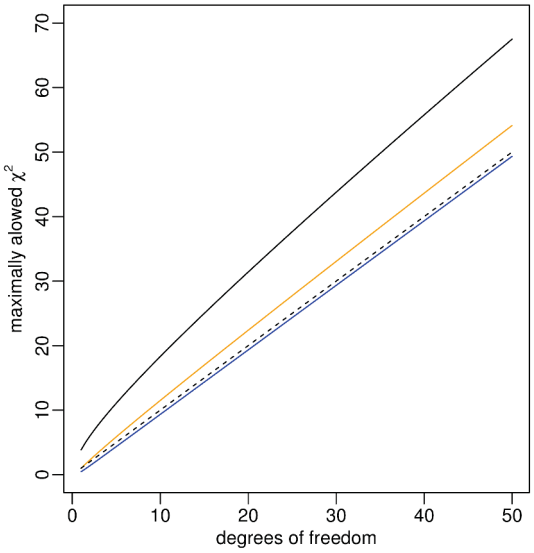


Figure 1.1.: Maximally allowed ratio $\chi^2$/dof for confidence levels (diamond symbols) of 95% (black) , 68% (orange) and 50% (blue). $\chi^2$/dof = 1 is shown as open circles.

introduction to the p-value should suffice for being able to follow the discussion in the next chapters. The interested reader may find more on this topic in respective textbooks on statistical methods for the data analysis.

### Minimisation algorithms

The various algorithms that exist for the detection of minima of a functions can be classified by their efficiency to find the minimum and their sensitivity to adverse ini-

[19] This can be understood like a fair coin flip. If the correct fit model is used, the probability is always 50% (for the criterion $p > 0.5$) that a single fit is accepted. The probability that one of these fits is accepted increases with each further fit that is performed with on an independent data set. After seven runs the probability is 99.2%. If not any of the fits was accepted up to this point one can be very sure that the model to describe the data was wrong.

tial conditions. None of the algorithms is guaranteed to find the global minimum of a function, as one usually has only local information about the behaviour of the function around a considered point. One has to perform several runs with changing initial conditions to check the proper convergence of the algorithm to the same minimum each time. If several minima would be found, the one with the smallest value of the objective function would be treated as the global minimum.
A robust algorithm performing well in practice is the Levenberg-Marquardt algorithm [30]. It requires however the knowledge of the first derivatives of the $\chi^2$-function with respect to the parameters $\beta$. This requires more effort in the implementation phase of the fitting code but pays off twice: At first, one can check explicitly whether a local minimum was found by verifying the vanishing of the gradient $\partial\chi^2/\partial\beta_i$ within a given tolerance. Secondly, gradient based algorithms can chose more efficiently the search direction, and this leads in most cases to a much faster convergence. This is particularly useful if one function evaluation is very time consuming as is the case for $\chi$PT formulae with very involved finite size effects.

### 1.4.4. Implementation as R-Package

A quite reasonable amount of time within this project was spent to create a code that implements the ideas and algorithms of this section which did not exist already in R, a programming language and program for statistical computing (`r-project.org`). This code is publicly available under `https://github.com/annube/Chifit`.
The concepts, methods and ideas presented in this chapter form the basis for the understanding of the next chapters, where some of the methods will be used extensively. The first practical topic we want to investigate is the chiral extrapolation of the pion mass and decay constant.

# 2. Setting the lattice scale

A necessary prerequisite for the expression of any quantity in physical units is the determination of the lattice scale $a$. In general, many possibilities exist to fix the lattice spacing. Apart from the approach used here also other hadronic observables, like the kaon decay constant [31] or the mass of the omega baryon [32], have been used for reasonable determinations of $a$. Another kind of suitable observables are $r_0$, the Sommer scale[19], $w_0$, and $t_0$, quantities arising from the Wilson flow[33]. The speciality of these pure gluonic quantities is that they can be measured to high precision on the lattice, but that their physical value can hardly be determined from experiments, if at all. We will come back to the discussion of $r_0$ below, in section 2.2. However, we will use this quantity only for the determination of *ratios* of lattice spacings.
The choice we want to stick to in this work is the scale setting through the pion decay constant $f_\pi$ and the pion mass $M_\pi$. These quantities can be determined straightforwardly with high precision on the lattice. But the following considerations have to be taken into account in such a scale setting procedure.
Our lattice simulations have been carried out with light quark masses ranging from 2.5 to 11 times the physical light quark mass[1]. During the scale setting one has to perform an extrapolation to the physical point, defined by the condition that the ratio $f_\pi/M_\pi$ should take on its physical value. For such an extrapolation we have to rely[2] on a $\chi$PT description involving the leading and next-to-leading order (NLO-$\chi$PT). But it is questionable over which range of pion masses, or equivalently the range of light quark masses, the NLO expressions of $\chi$PT describe correctly the behaviour of the corresponding quantities, especially $f_\pi$, from our lattice simulations. In the work from Borsányi et. al., 2012 [3] it was shown that their lattice data is described by $\chi$PT at NLO only up to about 4 to 5 times the physical light quark mass. In an even more recent analysis [21] it was explicitly concluded that NLO-$\chi$PT should only be applied up to pion masses of 300 MeV. This observation suggests a similar investigation on our lattice data.
Twisted mass lattice QCD is $O(a)$-improved at maximal twist. Hence, discretisation effects are expected to appear at $O(a^2)$. In a chiral extrapolation of $f_\pi$ and $M_\pi$ one can distinguish between discretisation effects directly proportional to $a^2$ and $O(a^2)$ corrections to the LO neutral pion mass $M_{\pi^0}$, a quantity appearing in the $\chi$PT formulae. This becomes important as $M_{\pi^0}$ contributes through exactly the same mechanism as $M_{\pi^\pm}$ to the finite volume correction (cf. formula (1.66), subsection 1.3.2), which depend exponentially(!) on the pion mass. This will become more clear in the course of the

[1] We want to remind the reader that we refer to the average up/down quark mass.
[2] This is due to the dramatic increase of the number of free parameters of the theory with higher orders of $\chi$PT and the lack of sufficient amounts of data to fix them.

following lines.
As just mentioned, an important issue is the finite volume effects, which are exponentially dependent on the dimensionless quantity $M_\pi L$, the pion Compton wavelength, $\lambda_C = M_\pi^{-1}$, in units of the spatial extent $L$. For a value of $M_\pi L = 4$ and a pion mass of 320 MeV (the heaviest pion mass we use for our final results) the relative finite volume correction (1.60) to $f_\pi$ in continuum $\chi$PT (NLO) is at the level of $\approx 4‰$. This is at the same order as the statistical errors of our measurement of $f_\pi$, which range from $\approx 2.5 - 6.3‰$. If one considers a smaller volume with $M_\pi L = 3$ ($M_\pi$ kept fixed), the relative shift of $f_\pi$ due to finite volume corrections goes up to $\approx 2\%$ and is significantly larger (approximately 5 times) than the statistical errors. Conclusively, one can say that the physical spatial extent $L$ should be at least four times larger than the pion Compton wavelength (This corresponds to the condition $M_\pi L > 4$.) to keep the finite size effects at the level of the statistical errors. This criterion is fulfilled for most of our ensembles when considering the charged pion (see table 2.2). As shown in [1] the chiral logarithms appearing for example in the NLO $\chi$PT expression for the charged pion, eq. (1.3.2), subsection 1.64, contain also the neutral pion mass. Hence, the corresponding finite volume correction is governed by the quantity $M_{\pi^0} L$. This becomes important if ones realises that the neutral pion mass is much lighter than the charged one on many of our ensembles. In this way an entanglement is created between finite size and discretisation effects making it unavoidable to describe both simultaneously in a chiral fit.
A scale setting purely based on a chiral extrapolation would lead to results with unsatisfying large errors coming from the necessity to perform a too far extrapolation to the physical point. Precise information at least about the ratios of lattice spacings is vital to a precise determination of the lattice spacings itself. Such information can be provided by the Sommer scale $r_0$, which was measured on each ensemble and has to be extrapolated to the chiral limit (light quark mass = 0) for a mass independent definition of $r_0$.
As a result of the previous discussion we can establish the following plan for this chapter. First, we will give an overview of the simulated parameters and some important observables in section 2.1. We will proceed with the determination of $r_0$ in the chiral limit for each value of $\beta$ in section section 2.2. In section 2.3 it will be shown how $f_\pi^\pm$ and $M_{\pi^\pm}$ have been obtained from the pseudoscalar correlator. Finally, we will discuss in section 2.4 our scale setting procedure based on chiral fits.

## 2.1. Simulation parameters

The European Twisted Mass Collaboration (ETMC) has put significant effort into the generation of gauge configurations suitable for the determination of a wide range of interesting observables in QCD. Noteworthy is the number of four dynamical quarks, namely up/down, strange and charm, in the simulation, which makes this set of ensembles a good starting point for a realistic investigation of mesons and other hadrons containing strange and charm quarks. The three simulated values of $\beta$ and the corresponding approximate lattice spacings are listed in Table 2.1.

| $\beta$ | approximate lattice spacing $a$ |
|---|---|
| 1.90 | 0.090 fm |
| 1.95 | 0.081 fm |
| 2.10 | 0.062 fm |

Table 2.1.: The three $\beta$-values used in our lattice simulations and the approximate lattice spacing

The set of simulated parameters and their approximate charged pion mass is given in Table 2.2.

Our ensembles feature pion masses ranging from 485 MeV down to 220 MeV. Most of the volumes, except A40.24, B25.32, D15.48 and D20.48, fulfill the criterion $M_{\pi^\pm} L > 4$. D20.48 fails the criterion only slightly, and the lattice size for A40.24 was chosen intentionally so small for the verification of the correct description with respect to finite size effects.

Although the PCAC mass of ensembles A30.32 and B25.32 would fail our criterion to be smaller than a tenth of $\mu_l$ we included these ensembles in our chiral fits in lack of data close to physical pion masses. But we performed fits where A30.32 and B25.32 were excluded. We verified the correct prediction of the values for $M_\pi$ and $f_\pi$ at these ensembles and found completely compatible results for the lattice spacings and low energy constants, such that we will discuss the case where these ensembles are included in the fits anyway.

We will proceed now with the determination of $r_0$ in the chiral limit.

## 2.2. Relative scale setting with $r_0$

As indicated earlier in this chapter, the precise determination of lattice spacing ratios based on the Sommer scale $r_0$ is an important ingredient for an accurate scale setting based on chiral extrapolations of $f_\pi$ and $M_\pi$. The measured values of $r_0$ are listed in Table 2.3. Obviously, $r_0$ exhibits a clear light quark mass dependence. An extrapolation to zero light quark mass is necessary for a mass independent scale setting. Such an extrapolation is less complicated as for example the chiral extrapolation of $f_\pi$, because the chiral dependence of $r_0$ is much milder. A quadratic extrapolation polynomial in the variable $x = (r_0 M_\pi)^2$, described by the coefficients $h_{1,2}$, is commonly assumed to be sufficient.

$$r_0(\mu_l, \beta) = r_0^\chi(\beta)(1 + h_1 x + h_2 x^2) \tag{2.1}$$

The superscript $\chi$ on $r_0$ refers to $r_0$ extrapolated to zero light quark mass. Conventionally, $r_0^\chi$ is also used in the definition of the variable $x$.

$$x^\chi = (\ r_0^\chi(\beta)\ M_\pi(\beta, \mu_l)\ )^2 \tag{2.2}$$

| Ensemble | $\beta$ | $L/a$ | $\kappa_{cr}$ | $a\mu_l$ | $\frac{m_{\mathrm{PCAC}}}{\mu_l}$ | $\frac{M_{\pi^\pm}}{\mathrm{MeV}}$ | $M_{\pi^\pm}L$ |
|---|---|---|---|---|---|---|---|
| A30.32 | 1.90 | 32 | 0.1632720 | 0.0030 | -0.123(87) | 270 | 4.0 |
| A40.24 | 1.90 | 24 | 0.1632700 | 0.0040 | -0.148(83) | 320 | 3.48 |
| A40.32 | 1.90 | 32 | 0.1632700 | 0.0040 | -0.055(55) | 310 | 4.5 |
| A60.24 | 1.90 | 24 | 0.1632650 | 0.0060 | -0.037(50) | 380 | 4.1 |
| A80.24 | 1.90 | 24 | 0.1632600 | 0.0080 | 0.020(19) | 435 | 4.8 |
| A100.24 | 1.90 | 24 | 0.1632550 | 0.0100 | 0.025(18) | 485 | 5.3 |
| B25.32 | 1.95 | 32 | 0.1612420 | 0.0025 | -0.185(69) | 260 | 3.4 |
| B35.32 | 1.95 | 32 | 0.1612400 | 0.0035 | 0.009(34) | 305 | 4.0 |
| B55.32 | 1.95 | 32 | 0.1612360 | 0.0055 | -0.069(13) | 375 | 5.0 |
| B75.32 | 1.95 | 32 | 0.1612320 | 0.0075 | -0.047(12) | 440 | 5.8 |
| B85.24 | 1.95 | 24 | 0.1612312 | 0.0085 | -0.001(16) | 470 | 4.7 |
| D15.48 | 2.10 | 48 | 0.1563610 | 0.0015 | -0.128(35) | 220 | 3.3 |
| D20.48 | 2.10 | 48 | 0.1563570 | 0.0020 | 0.016(23) | 255 | 3.9 |
| D30.48 | 2.10 | 48 | 0.1563550 | 0.0030 | -0.006(17) | 310 | 4.7 |

Table 2.2.: This table shows the set of simulated ensembles used for the scale determination in the pion sector. Columns two to five contain the simulation parameters, whereas columns six and seven contain the approximate pion mass (rounded to units of 5 MeV) and lattice size in units of the Compton wavelength of the pion.

This comes at the small price of $r_0^\chi$ appearing in up to the fifth power in (2.1), turning the following fits into a non-linear regression problem. As its determination is simple and precise we will always utilise the charged pion mass in (2.2).

It should be noted that the quantities $r_0$ and $M_\pi$ in (2.1) and (2.2) are always in units of the lattice spacing corresponding to the value of $\beta$ at which they were determined. Hence, the extracted values of $r_0^\chi$ will also be obtained in lattice units. Under the assumption that $r_0^\chi$ in physical units, what ever value it actually has, takes on the same value on all lattices, one can extract the lattice spacing ratios in the following way:

$$R_i = \frac{a(\beta_i)}{a(\beta_0)} = \frac{r_0^\chi(\beta_0)}{r_0^\chi(\beta_i)} \quad (\beta_0, \beta_1, \beta_3) = (1.90, 1.95, 2.10)\ . \tag{2.3}$$

One of the remaining questions is whether one has to apply the full fit formula (2.1), or whether the linear or the quadratic term in $x$ could be neglected. Furthermore, if one assumes that the dimensionless coefficients $h_1$ and $h_2$ are of universal nature for a given lattice setup one could perform a global fit of all lattice spacings simultaneously. We have investigated the various possibilities and summarised the results in tables 2.4

| Ensemble | $r_0$ |
|---|---|
| A40.32 | 5.179(49) |
| A50.32 | 5.081(45) |
| A60.24 | 5.209(58) |
| A80.24 | 4.989(40) |
| A100.24 | 4.864(21) |
| B25.32 | 5.728(35) |
| B35.32 | 5.634(43) |
| B55.32 | 5.662(33) |
| B75.32 | 5.566(44) |
| B85.24 | 5.493(41) |
| D15.48 | 7.614(55) |
| D20.48 | 7.449(42) |
| D30.48 | 7.409(26) |
| D45.32sc | 7.310(49) |

Table 2.3.: The table shows the measured values of the Sommer scale $r_0$ for each ensemble in lattice units.

(global fits) and 2.5 (separate fits for each lattice spacing). The corresponding plots are shown in figures 2.1 (linear fits), 2.2 (quadratic fits without the linear term) and 2.3 (quadratic fits with linear term).
Here and in the following we will often make use of the so called p-value. This quantity combines the value of $\chi^2$ and the number of degrees of freedom (dof) to a single one, and allows decisions on a confidence level basis. A short introduction to the p-value and a description of the use to obtain statistically more objective statements was given in chapter 1, subsection 1.4.3.
First we want to discuss the global fits in Table 2.4. Each data column corresponds to a different fit function (see table description). An interpretation based on the p-value leads to the conclusion that a pure quadratic fit (second column) is preferred over the other possibilities. The $\chi^2$-value and the degrees of freedom are given additionally for getting an impression on how they are related to the p-value. In fact, only the pure quadratic fit would survive a 95% confidence level criterion. Nevertheless, the ratios $R_1$ and $R_2$ come out very consistently among all three fits.
Looking at the results of the individual fits for each lattice spacing, given in Table 2.5, we find again a slight preference of a pure quadratic fit for $\beta = 1.90$ and $\beta = 1.95$, if we rely on the p-value. Although the pure quadratic fit at $\beta = 2.10$ has the smallest p-value, the obtained value $R_2 = 0.694(6)$ is in perfect agreement with the corresponding global fit (second column in table 2.4). We cannot give preference to one of the three forms

| | linear | quadratic | both |
|---|---|---|---|
| p-value | 0.024233 | 0.057605 | 0.038513 |
| $\chi^2$/dof | 20.6/10 | 17.8/10 | 17.7/9 |
| $r_0^\chi(\beta = 1.90)$ | 5.301(41) | 5.203(32) | 5.222(60) |
| $R_1$ | 0.900(5) | 0.902(5) | 0.902(5) |
| $R_2$ | 0.693(4) | 0.693(4) | 0.694(4) |
| $h_1$ | -0.0549(47) | - | -0.0101(288) |
| $h_2$ | - | -0.0345(28) | -0.0282(184) |

Table 2.4.: Shown are the results for global fits of $r_0$ to formula (2.1) on all lattice spacings simultaneously. The first data column ("linear") shows results for a linear fit in $x$ ($h_2$ set to zero). The following column ("quadratic") shows a pure quadratic fit ($h_1$ set to zero); and the last column ("both") investigates the case where $h_1$ and $h_2$ are free fit parameters. Instead of $r_0^\chi(\beta = 1.95)$ and $r_0^\chi(\beta = 2.10)$ we give the ratios $R_{1,2} = \frac{r_0^\chi(\beta=1.90)}{r_0^\chi(\beta=1.95,2.10)}$

of the polynomial from the p-value solely. But the pure quadratic fit is the one leading to the smallest statistical errors and should therefore be preferred, but we will take the other fit results into account as a systematic error (see below).
As final result for the lattice spacing ratios we choose to use in a conservative way (with respect to previous extrapolations of $r_0^\chi$ by the ETMC [34]) the results of the pure quadratic fits performed for each lattice spacing separately. We take the modulus of the difference to the global fit as systematic error. Hence, the final result is:

$$R_1 = 0.913(8)_{stat.}(11)_{sys.} = 0.913(14)_{comb.} \tag{2.4}$$
$$R_2 = 0.694(6)_{stat.}(1)_{sys.} = 0.694(6)_{comb.}\ , \tag{2.5}$$

where the errors have been added in quadrature.

Our values are in perfect agreement with other results from ETMC [35]. $R_1$ and $R_2$ can now be used as priors in the chiral fits to precisely fix the ratios between the three lattice spacings.

Of course, one of the most important prerequisites for the chiral fits is the determination of $f_\pi$ and $M_\pi$ from the pseudoscalar correlator. This will be discussed in the next section.

## 2.3. Analysis of the charged pseudoscalar correlator

In chapter 1 we discussed that the pseudoscalar correlator should behave in the limit of large times like a hyperbolic cosine function. Hence, we are going to describe $C_{\mathcal{PP}}$ with

| $\beta$ | *type* | $r_0^\chi$ | $h_1$ | $h_2$ | p-value | $\chi^2$/dof |
|---|---|---|---|---|---|---|
| 1.9 | linear | 5.405(60) | -0.068(7) | - | 0.095 | 6.4/3 |
| | quadr. | 5.231(37) | - | -0.0379(37) | 0.149 | 5.3/3 |
| | both | 5.141(231) | 0.04(10) | -0.06(6) | 0.074 | 5.2/2 |
| | | $R_1$ | | | | |
| 1.95 | linear | 0.930(13) | -0.039(8) | - | 0.337 | 3.4/3 |
| | quadr. | 0.913(8) | - | -0.026(5) | 0.452 | 2.6/3 |
| | both | 0.901(46) | 0.01(6) | -0.036(43) | 0.275 | 2.6/2 |
| | | $R_2$ | | | | |
| 2.1 | linear | 0.706(10) | -0.056(14) | - | 0.174 | 3.5/2 |
| | quadr. | 0.694(6) | - | -0.049(14) | 0.070 | 5.3/2 |
| | both | 0.656(30) | -0.14(6) | 0.07(5) | 0.126 | 2.3/1 |

Table 2.5.: The table shows fits of $r_0$ performed separately for each lattice spacing. The second column indicates the applied fit ansatz (see description table 2.4). As in Table 2.4 we have given the ratios $R_1$ and $R_2$ for $\beta = 1.95$ and $\beta = 2.10$ formed from $r_0^\chi$ values obtained from the same type of fit. Braces indicate statistical errors calculated from 100 bootstrap samples.

the following model

$$C_{\mathcal{PP}}(x_0) \sim C\frac{1}{2}\left(e^{-m_{\text{eff}}x_0} + e^{-m_{\text{eff}}(T-x_0)}\right) . \tag{2.6}$$

The coefficient $C$ and the effective mass $m_{\text{eff}}$ will be determined from a fit of this model to the correlator data. As in the previous section, we consider all quantities in lattice units. $m_{\text{eff}}$ is then identified with the pion mass $M_\pi$ and the pion decay constant $f_\pi$ can be determined from

$$C = \frac{(M_\pi^2 f_\pi)^2}{2M_\pi \mu_l} . \tag{2.7}$$

This expression can be obtained from comparing (2.6) with formulae (1.51) in subsection 1.2.5.

For an actual analysis one would like to include as many data as possible, consequently as many time slices as available, into the analysis to keep the statistical errors as small as achievable. One is restricted however by the criterion of large times when applying (2.6). This is caused by the influence of higher excited states, especially the first excited state. Consequently, one is able to define an interval $[x_0^{\min}, T - x_0^{\min}]$ by the requirement, that the contribution of the first excited state to the correlator becomes negligible.

This criterion can be realised by a further fit to an extended model describing both, the

ground state and the first excited state. A suitable model is constructed as the sum of two parametrised hyperbolic cosine functions, each having different parameters.

$$C_{\mathcal{PP}}(t) \sim C\frac{1}{2}\left(e^{-m_{\text{eff}}t} + e^{-m_{\text{eff}}(T-t)}\right) + C_2\frac{1}{2}\left(e^{-m_{\text{exc}}t} + e^{-m_{\text{exc}}(T-t)}\right) \tag{2.8}$$

Therein, $C_2$ and $m_{\text{exc}}$ represent the parameters of the excited state. A consistent fit (based on the $\chi^2$-value) to the correlator is performed with this extended model in a time interval being as large as possible. As mentioned before, $x_0^{\min}$ is defined as the point where the contribution to the correlator coming solely from the excited state (second term of the sum in (2.8) falls below the fraction $R$ of $\Delta C_{\mathcal{PP}}(x_0)$ , the statistical error of $C_{\mathcal{PP}}(x_0)$ at a time slice $x_0$.

$$\frac{C_2\frac{1}{2}\left(e^{-m_{\text{exc}}x_0} + e^{-m_{\text{exc}}(T-x_0)}\right)}{\Delta C_{\mathcal{PP}}(x_0)} < R \quad \forall\, x_0 > x_0^{\min}\,, \tag{2.9}$$

A similar method has been investigated in [31]. In our fits $R$ has been set to 0.2. An illustration of this procedure is shown in Figure 2.4.

After the determination of $x_0^{\min}$ we performed a single-state fit (formula (2.6)) in the corresponding region to extract $M_{\pi^\pm}$ and $f_{\pi^\pm}$. For the error analysis, this procedure has been repeated with 1000 blocked bootstrap samples[3]. The block sizes have been determined individually for each ensemble by, starting from 1, increasing the block size until no further significant increase of the error (within errors) could be observed. An example is shown in figure 2.5.

It is interesting to note, that for ensemble B25.32 one would estimate a value[4] of $\tau_{\text{int}} \approx 3.5$ for $f_\pi$ , although this result is only obtained when one goes to block sizes of about 150. This can only be taken as an indication that the usual model of an exponentially decaying covariance of the underlying observable (the pseudoscalar correlator at certain time slices) in Monte Carlo time is not valid in this case. Hence, the interpretation of $\tau_{\text{int}}$ as a correlation length in Monte Carlo time is a bit misleading, as small but significant correlations must exist over Monte Carlo times of 50 times longer than $\tau_{\text{int}}$.

The bootstrap samples are being reused for the statistical error analysis for the chiral fits. The final results for $f_\pi$ and $M_\pi$ are found in Table B.1 in appendix B. They are in good agreement with results from [24] (p. 10, table 1).

We come now to the final part of this chapter, namely the global description of the data for $f_\pi$ and $M_\pi$ in the framework of chiral perturbation theory and, based on this, the chiral extrapolation to the physical point of these quantities, allowing us to set the scale of our lattices.

[3] The blocked bootstrap method was introduced in chapter 1, subsection 1.4.1.

[4] We refer to the definition of $\tau_{\text{int}}$ as defined in [26]

## 2.4. Scale setting from chiral fits to $f_\pi$ and $M_\pi$

Throughout this section we should keep in mind that the focus should lie on the scale setting of our lattice setup. As we rely on chiral extrapolations through $\chi$PT formulae, we can not avoid to touch a very long stated problem, namely the question up to which pion mass chiral perturbation theory at NLO can describe correctly the lattice data for $f_{\pi^\pm}$ and $M_{\pi^\pm}$. This is in fact a very important question, if one is simulating rather far from the physical point (for example at four to five times the light quark mass). The precise determination of the physical point (where $f_\pi/M_\pi$ takes on its experimental value) requires an extrapolation in the light quark mass and hence, relies on the precise determination of the exact form of the predicting formulae, determined by the low energy constants.
Those in turn, can only be determined correctly from lattice data in the region of light quark masses where chiral perturbation theory at NLO correctly describes QCD.
More explicitly, there might be a critical largest light quark mass above which $\chi$PT fails to describe our lattice data.
When the pion masses then become too large one might still be able to perform fits based on the $\chi$PT formulae describing the data within errors. But the extracted low energy constants are very likely to be wrong in the sense that they are not suitable to describe QCD at and around zero light quark mass, and even more importantly could lead to a misidentification of the true physical point.
If we doubt the validity of the $\chi$PT prediction over the full range of pion masses in our ensembles we have to introduce an upper bound for the pion masses included in the fit. Thus, we first investigate the influence of such a mass cut on the $\chi^2$-value with respect to the degrees of freedom (or equivalently the p-value), which we take as an indicator for the consistency of the fit.
As a next step we want to take a closer look to the $\chi^2$-function we used in the chiral fits, as it is a bit more elaborate than in the case of the correlator fits in section 2.3.

### 2.4.1. Construction of the $\chi^2$ function

The $\chi^2$ function for the chiral fits is constructed as follows:

$$\chi^2 = \chi^2_f + \chi^2_m + \chi^2_{m_0} + \chi^2_{\text{prior}} \,. \tag{2.10}$$

$\chi^2_f$, $\chi^2_m$ and $\chi^2_{m_0}$ correspond to the charged pion mass and decay constant and the neutral pion mass. Their design is described in subsection 1.4.2, with $af_{\pi^\pm}$, $(aM_{\pi^\pm})^2$ and $(aM_{\pi^0})^2$ (quantities in lattice units) in place of $y_i$ and formulae (1.63), (1.64) and (1.65):

$$f_{\pi^\pm} = f_0 \left(1 - \frac{1}{(4\pi f_0)^2}\left(M^2_\pm \ln\frac{M^2_\pm}{\Lambda^2_4} + M^2_0 \ln\frac{M^2_0}{\Lambda^2_4}\right) + C_f a^2\right) \tag{1.63}$$

$$M^2_{\pi^\pm} = M^2_\pm \left(1 + \frac{M^2_0}{(4\pi f_0)^2}\ln\frac{M^2_0}{\Lambda^2_3} + C_{M_\pm} a^2\right) \,. \tag{1.64}$$

$$M_{\pi^0}^2 = M_\pm^2 \left(1 + \frac{1}{(4\pi f_0)^2}\left(2M_\pm^2 \ln\frac{M_\pm^2}{\Lambda_3^2} - M_0^2 \ln\frac{M_0^2}{\Lambda_3}\right)\right) + 2c_2 a^2 \left(1 - 4\frac{M_0^2}{(4\pi f_0)^2}\ln\frac{M_0^2}{\Xi^2} + C_{M_0} a^2\right) , \tag{1.65}$$

repeated here for the sake of a better readability, as the functions, which include the finite size effects of section 1.3.2. The parameters of these functions, $B$, $f_0$, $c_2$ , $\Lambda_{3,4}$, $\Xi$ and $C_{M_\pm,M_0,f}$, are made dimensionless by multiplications with suitable powers of the largest lattice spacing (usually the one at $\beta = 1.90$). In this way we obtain dimensionless parameters and avoid the necessity for an explicit scale setting during the fitting procedure. The parameters at the smaller lattice spacings are simply obtained by multiplications with suitable ( the same as for the lattice spacing) powers of $R_1 = \frac{a(\beta=1.95)}{a(\beta=1.90)}$ or $R_2 = \frac{a(\beta=2.10)}{a(\beta=1.90)}$, the quantities that have been computed in section 2.2. These ratios are not kept fixed in the fits, but are treated as semi-free parameters in the sense that, they are in principle free but constrained through the $\chi^2_{\text{prior}}$ term. This term is for the consideration of prior knowledge about certain parameters. It is constructed as follows:

$$\chi^2_{prior} = \frac{1}{2}\sum_i \frac{(\beta_i - \beta_i^{prior})^2}{\sigma_i^2} , \tag{2.11}$$

where $\beta_i$ is the actual value of a fit parameter, $\beta_i^{prior}$ its value known from a previous determination with the uncertainty $\sigma_i$. The renormalised light quark mass $\mu^R = \mu_l/Z_P$ is computed using values of $Z_P$ in the $\overline{MS}$-scheme, which are also semi-free parameters like $R_{1,2}$. Their priors and uncertainties are quoted in table Table 2.6 (Silvano Simula, June 2013, personal communication). Although, we determine the parameter $B$ in our

| $\beta$ | $Z_P$ |
|---|---|
| 1.90 | 0.521(7) |
| 1.95 | 0.506(4) |
| 2.10 | 0.513(3) |

Table 2.6.: Values used for the pseudoscalar current renormalisation constant $Z_P$ for the three lattice spacings, required for the renormalised light quark mass $\mu^R = \frac{\mu_l}{Z_P}$

fits, its detailed value is irrelevant for the scale setting. Hence, also the detailed value of $Z_P$ is irrelevant as it can be absorbed into the definition of $B$ (for each lattice spacing separately). Our experiments showed that no significantly different results for the lattice scales are obtained when $Z_P$ is set to one on all lattices. Hence, we assume only rather small systematic uncertainties for the final result arising from renormalisation constant priors. To avoid confusion across the different definitions and methods for the determination of $Z_P$ we will always quote the value of $M_\pm^{\text{phys}}$, the leading order charged

pion mass at the physical point, instead of $B$ and $\mu^{R,\text{phys}}$ separately in the scale setting procedure.
We have now established all relevant prerequisites for the chiral fits, and can finally turn to the results we obtain from our lattice data.

### 2.4.2. Results

Ideally one would perform one global fit with data from all ensembles from table 2.2. But as indicated before, we have to investigate the influence of a pion mass cut. Hence, we have selected the cuts listed in table 2.8, which are based on the available data. The mass cut refers to the charged pion masses as given in table 2.2, section 2.1. As we will see later in the figure 2.7, these raw pion masses receive significant downward shifts from discretisation and finite volume corrections.
The fit results are listed in table 2.9. Additionally to the cut-off parameters $\Lambda_{3,4}$ we have also give the values of the often used low energy constants $l_3$ and $l_4$, which are related to $\Lambda_i$ through $l_i = 2\ln\frac{\Lambda_i}{M_\pi^{phys}}$. $M_\pi^{phys} = 134.8$ MeV is the physical[5] value of the pion mass.

| $M_{\pi^\pm}^{\max}$/MeV | ensembles included in the fit | fit label |
|---|---|---|
| 320 | A30.32, A40.32, B25.32, B35.32, D15.48, D20.48, D30.48 | I |
| 375 | ensembles of fit "I" and A60.24, B55.32 | II |
| 435 | ensembles of fit "II" and A80.24 , B75.32 | III |
| 485 | ensembles of fit "III" and A100.24 , B85.24 | IV |

Table 2.8.: This table shows an overview of the pion mass cuts we applied to our data in the chiral fits. In the second column we list the ensembles we used for a certain fit. The third column shows the corresponding fit labels, referred to in the discussion.

It can be seen clearly that only the most restrictive cut of $M_{\pi^\pm}^{\max} = 320$ MeV leads to a consistent fit result. All other fits have too large $\chi^2$ values with respect to the degree of freedom as it can be deduced from the p-value. For the most quantities we can observe a clear dependence on the mass cut. The lattice spacings and $f_0$ decrease, $M_\pm^{\text{phys}}$, $l_3$ and $l_4$ increase with the increasing pion mass cut.

[5] We use here the pion mass corrected for the effects of disregarding the electromagnetic interaction and the non-degeneracy of the up and down quark mass in nature [7].

| fit label | I | II | III | IV |
|---|---|---|---|---|
| figure no. | 2.6, 2.7 | 2.8 | 2.9 | 2.10 |
| p-value | 0.8161 | 0.0073 | 0.0050 | 0.0032 |
| $\chi^2$/dof | 3.68/7 | 25.67/11 | 32.79/15 | 40.06/19 |
| $a(\beta = 1.90)$ / fm | 0.0899(10) | 0.0893(8) | 0.0889(8) | 0.0886(8) |
| $a(\beta = 1.95)$ / fm | 0.0812(9) | 0.0806(8) | 0.0803(7) | 0.0798(7) |
| $a(\beta = 2.10)$ / fm | 0.0624(6) | 0.06189(49) | 0.06167(44) | 0.06147(48) |
| $M_{\pm}^{\text{phys}}$ / MeV | 135.85(29) | 136.45(17) | 136.53(10) | 136.66(11) |
| $f_0$ / MeV | 122.85(41) | 122.34(25) | 121.96(17) | 121.69(18) |
| $\Lambda_3$ / GeV | 0.30(9) | 0.52(8) | .55(5) | 0.62(6) |
| $\Lambda_4$ / GeV | 1.07(11) | 1.19(7) | 1.31(5) | 1.39(6) |
| $l_3$ | 1.6(5) | 2.7(3) | 2.83(17) | 3.05(17) |
| $l_4$ | 4.14(18) | 4.36(11) | 4.54(7) | 4.66(7) |
| $\sqrt[4]{-c_2}$ / MeV | 580(12) | 586(25) | 574(28) | 554(44) |

Table 2.9.: Results of the chiral fits are shown for four different pion mass cuts. See table 2.8 for the list of ensembles used.

We have repeated fit I, the fit with the lowest mass cut of $M_{\pi^{\pm}}^{\max} = 320$ MeV, but included ensemble A40.24 and found a very good description of the data and completely compatible results for the lattice spacings. From [24] we have taken the data for the neutral pion mass and verified a perfect description of the data in case of fit I. Although we have to note that the neutral pion mass has a rather large error ( around 1-2% ) as compared to the charged pion mass ( around 3 per mille) leading to increased errors (roughly a factor of 10 for the lattice spacings) in the fit results. But they agree perfectly with results of fit I.

In reference [2] a similar scale setting as in this work was performed, but under the usage of the continuum $\chi$PT formulae (1.57) (not describing the explicit isospin breaking) and the full range of pion masses up to $\approx 480$ MeV. The following lattice spacings and low energy constants were determined in this source (Ref. [2], table 2, last row):

$$a(\beta = 1.90) = 0.0863(4) \text{ fm} \tag{2.12}$$
$$a(\beta = 1.95) = 0.0779(4) \text{ fm} \tag{2.13}$$
$$a(\beta = 2.10) = 0.0607(2) \text{ fm} \tag{2.14}$$
$$f_0 = 121.05(5) \text{ MeV} \tag{2.15}$$
$$l_3 = 3.53(5) \text{ and} \tag{2.16}$$
$$l_4 = 4.73(2) \text{ ,} \tag{2.17}$$

using data from all three lattice spacings. Using our knowledge about the tendencies of the quantities $a$, $f_0$, $\Lambda_3$ and $\Lambda_4$ with respect to the pion mass cut, we find in [2], as expected, significantly smaller values for $a$ and $f_0$ and larger values for $l_3$ and $l_4$ when comparing to the results of fit I. Hence, it is an obvious conclusion that the deviations of our results from the results in [2] could be explained by the application of a pion mass cut.
The extracted low energy constants $f_0$ and $l_4$ from fit I agree very well with the results, $f_0 = 122.72(07)_{stat}(35)_{syst}$ and $l_4 = 4.03(03)_{stat}(16)_{syst}$, obtained in [3], where data around the physical point up to pion masses of 240 MeV have been used to determine these quantities. The smallness of our result for $l_3 = 1.6(5)$ (cf. $l_3 = 3.16(10)_{stat}(29)_{syst}$ [3]) might originate in the rather small number of data points for the lowest pion mass cut. But looking at the p-value of fit I we see that there is still some room for the inclusion of a prior for $\Lambda_3$ from [3]:

$$\Lambda_3^{\text{prior}} = 653(106)\ \text{MeV}\ . \tag{2.18}$$

If we take into account this prior, as we did with the ratios $R_i$ and the renormalisation constants $Z_P$, we still obtain a fit with a p-value of 0.234 ($\chi^2/\text{dof} = 10.5/8$) and mean values of $\Lambda_3 = 450(70)$ MeV ($l_3 = 2.41(30)$), $M_\pm^{\text{phys}} = 136.29(18)$ MeV and all other parameters basically unchanged. The extracted lattice spacings coincide within a tenth of their statistical error as compared with the ones obtained from the unconstrained (with respect to $\Lambda_3$) fit I. We can deduce that our lattice data is completely compatible with the low energy constants obtained in [3]. In the more recent analysis [21] the value for $l_3$ was lowered to $l_3 = 2.5 \pm 0.5 \pm 0.4$, which is in even better agreement with our result. And most importantly, the usage of the prior for $\Lambda_3$ (2.18) does not change the scale setting.

The Wilson $\chi$PT parameter $c_2$ can be compared equally well to existing results. In [24] this parameter was estimated[6] to $c_2 = -(528(33)\ \text{MeV})^4$ and $c_2 = -(643(29)\ \text{MeV})^4$ from two different methods. Our result lies exactly in between and we are thus confident that it is sensible. This confidence is further supported by the fact that we obtained our result solely from the charged pion mass and decay constant, whereas in [24] the result was obtained from the neutral and charged pion mass. We note in passing that a fit with $c_2 = 0$ (corresponding to a fit to (1.57)) leads to a p-value of 0.0014 ($\chi^2/\text{dof} = 25.2/8$) (with ensembles from fit I), and hence fails *by far* the 95% confidence criterion. This fact strongly suggests that our data should not be described by the continuum $\chi$PT formulae but requires the consideration of isospin breaking effects.
For the estimation of systematic errors we have repeated fit I-IV with results of the charged pion masses and decay constants from [24]. We find completely consistent results between fits corresponding to the same pion mass cut and take the deviations in the lattice spacings as a systematic uncertainty.
As a result of the previous discussion we can establish fit I as the most sensible one.

[6] For taking into account the different definitions of $c_2$ in [24] (see formula (9) specified therein) and this work ( see formula (1.62)) , the results have been multiplied with $\sqrt[4]{2}$.

Hence, we quote the following results for the lattice spacings as our final ones

$$a(\beta = 1.90) = 0.0899\ (10)_{stat.}\ (8)_{sys.}\text{fm} \tag{2.19a}$$
$$a(\beta = 1.95) = 0.0812\ (9)_{stat.}\ (6)_{sys.}\text{fm} \tag{2.19b}$$
$$a(\beta = 2.10) = 0.0624\ (6)_{stat.}\ (4)_{sys.}\text{fm}\ . \tag{2.19c}$$

An alternative determination of the scale by the ETMC based on the nucleon mass [36] with a similar restriction in the range of pion masses gives compatible results . Even though, a trend to slightly larger values is visible.
All in all, we find a very consistent picture concerning the description of our data by the specialised $\chi$PT description. Although we are rather careful to quote our results for the deternined low energy constants, $f_0$, $l_3$, $l_4$, $M_{\pm}^{\text{phys}}$, and $c_2$, as final results (in lack of a more sophisticated estimation of systematic uncertainties), we find very good agreement among *all* of them with other [3][24][21] determinations. And finally, we have to come to the same conclusion as the authors of [21], that NLO-$\chi$PT should only be used up to 300 MeV pion masses, which is our largest pion mass in fit I of $\approx 310$ MeV, receiving a downward shift of 3.7% from discretisation and finite volume effects to $\approx 300$ MeV, as it can be seen in figure 2.7.

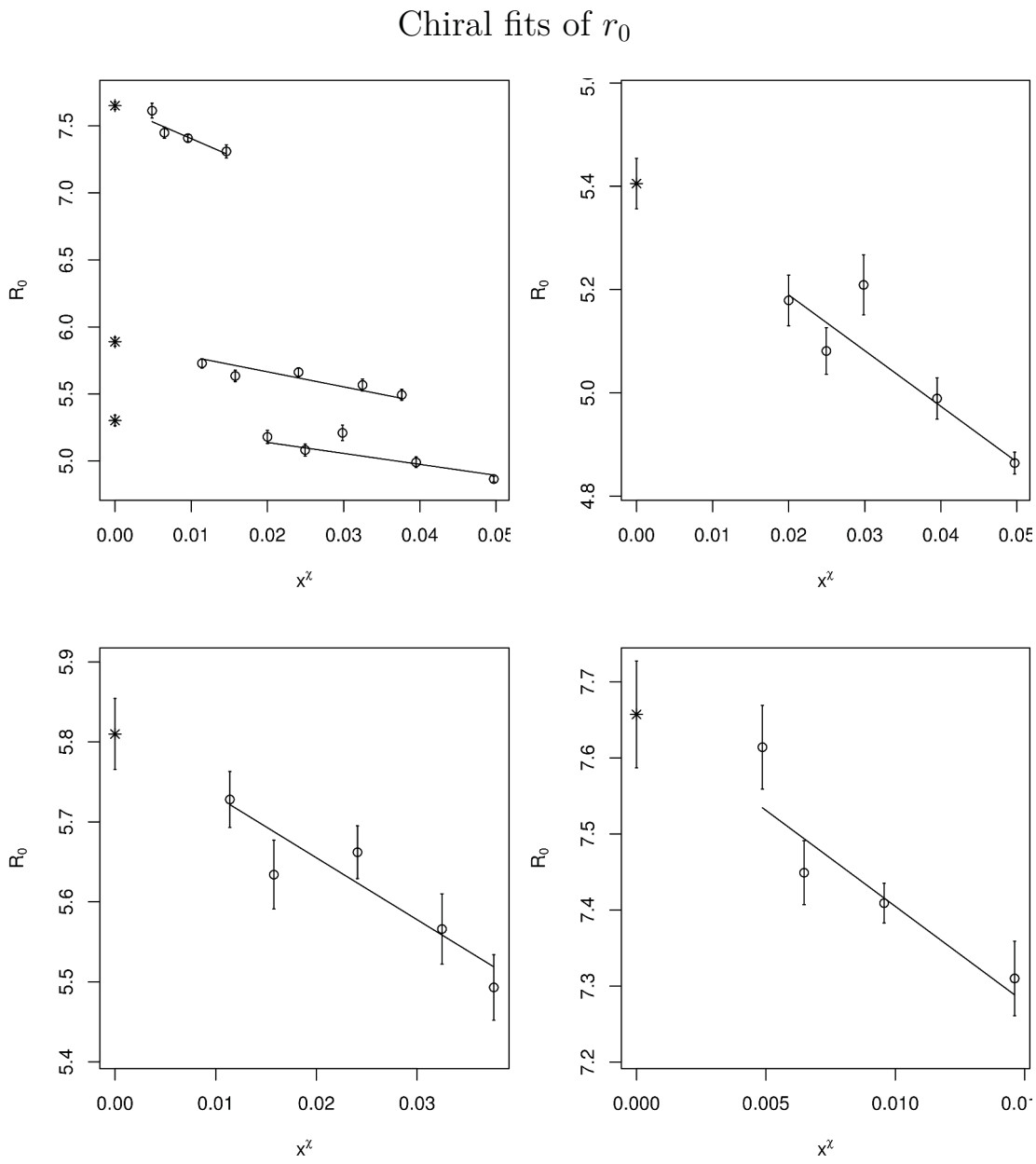


Figure 2.1.: We show the plots of the chiral fits of $r_0$ for the linear fit (see text). The circle symbols correspond to the measured data whereas the star symbol represents the chirally extrapolated value of $r_0$. **(upper-left)** : combined fit of all lattice spacings → as shown in table 2.4 ; The remaining three plots correspond to the fits with a single lattice spacing (as in table 2.5). **(upper-right)** : $\beta = 1.90$ ; **(lower-left)** : $\beta = 1.95$ ; **(lower-right)**: $\beta = 2.10$

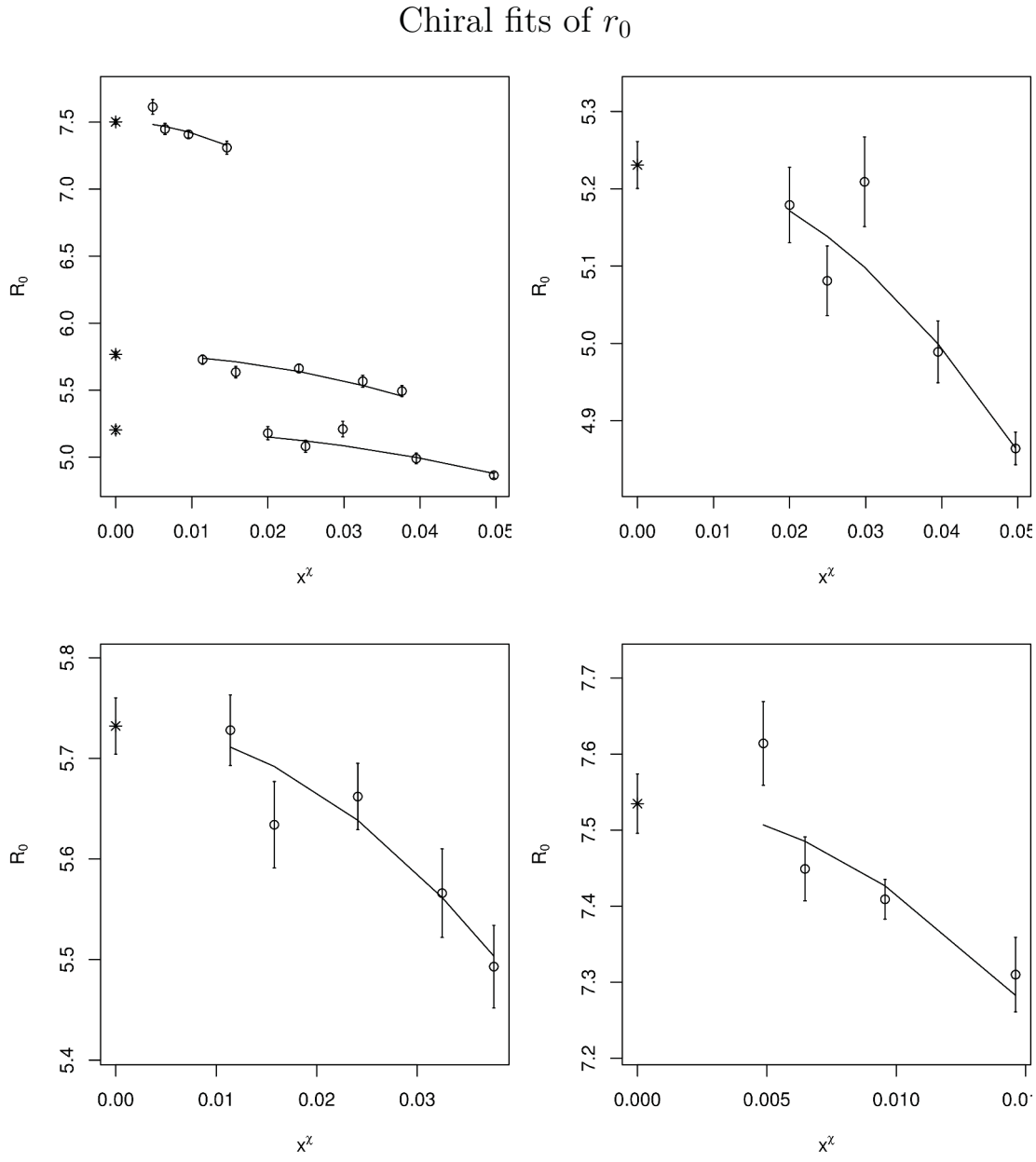


Figure 2.2.: These plots show the chiral fits of $r_0$ for the quadratic fit *without* the linear term. The circle symbols correspond to the measured data whereas the star symbol represents the chirally extrapolated value of $r_0$. **(upper-left)** : combined fit of all lattice spacings → as shown in table 2.4 ; The remaining three plots correspond to the fits with a single lattice spacing (as in table 2.5). **(upper-right)** : $\beta = 1.90$ ; **(lower-left)** : $\beta = 1.95$ ; **(lower-right)**: $\beta = 2.10$

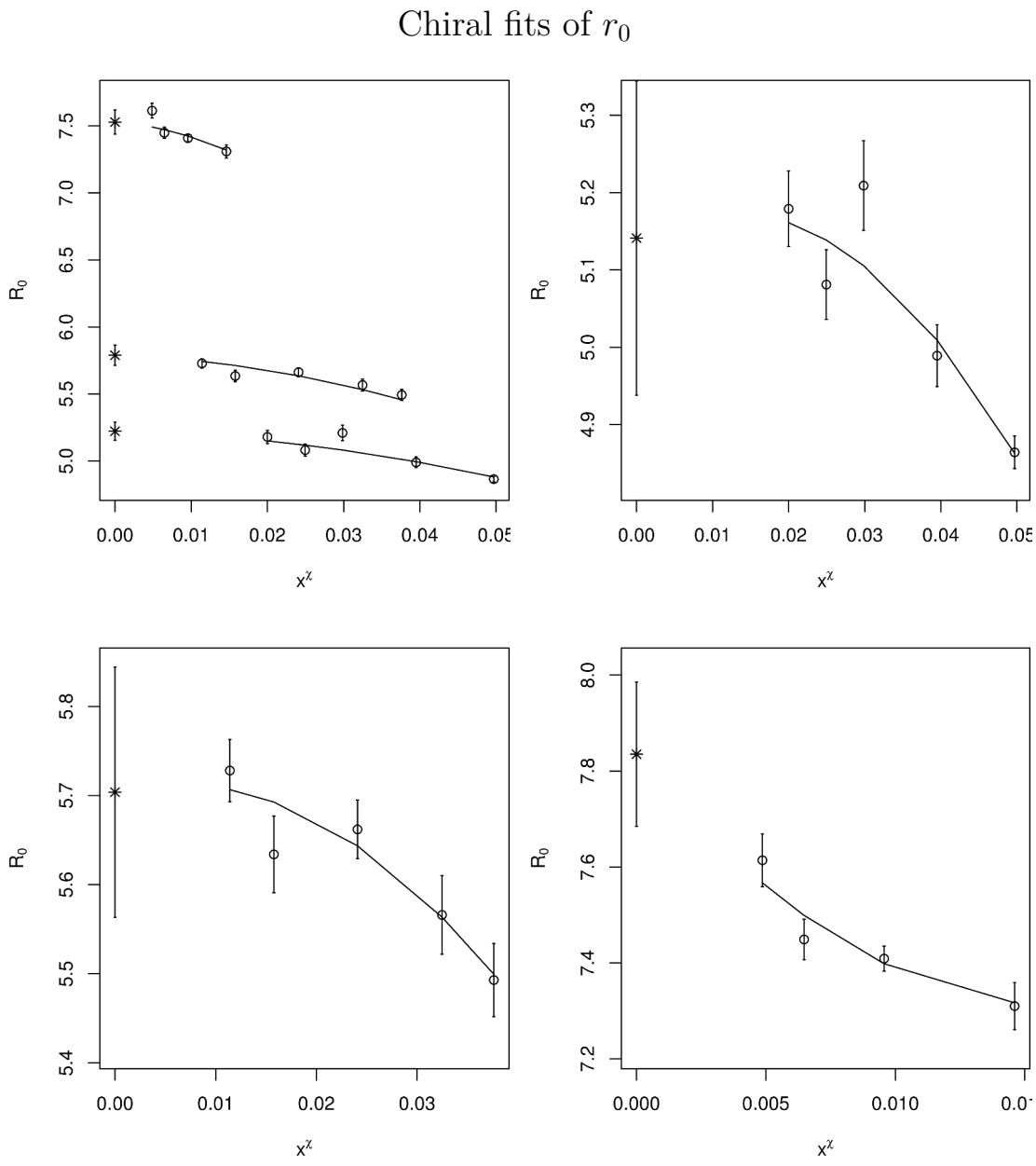


Figure 2.3.: The chiral fits of $r_0$ of the quadratic kind *including* the linear term are displayed in these plots. The circle symbols correspond to the measured data whereas the star symbol represents the chirally extrapolated value of $r_0$. **(upper-left)** : combined fit of all lattice spacings → as shown in table 2.4 ; The remaining three plots correspond to the fits with a single lattice spacing (as in table 2.5). **(upper-right)** : $\beta = 1.90$ ; **(lower-left)** : $\beta = 1.95$ ; **(lower-right)**: $\beta = 2.10$

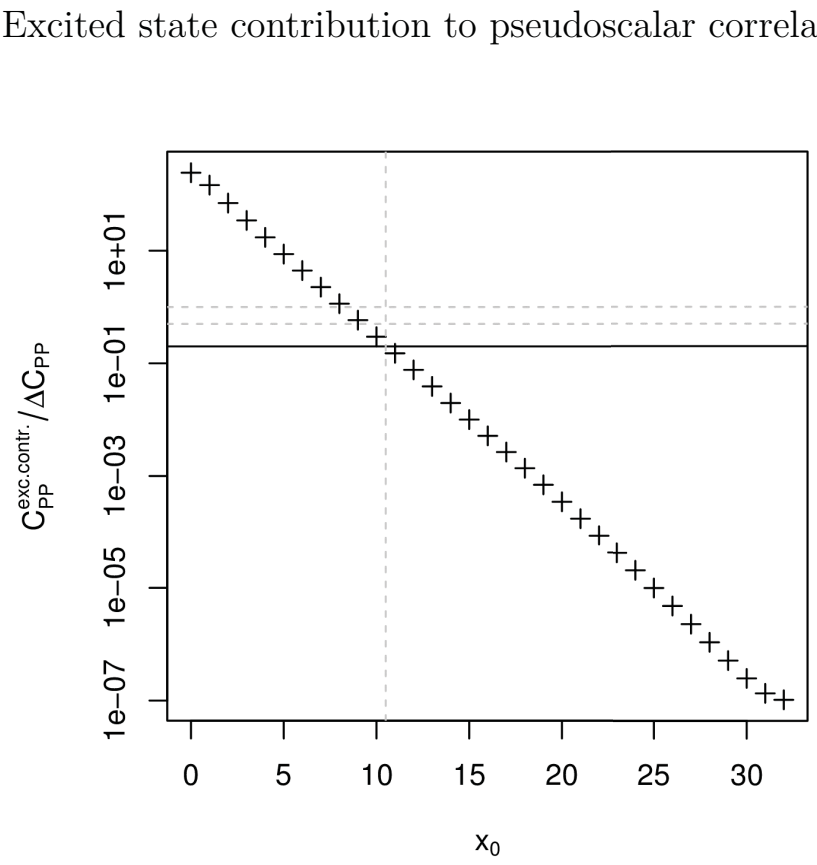


Figure 2.4.: The ratio of the first excited state contribution to the statistical error on the correlator (for ensemble B25.32, see criterion in formula (2.9)). This illustrates the selection of $x_0^{min}$, the optimal starting time slice for the extraction of the pion mass and decay constant from the pseudoscalar correlator. The black line corresponds to a ratio of 0.2. In this specific case $x_0^{min} = 11$ has been determined.

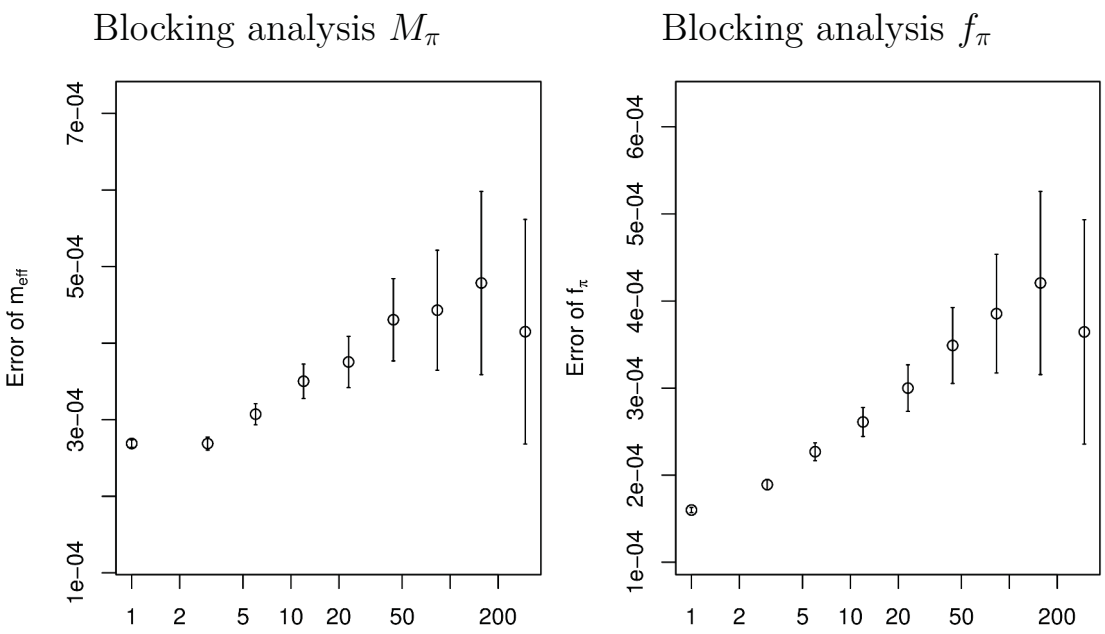


Figure 2.5.: The error of the pion mass (left) and decay constant (right) as a function of the block size (x-axis) in the blocked bootstrap analysis (ensemble B25.32).

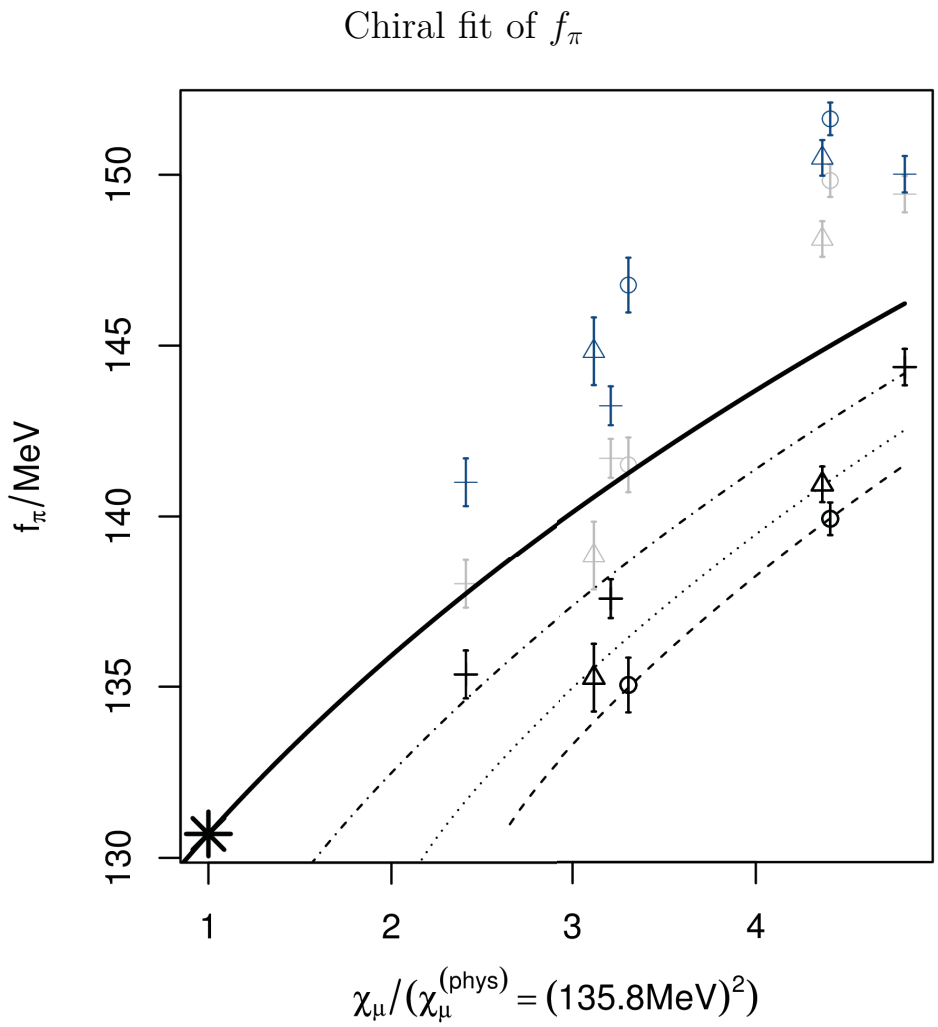


Figure 2.6.: The curves show the chiral fit describing the charged pion **decay constant** for fit **I**. The symbol shapes correspond to the lattice spacings as follows: **circle** $\rightarrow \beta = 1.90$, **triangle** $\rightarrow \beta = 1.95$, **cross** $\rightarrow \beta = 2.10$. The **star** symbol represents the physical point. **Gray** and **blue** symbols refer to the original data and the finite-volume corrected data respectively. The black symbols are finite-volume corrected with discretisation effects taken into account with a term proportional to $a^2$. The remaining discretisation effects only stem from the $a^2$ term in the LO neutral pion mass. The dashed ($\beta = 1.90$), dotted ($\beta = 1.95$) and dash-dotted ($\beta = 2.10$) curves represent the predictions of twisted mass Wilson $\chi$PT at finite lattice spacing. The solid curve shows the continuum $\chi$PT prediction (extrapolation). Look at table 2.9 for numerical results.

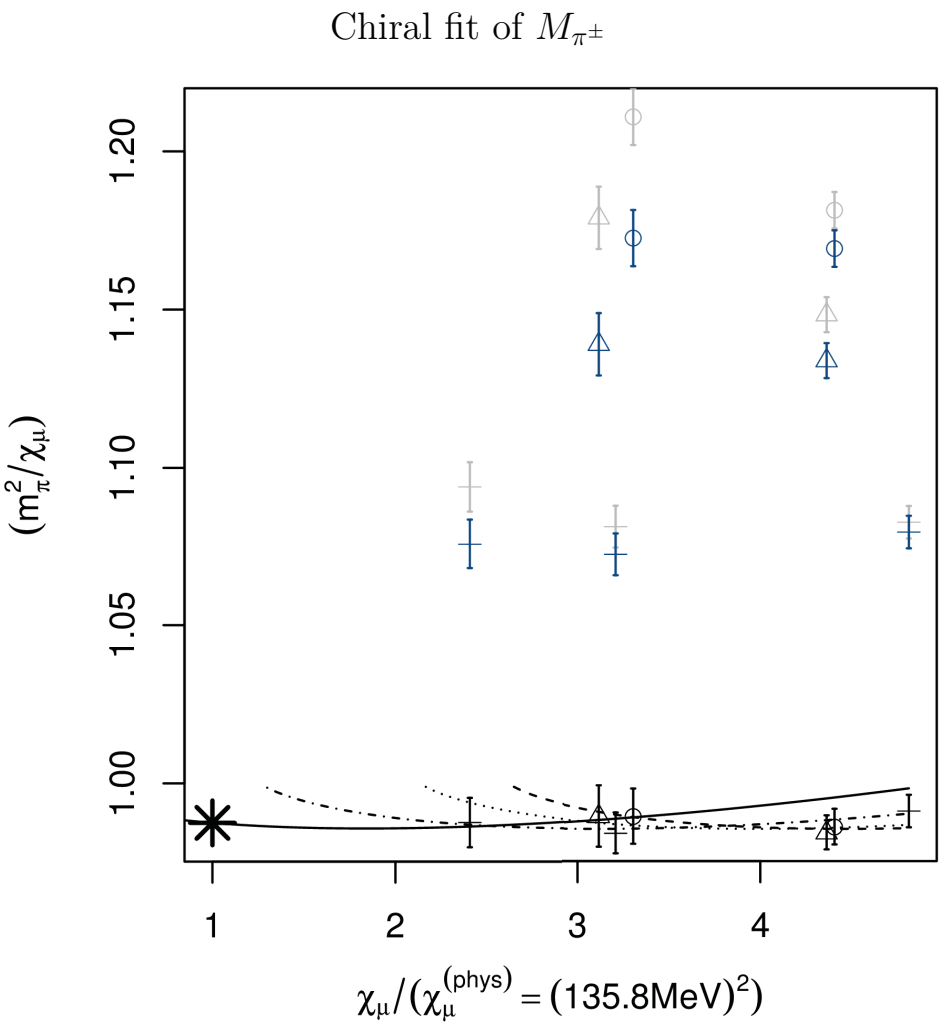


Figure 2.7.: The notation is the same as in figure 2.6 with the only difference that the pion mass (respectively its square scaled with $\chi_\mu$) is shown.

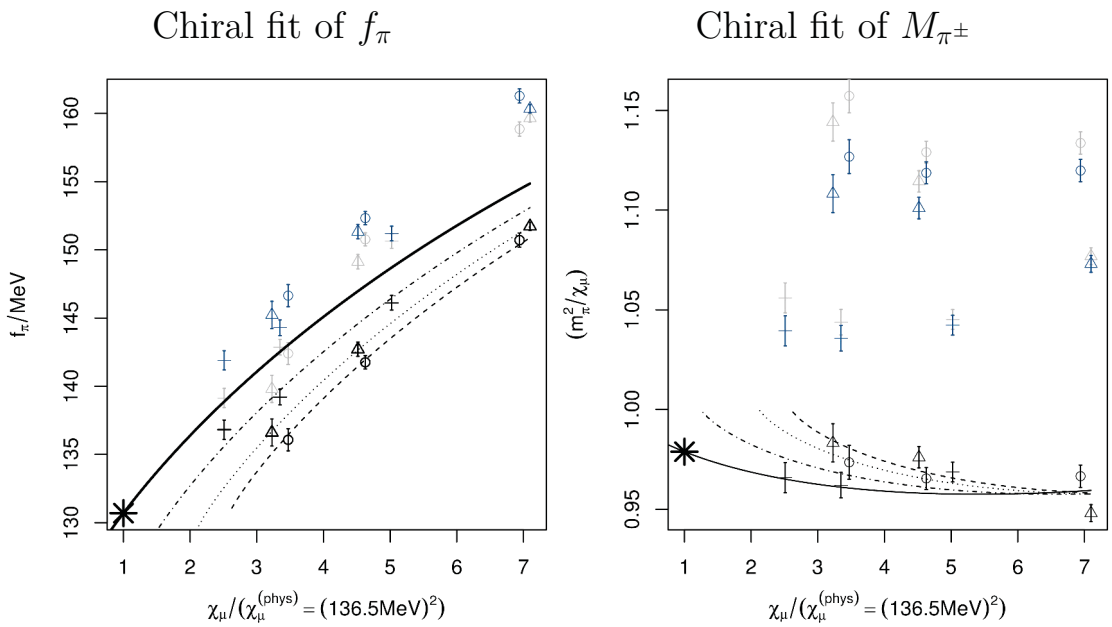


Figure 2.8.: Chiral fits for fit **II**, for details see description of figures 2.6 and 2.7

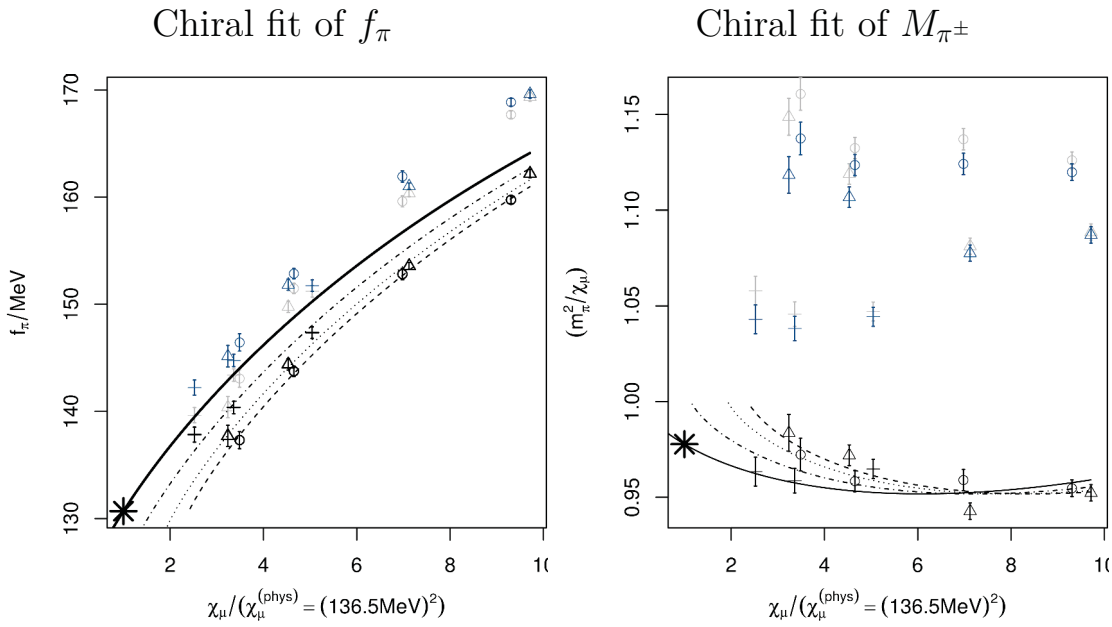


Figure 2.9.: Chiral fits for fit **III**, for details see description of figures 2.6 and 2.7

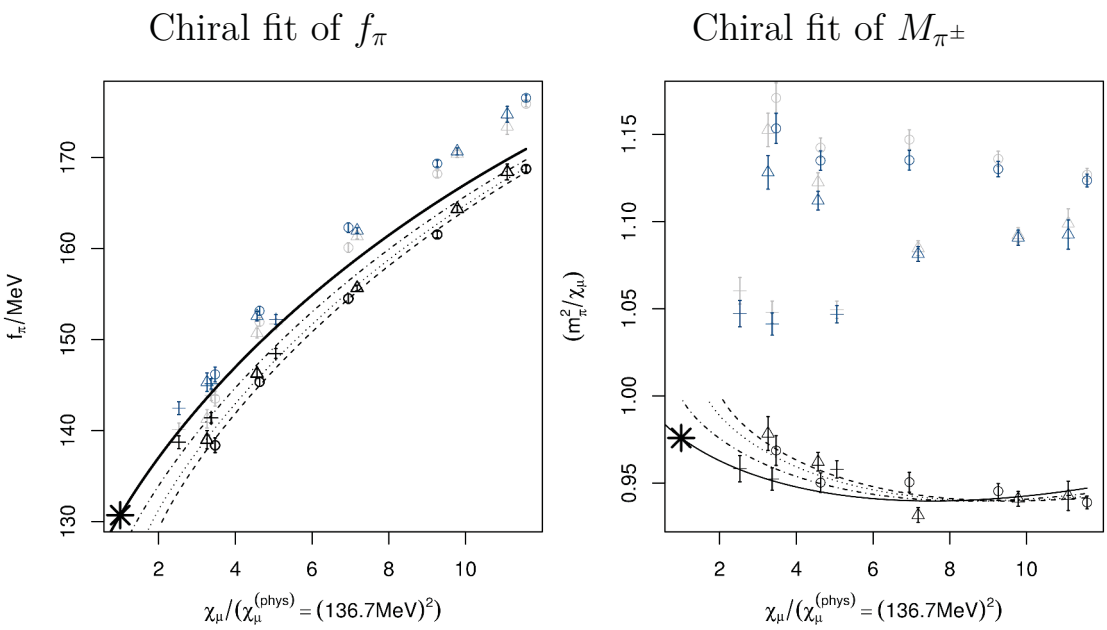


Figure 2.10.: Chiral fits for fit **IV**, for details see description of figures 2.6 and 2.7

# 3. Determination of $f_{D_s}$ in the physical limit

$f_{D_S}$ is the decay constant of the $D_s$ meson, a charged pseudoscalar particle constructed from a strange and a charm quark. Theoretically this quantity is defined in QCD through the following matrix element:

$$\langle 0|\mathcal{A}_\mu(x)|D_s(p)\rangle = -if_{D_s}\, p_\mu\, e^{-ipx}\ , \tag{3.1}$$

as a specialisation of equation 1.50. $|D_s(p)\rangle$ refers to the $D_s$-meson state with four-momentum $p_\mu$. $\mathcal{A}_\mu$ is the axial vector current constructed from a strange and a charm quark field.
$f_{D_s}$ can not be measured directly in experiments but is related to the branching fractions of the leptonic decays [6] $D_s \to \tau\nu$ and $D_s \to \mu\nu$.

$$\Gamma(D_s \to l\nu) = \frac{G_f}{8\pi} f_{D_s}^2 m_l^2 M_{D_s}(1 - \frac{m_l^2}{M_{D_s}^2})|V_{cs}|^2\ . \tag{3.2}$$

Here $l$ is any of the two leptons, the $\tau$-lepton or the muon, $G_f$ the Fermi coupling constant, $m_l$ and $M_{D_s}$ the mass of the lepton and $D_s$-meson respectively and $V_{cs}$ the mixing coefficient between the strange and charm quark in the Cabibbo-Kobayashi-Maskawa (CKM) matrix. The majority of quantities in this expression are known quite precisely with the only exception of $V_{cs}$. Hence, one can determine the product $f_{D_s}^2|V_{cs}|^2$ experimentally with a rather good accuracy as a first step. In a second step, one could either determine $f_{D_s}$ with further experimental or theoretical input about $V_{cs}$ or one determines $V_{cs}$ with theoretical input about $f_{D_s}$.
$f_{D_s}$ is of particular interest, as certain inconsistencies between theoretical predictions from lattice calculations and experimental measurements existed in the past. After a relaxation[1] of the discrepancy in 2010 to $1.6\sigma$, taking the lattice result of $f_{D_s} = 248(2.5)MeV$, from [5], and $f_{D_s} = 257.5(6.1)MeV$, the Particle Data Group world average of this time [37]. The year 2012 revision of the experimental results presented in [6] lead to a value of $f_{D_S} = 260.0(5.4)MeV$, which is again an increase of the tension between theory and experiment to $2.2\sigma$ [2]. If this deviation is taken serious one has to ask for reasons causing such a discrepancy.
A possible question we want to investigate in this work is the influence of the strange and charm quark present in the sea-quark action during our dynamical simulations. To our knowledge this work would present one of the first determinations of $f_{D_s}$ from lattice

[1] In the years before the discrepancy was even larger but most likely also because of the underestimation of uncertainties in theoretical and experimental methods. Since then the methods in both fields have been improved dramatically and hence, led to significantly decreased uncertainties.
[2] Since 2010 no respective lattice results have been published to our knowledge.

QCD with *four* dynamical quark flavours.
In the previous chapter we already discussed the basic simulation parameters of our ensembles like $\beta$, $\kappa_{cr}$ and $\mu_l$ responsible for the lattice scale, tuning to maximal twist, and the light quark mass respectively. Now we want to discuss the tuning of the strange and charm quark masses.

## 3.1. Tuning of the sea strange and charm quark mass

The strange and charm quark mass in our dynamical simulation of these quarks are controlled through the parameters $\mu_\sigma$ and $\mu_\delta$ (see equation (1.9) ).
There exist basically two different approaches to adjust these parameters in order to reflect the correct physical situation. The first one is based on a direct calculation of $\mu_\sigma$ and $\mu_\delta$ from the experimental values of $m_s$ and $m_c$, the strange and charm quark mass respectively. But a precise determination requires detailed knowledge about $Z_P$ and $Z_S$, the renormalisation constants of the pseudoscalar and scalar current respectively. And furthermore the experimental uncertainties ($\approx 5\%$ for $m_s$ [38]) would propagate into the errors of $\mu_\sigma$ and $\mu_\delta$.
Another possibility, that we in fact used, is the tuning of $\mu_\sigma$ and $\mu_\delta$, such that on the lattice the physical kaon and D-meson masses are obtained after the continuum limit and the limit to the physical light quark mass have been taken. The result is shown in table 3.1 and illustrated in figure 1, page 4, in [39]. This illustration can be understood

| $\beta$ | $\mu_\sigma$ | $\mu_\delta$ |
|---|---|---|
| 1.90 | 0.150 | 0.19 |
| 1.95 | 0.135 | 0.170 |
| 2.10 | 0.120 | 0.1385 |

Table 3.1.: Parameters of $\mu_\sigma$ and $\mu_\delta$ used in our simulations for the different values of $\beta$

as follows: $\mu_\sigma$ controls the average of the strange and charm quark mass, whereas $\mu_\delta$ takes direct influence on their difference. Hence one can increase (decrease) the kaon and D-meson mass simultaneously with an upwards (downwards) shift of $\mu_\sigma$. If $M_K$ and $M_D$ are too close (distant) to each other one needs to increase (decrease) $\mu_\delta$. This procedure is continued until the experimental values of $M_K$ and $M_D$ are reproduced in the physical limit, as indicated above. Nevertheless, the number of tuning steps is limited by the available computer resources, such that one has to finalise the tuning at some point, maybe not having achieved the highest possible precision of the parameters.
An important point during the aforementioned tuning is the actual measurement of $M_K$ and $M_D$. To reflect the correct physical situation with respect to the quark masses, the sea-quark action (1.7) for the strange and charm quarks was used to construct the kaon and $D$-meson correlation functions[3] from which the masses were determined. Certain

[3]This was referred to as the unitary setup in chapter 2, subsection 1.1.3.

subtleties related to parity and flavour symmetry breaking arose in this connection and are discussed in [12] together with the detailed methods for the determination of the kaon and D-meson masses in the unitary setup.
The measured kaon and D-meson masses are shown in figure 3.1 and are also given in table B.2 in the appendix B.

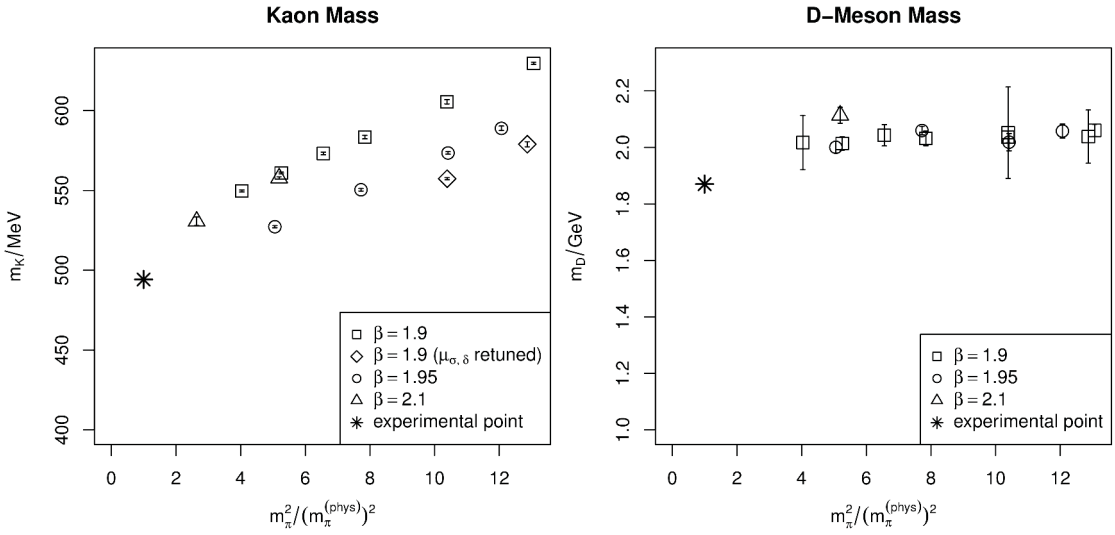


Figure 3.1.: Kaon and D-meson masses determined on our ensembles as a result of the strange and charm quark mass tuning

Assuming the absence of large discretisation and finite size effects, it seems that in the case of the kaon mass (left plot, figure 3.1) the data for $\beta = 2.1$ and $\beta = 1.9$ lead to a slightly larger Kaon mass at the physical point, whereas the kaon masses at $\beta = 1.95$ seem to match the physical point very well assuming a linear behaviour with the squared pion mass. To study the influence of a smaller strange sea-quark mass we have generated the ensembles $A80.24s$ and $A100.24s$, visible as diamond symbols at the right margin of the plot, which are not in line with the square symbol points from $\beta = 1.9$. These ensembles have been simulated exactly with the same parameters as the corresponding ensembles, A80.24 and A100.24, except the parameter $\mu_\delta$, which has been set to 0.197 and the critical hopping parameter $\kappa_{cr}$, retuned to 0.163204 (A80.24s) and 0.163196 (A100.24s), according to the maximum twist criterion.
Looking at the D-meson masses (right plot, figure 3.1) we see that the data points seem to form a horizontal plateau situated slightly above $2GeV$. If we assume the absence of visible discretisation effects, we would conclude that the charm quark mass at the physical point is larger than its physical value.
Nevertheless, a high precision tuning of the sea-strange and -charm quark mass does not seem to be too important as we are going to measure the meson masses and decay constants in the mixed action setup where we can adjust the strange and charm quark mass as required. A reasonable argumentation for this will be given later when we

compare fit results including the ensembles A100.24s and A80.24s with fits excluding them.
This brings us to the next topic we want to discuss, namely the chosen valence quark masses and the measurement of the meson masses and decay constants in the mixed action setup, which we started to discuss in 1.1.3, chapter 1.

## 3.2. Measurement of meson masses and decay constants

As discussed in 1.2.4, we have constructed and measured pseudoscalar correlators representing the kaon and $D_s$-meson. Additionally we have also measured the mass $M_{ss}$ of the strange-quarkonium[4] which will be used as a proxy for the actually simulated valence strange quark mass. As we do not know the physical strange and charm quark mass[5] in lattice units before the scale setting and renormalisation constant determination we have measured correlators with several strange and charm quark masses for each lattice spacing in a region most likely including the physical quark masses. This has been illustrated for the kaon mass in figure 3.2 for ensemble A40.32. In this way, we can bracket the physical meson masses which allows to finally perform an only small interpolation for the decay constants. Hence, we have chosen the strange quark masses $\mu_s$ in table 3.2 and the charm quark masses $\mu_c$ in table 3.3. The kaon, $D_s$-meson and

| $\beta \rightarrow$ | 1.90 | 1.95 | 2.10 |
|---|---|---|---|
| $\mu_s^1$ | 0.0135 | 0.0130 | 0.0110 |
| $\mu_s^2$ | 0.0150 | 0.0145 | 0.0120 |
| $\mu_s^3$ | 0.0170 | 0.0160 | 0.0130 |
| $\mu_s^4$ | 0.0190 | 0.0180 | 0.0150 |
| $\mu_s^5$ | 0.0225 | 0.0210 | 0.0180 |
| $\mu_s^6$ | 0.0240 | - | - |

Table 3.2.: Strange quark masses $\mu_s$ in lattice units used for the measurement of kaon and $D_s$ meson correlators

strange-quarkonium correlators have been analysed as described in the previous chapter, chapter 2, section 2.3, where the pion correlator analysis was presented. Due to the many possible combinations of valence quark masses, the results are numerous. This is the reason why we disregarded to list all results in extensive tables in the appendix. Nevertheless, the relevant data, including the bootstrap samples, can be requested from

[4]This is an artificial pseudoscalar meson constructed from a strange and an anti-strange quark. Hence, $\mu_1$ *and* $\mu_2$ is set to the considered strange quark mass in the mixed action setup (described in chapter 1, subsections 1.1.3 and 1.2.4).

[5]defined through the correct continuum and chiral limit (with respect to the experimental values) of the kaon and D-meson mass or any other observables sensitive to the corresponding quark masses

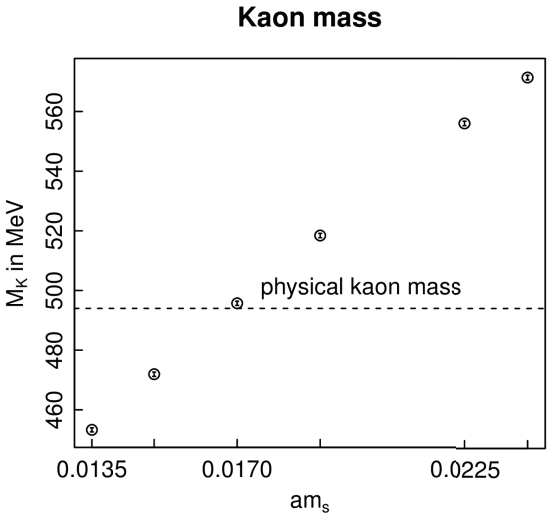


Figure 3.2.: Kaon masses determined from ensemble A40.32 in the mixed action setup for various strange quark masses, enclosing the region of the physical kaon/strange mass, **x-axis:** unrenormalised strange quark mass in lattice units as given in table 3.2, **y-axis:** measured kaon mass in physical units, **dashed line:** experimental kaon mass, bracketed by the points at $am_s = 0.015$ and $am_s = 0.017$

the author[6].

## 3.3. Extrapolation of $f_{D_s}$ to the physical point

In the previous section we have discussed the determination of the raw lattice data for the pseudoscalar masses and decay constants. Using the results of the scale setting (2.19), at the end of chapter 2 we can convert the lattice results to physical units. But it is still necessary to perform the continuum extrapolation ($a \to 0$) and the extrapolation to the physical light quark mass. In order to do this, we have fitted our data to the following two models, discussed already in chapter 1, subsection 1.3.3, but we repeat them here for the sake of clarity:

$$\Phi_{D_s} = f_{D_s}\sqrt{M_{D_s}} = D_1\left[1 + D_2\xi + D_a a^2 + D_{ah} a^2 M_{D_s}^2\right] + \frac{D_3}{M_{D_s}} \tag{3.3a}$$

$$R_1 = \frac{f_{D_s}\sqrt{M_{D_s}}}{f_K} = D_1\left(1 + A_1 a^2 + A_2 a^2 M_{D_s}\right)\left(1 + \frac{3}{4}\xi\ln\xi + D_2\xi\right) + \frac{D_3}{M_{D_s}}\ . \tag{3.3b}$$

[6] Andreas Ammon, NIC, DESY Zeuthen, Platanenallee 6, D-15738 Zeuthen, Germany, contact also via Karl Jansen (Karl.Jansen@desy.de), E-Mail: Andreas.Ammon@desy.de or nubi@freenet.de

| $\beta \rightarrow$ | 1.90 | 1.95 | 2.10 |
|---|---|---|---|
| $\mu_c$ | 0.210 | 0.200 | 0.165 |
| | 0.225 | 0.215 | 0.180 |
| | 0.260 | 0.240 | 0.200 |
| | 0.285 | 0.260 | 0.225 |
| | 0.310 | - | 0.250 |

Table 3.3.: Charm quark masses $\mu_c$ in lattice units used for the measurement of $D_s$ meson correlators

We recall that formula (3.3a) describes the chiral extrapolation of the quantity $\Phi_{D_s} = f_{D_s}\sqrt{M_{D_s}}$ based on results of heavy meson chiral perturbation theory (HM-$\chi$PT), having the advantage of a mild chiral behaviour. (3.3b) describes the chiral behaviour of $R_1 = \frac{f_{D_s}\sqrt{M_{D_s}}}{f_K}$ and is described by a combination of HM-$\chi$PT and conventional SU(2)-$\chi$PT ($\chi$PT for the light quark sector). The advantage of considering $R_1$ is the cancellation of discretisation effects in this quantity. The variable $\xi_{ss} = \frac{2Bm_s}{(4\pi f_0)^2}$, appearing as a linear term in some of the coefficients in formulae (3.3), has been constructed from the strange-quarkonium mass (mentioned in the previous section) by identifying $M_{ss}$ with the leading order strange-quarkonium mass $2Bm_s$:

$$\xi_{ss} = \frac{M_{ss}(\mu_s)^2}{(4\pi f_0)^2} \ , \tag{3.4}$$

where $M_{ss}(\mu_s)$ has been written to underline the dependence on the valence strange quark mass. In this way, an explicit determination of the strange quark mass can be avoided. $M_{ss}$ is the mass of a pseudo-physical state which does not exist in nature. But in the framework of the mixed action setup one can formally define such an object as a pseudoscalar meson consisting of a strange quark and a strange anti-quark. We define[7] the pseudo-physical value of this state as:

$$M_{ss}^{pp} = \sqrt{2(M_K^{phys})^2 - (M_\pi^{phys})^2} \ . \tag{3.5}$$

In principle one could apply the whole data set with all possible combinations of strange and charm quark masses to the fit formulae (3.3). And this would lead in fact to a very good description of our data. But to verify a good description, especially in the region of the physical strange and charm quark masses, we select only those two quark masses, separately for strange and charm, which lead to values of $M_{ss}$ and $M_{D_s}$ being the closest to the pseudo-physical $M_{ss}^{pp}$ and the physical value $M_{D_s}^{phys}$ respectively. More explicitly, if we form an interval $[M_{ss}(\mu_s^1), M_{ss}(\mu_s^2)]$ we would select $\mu_s^{1,2}$ such that $M_{ss}^{pp}$, defined above, is included in the interval. Then we proceed in the same way with the

[7] This definition is motivated by the leading order expressions for $M_K$, $M_\pi$ and $M_{ss}$ in $\chi$PT.

charm quark masses $\mu_c^{1,2,3,4}$ by considering the intervals $[M_{D_s}(\mu_s^1, \mu_c^1), M_{D_s}(\mu_s^1, \mu_c^2)]$ and $[M_{D_s}(\mu_s^2, \mu_c^3), M_{D_s}(\mu_s^2, \mu_c^4)]$ chosen to include the physical $D_s$-meson mass.
After the fit parameters of equations (3.3) have been determined by a $\chi^2$-minimisation, the continuum value of $\Phi_{D_s}$ and $R_1$ is extrapolated to the physical point by performing the limits

- $a \to 0$,
- $M_\pi$ to its physical[8] value $M_\pi^{phys} = 134.8\text{MeV}$,
- $M_{D_s}$ to its physical[9] value $M_{D_s}^{phys} = 1968.5\text{MeV}$,
- $M_{ss}$ to its pseudo-physical value $M_{ss}^{pp} = 685.8\text{MeV}$ (assuming[8] $M_K^{phys} = 494.2MeV$)

in the fit formulae. The physical value of $f_{D_s}$ is then obtained by multiplying $\Phi_{D_s}$ with $\left(M_{D_s}^{phys}\right)^{-\frac{1}{2}}$ and $R_1$ with $\left(M_{D_s}^{phys}\right)^{-\frac{1}{2}} f_K^{phys}$, assuming $f_K^{phys} = 156.1\text{MeV}$ (the experimental average [6]).

As in the previous chapter we have used the blocked bootstrap samples from the correlator fits also in the chiral fits for the analysis of statistical errors. Additionally, for taking into account the uncertainties of the scale setting, we have generated synthetic bootstrap samples for the lattice spacings $a(\beta)$ by assuming[10] a normal distribution, the statistical and systematic error (added in quadrature) taken as the standard deviation.

Finally we have performed fits to the two models (3.3) with two sets of ensembles each, resulting in four different fits. Fits I and II, involve all twelve ensembles, A30.32, A40.32, A50.32, A60.24, A80.24, A100.24, B35.32, B55.32, B75.32, B85.24, D15.48 and D30.48. To investigate the influence of a pion mass cut at around $380MeV$, we performed fits III and IV that exclude ensembles A80.24, A100.24, B75.32 and B85.24. The correlation matrix has a very large condition number due to strong correlations of values stemming from the same ensemble. This would make correlated fits very unstable, and would lead to large statistical errors. Hence, we performed uncorrelated fits which show a much higher stability. The results are listed in table 3.5. The first column shows the mapping of fit labels to the fit model (column two) and the corresponding fitted quantity (column three). Column four and five contain information about the quality of the fit through the minimum value of the $\chi^2$-function, the degrees of freedom dof, and the resulting p-value respectively. The last column shows the result for the continuum values at the physical point for $f_{D_s}$, obtained from the corresponding fit. The detailed fit parameters can be found in appendix C, table C.1. A plot of the results for fit I is shown in figure 3.3, for fit II in figure 3.4, for fit III in figure 3.5 and for fit IV in figure 3.6.

[8] Instead of the experimental value we use pion and kaon masses in the isospin limit ($m_u \to m_d$) corrected for electromagnetic effects as discussed in [7].
[9] In this case we rely on the experimental average by the PDG [38].
[10] This assumption has been verified for the statistical errors by an analysis of the bootstrap samples from the chiral fits in the pion sector (in the previous chapter).

| fit | model | fitted quantity | $\chi^2$/dof | p-value | $f_{D_s}$/MeV |
|---|---|---|---|---|---|
| I | (3.3a) | $\Phi_{D_s}$ | 29.4 / 40 | 0.891 | 248.6(4.3) |
| II | (3.3b) | $R_1$ | 17.1 / 41 | 0.99965 | 250.9(3.6) |
| III | (3.3a) | $\Phi_{D_s}$ | 19.4 / 24 | 0.728 | 247.1(4.7) |
| IV | (3.3b) | $R_1$ | 9.65 / 25 | 0.9975 | 249.1(3.6) |

Table 3.5.: Fit results of the chiral fits to $\Phi_{D_s} = f_{D_s}\sqrt{M_{D_s}}$ and $R_1 = \frac{\Phi_{D_s}}{f_K}$ and extrapolation result in the continuum for $f_{D_s}$.

The first observation, we can deduce from the p-values [11], is that the fitted functional forms describe the data very well. From the figures (3.3,3.4,3.5,3.6) we see that all data points are not more than $2\sigma$ (with respect to their own error) away from their prediction. Predictions from all the fits (I-IV) for $f_{D_s}$ agree very well within their statistical errors. Nevertheless, the prediction of $f_{D_s}$ based on the fits to $\Phi_{D_s}$ (fits I and III) always leads to smaller values than the fits to $R_1$ (fits II and IV) compared on the same set of ensembles. This seems to be due to the different chiral extrapolation strategies. Hence, we can take the deviations in this context as an approximation of chiral extrapolation uncertainties, given by 2.1MeV (fit I vs. II) and 2.3MeV (fit III vs. IV). Taking the larger of the two, this uncertainty also includes the deviations with respect to the exclusion of heavier pion masses, when comparing for example fit II and IV.

Information about uncertainties originating from the lattice spacings can be obtained from setting their errors to zero in the bootstrap procedure. Significant decreases in the error could only be observed for fit I and III. The errors decrease from 4.3 to 3.0MeV for fit I and from 4.7 to 3.5MeV for fit III.

As mentioned at the end of section 3.1, we performed a fit including the ensembles A80.24s and A100.24s. The results indicate that the influence of a slight miss-tuning of the strange and charm sea-quark mass is rather small, as no significantly different results are obtained. Turning the argument around, we can conclude that the effect of partially quenching[12] of the strange and charm quark is rather small. Nevertheless, a dedicated and more sophisticated analysis should verify these assumptions in detail.

Furthermore, we have to mention that, as in the case of the pion decay constant, one would need to estimate the effects of a pure QCD simulation, neglecting electromagnetic effects from QED. An investigation in this direction however, goes beyond the scope of this work.

The extrapolation results of all fits are very consistent, and we take their mean as our

[11] See sec. 1.4.3, chapter 1 for a brief introduction.

[12] Partially quenching of a quark means that its mass is different in the simulation and in observables involving the corresponding quark field (for example the pseudoscalar density).

final result:

$$f_{D_s} = 248.9(4.7)_{\text{stat}}(2.3)_{\text{chiral}}\text{MeV} \qquad (3.6)$$
$$f_{D_s} = 248.9(5.3)_{\text{comb.}}\ \text{MeV}$$

Conservatively, we have taken the largest value in each category of uncertainties and added up the errors in quadrature to compute the combined error in the second line. We have plotted our result together with the $N_f = 2 + 1$ results from [5] (HPQCD collaboration, 2010), preliminary $N_f = 2 + 1 + 1$ results from the Lattice 2013 talk [40] (Fermilab/MILC collaboration, 2013), the year 2009 $N_f = 2$ results from the ETM collaboration [4] and the most recent particle data group average from 2012 [6] in figure 3.7. Looking at this figure we can conclude that our result is about $2\sigma$ below the PDG average. We find only a minor upwards shift of our result compared to other lattice determinations with less fermion flavours in the sea ($N_f = 2$ and $N_f = 2 + 1$). Perfect agreement is found with the preliminary result with $N_f = 2 + 1 + 1$ sea-quarks by the Fermilab and MILC collaboration. As mentioned before we expect further small uncertainties from the miss-tuning or partially quenching of the strange and charm quark mass respectively. More significant systematic uncertainties could originate from neglected electromagnetic effects, possibly explaining the still existing tension between lattice and experimental results. Nevertheless, definite conclusions about the influence of the number of sea quark flavours on the value of $f_{D_s}$ can only be drawn in the future when the overall error of $f_{D_s}$ has been reduced further.

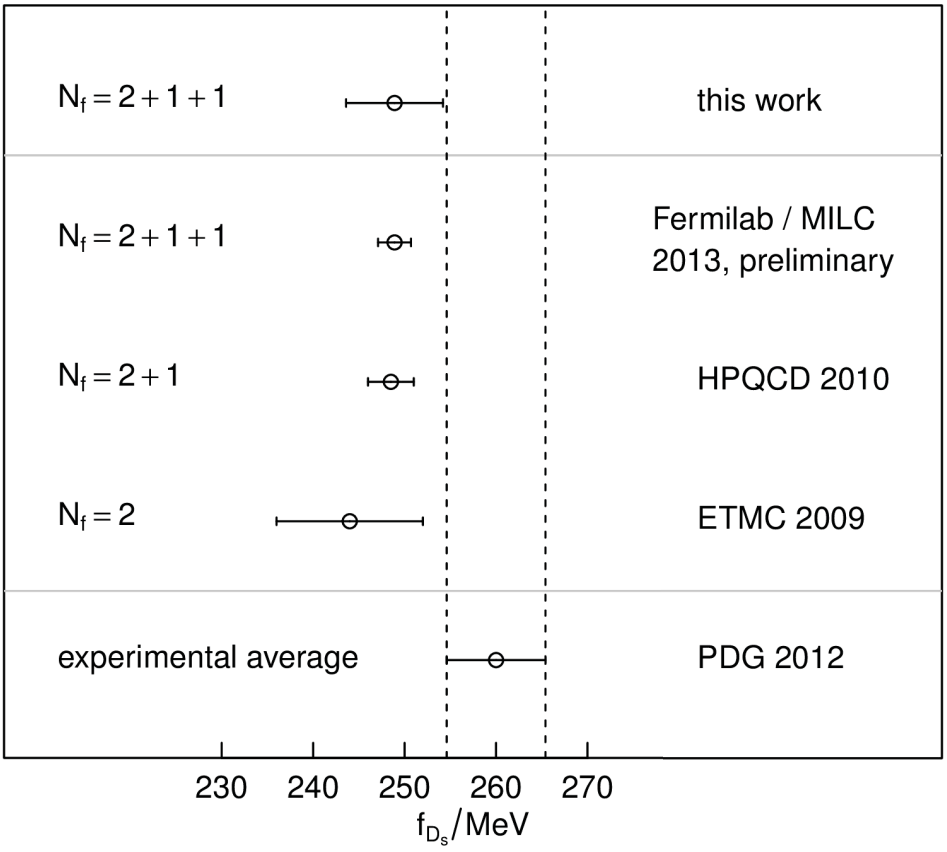


Figure 3.7.: Comparison of our result for $f_{D_s}$ with others obtained with the same or less numbers of sea quark flavours from lattice-QCD: [4] ($N_f = 2$, ETMC, 2009), [5] ($N_f = 2 + 1$, HPQCD collaboration, 2010), [40] ($N_f = 2 + 1 + 1$, Fermilab/MILC collaborations, 2013, preliminary results) and experimental average from PDG [6]

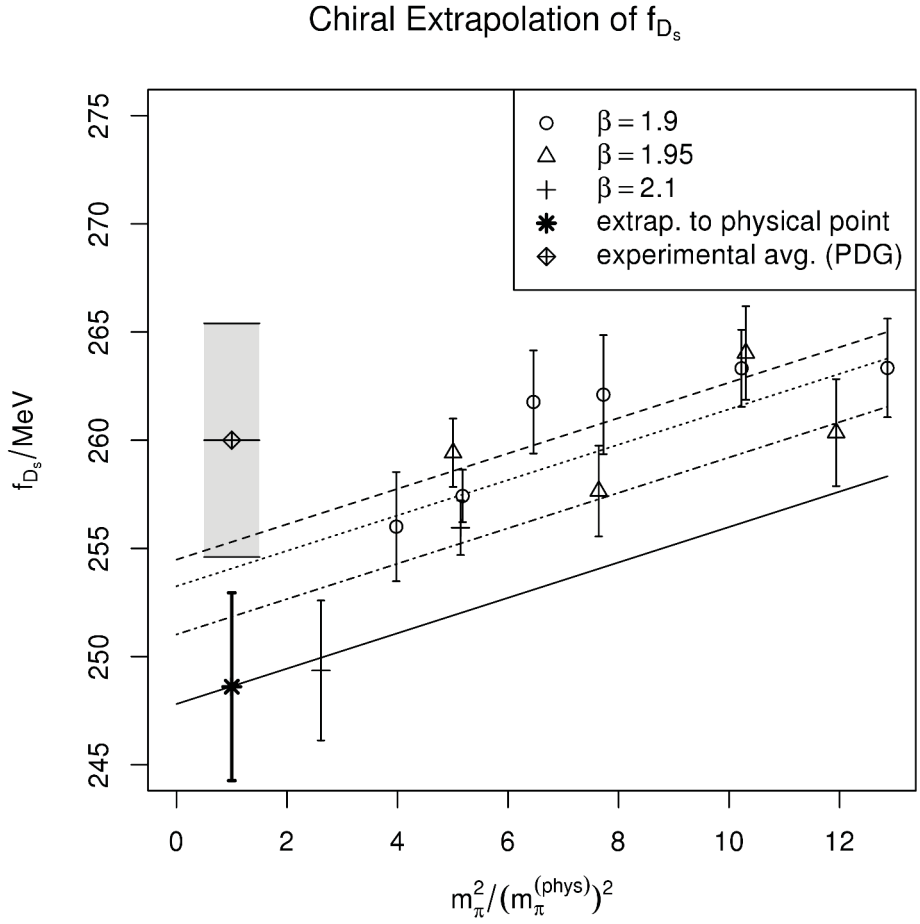


Figure 3.3.: The curves are the results for the chiral fit of $\Phi_{D_s}$ (described by formula (3.3a)) with pion masses up to $\approx 485MeV$. We note, that all data points and the describing fit funtion have been multiplied with $\sqrt{M_{D_s}^{\text{phys}}}$, such that the y-axis is in units of $f_{D_s}$. The circle, triangle and cross symbols represent the fitted data points at the corresponding value of $\beta$ as indicated in the legend. The dashed ($\beta = 1.9$), the dotted ($\beta = 1.95$) and the dash-dotted ($\beta = 2.1$) line show the predictions at finite lattice spacing whereas the solid black line stands for the continuum prediction which leads at the physical pion mass to the extrapolation result for $f_{D_s}$ depicted by the asterisk symbol (with error bars accounting for statistical errors). The experimental point from the 2012 revision [6] of the PDG average is shown as the diamond symbol, and the grey shaded area is the overall uncertainty of the experimental average.

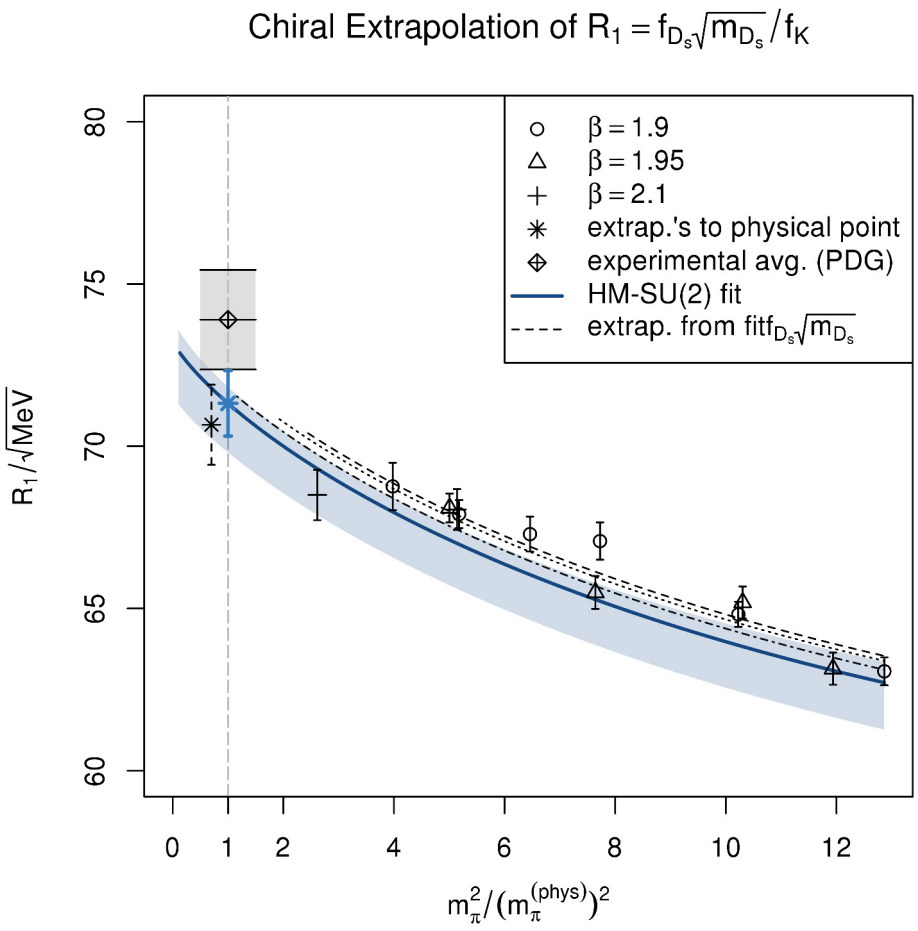


Figure 3.4.: The chiral fit of $R_1$ corresponding to formulae (3.3b) (blue curve) ( $M_\pi \leq 485 MeV$). The meaning of the symbols is as in the previous figure 3.3. The dashed, dotted and dash-dotted curves represent the prediction of formula (3.3b) at finite lattice spacing, $\beta = 1.9;\ 1.95;$ and 2.1 in this order. The continuum prediction for $R_1$ is shown as the blue asterisk. The black asterisk symbol with dashed error bars represents the continuum extrapolation result from the fit to formulae (3.3a) (shown in figure 3.3 ). Both asterisk symbols are supposed to lie at the physical pion mass marked by the grey dashed vertical line at $\frac{M_\pi^2}{(M_\pi^{\rm phys})^2} = 1$. Only the black point has been slightly set off from this line for a better visibility.

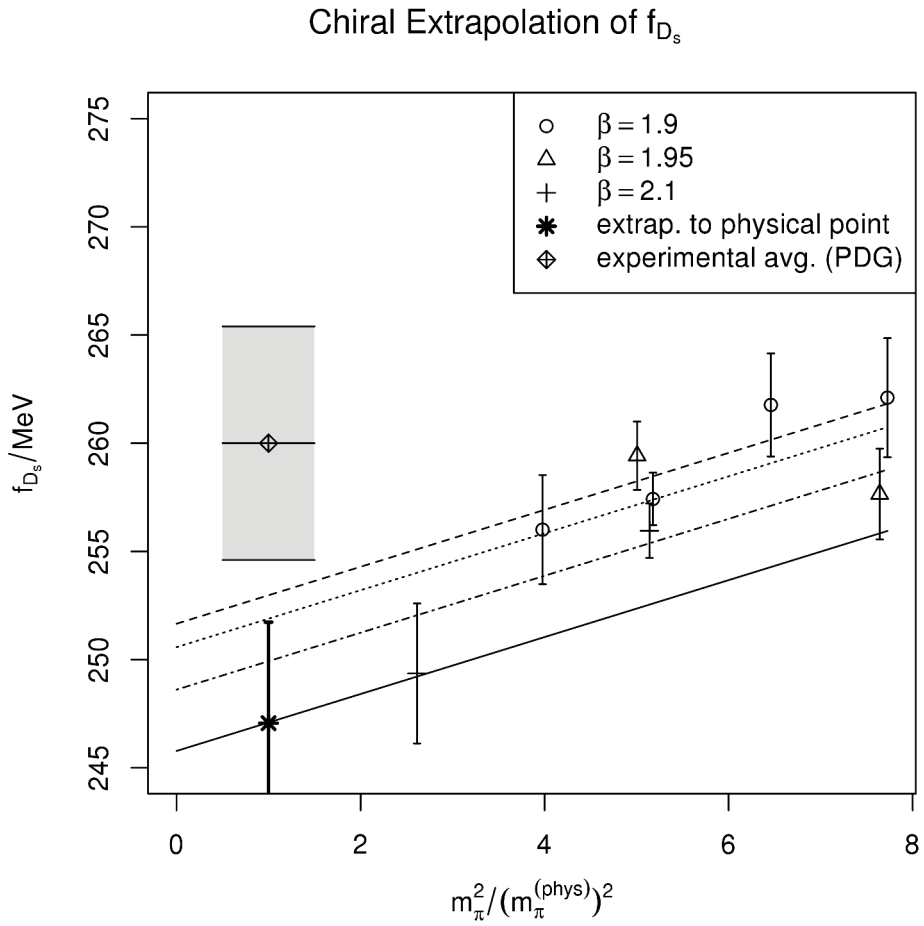


Figure 3.5.: These curves show the fit results for $\Phi_{D_s}$ with pion masses only up to $\approx 380MeV$. The notation is as in the description of figure 3.3, where the fit was performed with pion masses up to 485MeV.

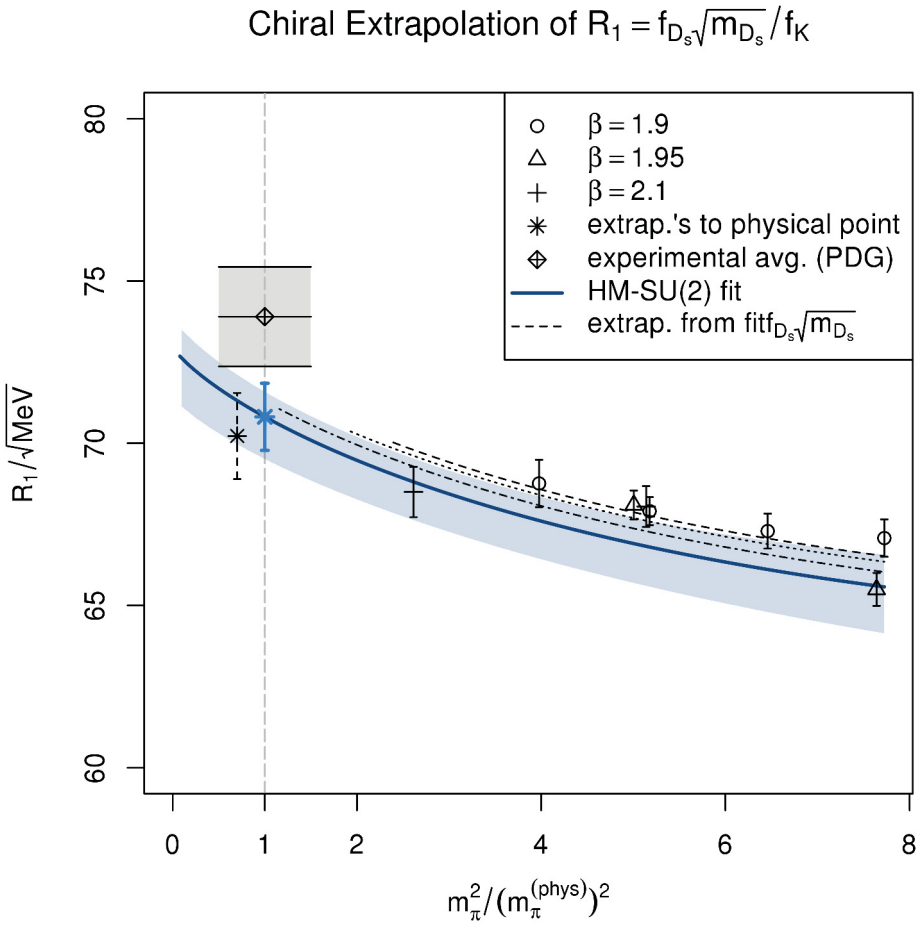


Figure 3.6.: The chiral fit of $R_1$ corresponding to formulae (3.3b) (blue curve) with pion masses $M_\pi \leq 380MeV$. Notation is as in the description of figure 3.4 where the same fit was performed with pion masses up to 485MeV.

# 4. Lattice simulations with quasi-Monte Carlo: an applicability study

Based on the favourable properties of the quasi-Monte Carlo method and our first experiences we made with this technique, we see an enormous potential, if this approach can eventually be applied to gauge theories, maybe even with fermions, as substantial gains in simulations could be obtained. Already now, the method can be tested for the computation of disconnected diagrams which appear in many interesting observables of QCD, like flavour singlet quantities and matrix elements of scalar operators.
Hence, we are highly motivated to undertake applicability studies of the QMC method for physical systems. Before coming to sophisticated models like lattice-QCD, the method should be able to proove its efficiency for less complicated models. Thus, such studies should commence with rather simple applications and should continue step by step to the extent it overcomes the given problems.
According to this, this chapter is devoted to the direct application of the quasi-Monte Carlo method (QMC) to actual, rather basic lattice problems, like the harmonic and anharmonic oscillator. But we also want to give a perspective on further applications with a much farther reach, and discuss next directions on the way to their realisation.
One of the more elaborate applications, discussed in chapter 1, subsection 1.2.3, was the stochastic estimation of the trace of a matrix $M$ formulated as the stochastic estimation of a weighted $\chi^2$-function (1.45). This was taken as a toy model for the stochastic estimation of disconnected diagrams contributing to the neutral pion correlation function. We indicated that the QMC method could offer an improved error convergence in such cases. But a necessary prerequisite for this was the transformation to the eigenbasis of the matrix $M$ where the components of the stochastic source can be assigned directly to a specific eigenvalue. This is very similar when one would apply the QMC method to the estimation of disconnected contributions to the neutral pion correlator, and would involve at least a good approximation of the eigenbasis corresponding to at least a given number of smallest eigenvalues of the lattice Dirac operator. Certain techniques like low mode deflation, based on the exploitation of local coherence [41], or the approximate diagonality of the fermion propagator in momentum space, implying Landau gauge [42], and other methods, potentially useful in this context, exist. Further investigations in this direction are very interesting and promising, but they lie beyond the scope of this work and have to be postponed to future investigations.
Instead of this, we will explicitly demonstrate the QMC approach taking the example of the quantum mechanical harmonic oscillator on the lattice. Although this model is rather trivial and its optimal asymptotic error behaviour of $N^{-1}$ with the number of samples $N$ in the QMC approach is as expected (by construction of the QMC technique [16]), we get

a good insight into the basic steps involved in a QMC simulation. Moreover, the mastery of this simple model can be seen as a prelude to the solution of a more sophisticated, rather non-trivial model, namely the quantum mechanical *anharmonic* oscillator, which can be treated with QMC methods by means of techniques we developed for the harmonic oscillator.
We will introduce the lattice actions of the harmonic and anharmonic oscillator in section 4.2. In section 4.3 we construct an explicit algorithm for the generation of lattice paths for the harmonic oscillator suitable for the QMC approach. This is followed by section 4.4 where we present the results of the error scaling for the harmonic and anharmonic oscillator. We will compare for both models the asymptotic error behaviour of a standard Monte Carlo (MC) and a QMC technique and finally conclude this chapter in section 4.5, and give an outlook and perspectives to possible next steps for the integration of QMC methods into further lattice problems.
The two experiments we are going to investigate should be considered as a first exploratoration, aiming at the general goal to assess the applicability of the QMC method for the evaluation of path integrals describing quantum mechanical and quantum field theoretical systems in Euclidean space-time, regularised through the lattice approach. A first-time positive verification will be performed by the non-trivial example of the quantum mechanical anharmonic oscillator.
But before coming to this discussion, we want to extend a little bit the understanding of *how* the QMC method achieves the improved error behaviour, which is strongly connected to the uniformity property. In order to reach this, we want to illustrate in the following section what makes samples generated through a quasi-Monte Carlo technique so different from a naive sampling in two dimensions.

## 4.1. Quasi-Monte Carlo samples are "more uniform"

The special mathematical properties of quasi-Monte Carlo methods have been summarised in ref. [16], and are discussed in more detail in the mathematical literature, for example in the reviews [17] and [18]. However, at this point we rather want to skip a mathematical discussion of this topic, and want to come directly to a practical illustration of one of the most prominent properties of QMC samples often referred to as *uniformity* or *more uniform*[1].
A little experiment will bring us closer to the understanding of this property. Consider a unit square $[0,1] \times [0,1]$, which is subdivided into $8 \times 8$ small squares of equal size. Now, we throw 512 rice seeds (pseudo)randomly[2] into the large square and count for each of the $8 \times 8 = 64$ little squares the number of seeds they contain. One example of the outcome of such an experiment (using a PC) is shown in figure 4.1 on the left. The colour of each square corresponds to the number of rice seeds it contains. On the right of this

[1] This property is strongly related to the discrepancy property, a mathematical term with a well defined meaning in the context of QMC [16].
[2] Either one can do a real experiment on a checkerboard (as Karl Jansen suggested to me while we were drinking a coffee) with real rice seeds, or you use a pseudo random number generator on your PC.

figure we have plotted a histogram of the counts. We can see clearly that the distribution is rather broad. This means in practice that some squares contain significantly more or less seeds than one would expect on average, namely 8.

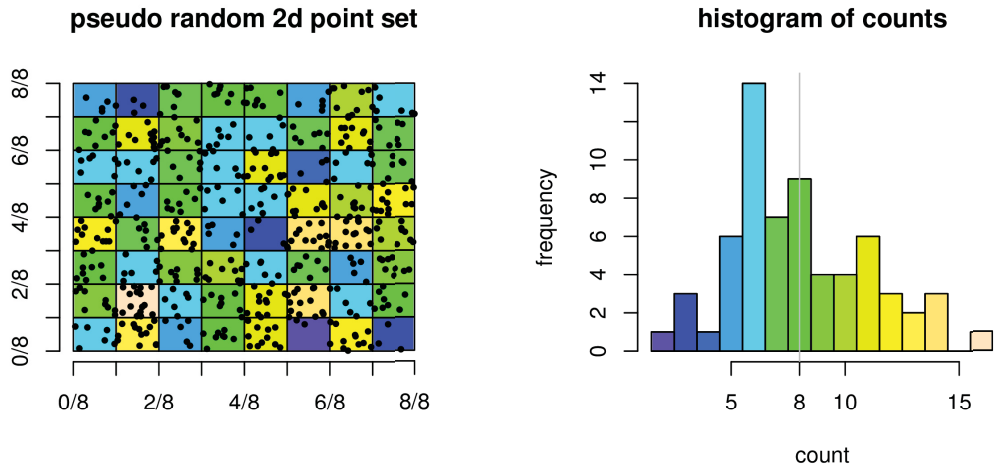


Figure 4.1.: **Left:** 512 rice seeds thrown (pseudo)randomly onto a square of edge length 1, subdivided into $8 \times 8$ equal smaller squares, each colour corresponds to the number of seeds contained in the square; **right:** histogram, showing the number of squares with a certain number of seeds, colour code corresponding to figure on the left

If we would use these points, $(x_i, y_i)_{i=1\ldots512}$, for a Monte Carlo approximation of a two-dimensional integral

$$\int_0^1 \int_0^1 f(x,y)dxdy \approx \frac{1}{512} \sum_{i=1}^{512} f(x_i, y_i) \tag{4.1}$$

it should become clear that regions of the function $f$ in squares with small or large counts are over- or underrespresented respectively in the final average. Furthermore, this uneven filling of squares with seeds leads to significant fluctuations when comparing the approximation to a different sampling with 512 seeds, where completely different squares will be over- or underrepresented. This uneven sampling is reflected in the Poisson distribution, shown in figure 4.2, which describes the probability of each count in the limit of infinitely many little squares[3] when the average count of 8 is kept fixed.

[3] A finite number of squares would be described by the binomial distribution. But for the case of 64 elements, we considered here, the binomial distribution almost coincides with the Poisson distribution.

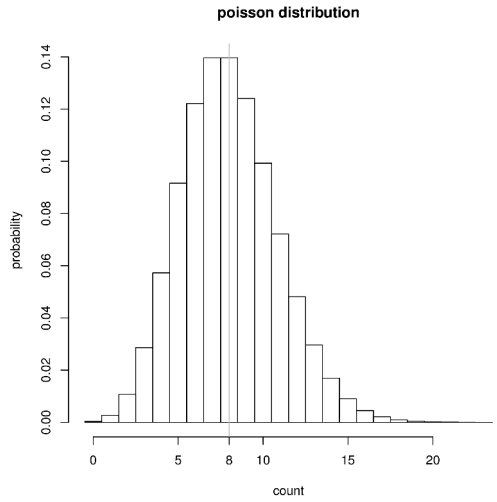


Figure 4.2.: Poisson distribution for the expectation value $\bar{n} = 8$

This little experiment should illustrate what happens in a conventional Monte Carlo simulation.

Now we want to repeat exactly the same experiment with a set of 512 QMC points. Here and in the following we use the Sobol' method [43] with direction numbers from Frances Kuo's page `http://web.maths.unsw.edu.au/~fkuo/sobol/index.html` for the generation of such point sets. For further reading, see the references [44], [45] and a three-pages-note on the top of this web page and ref. [16].

The result is shown in figure 4.3. As we can see, each little square contains exactly 8 points. This result demonstrates very convincingly that QMC points are distributed much more evenly over the area of the square. Hence, one expects much smaller fluctuations (= statistical errors) when using such points for the approximation (4.1) of an integral.

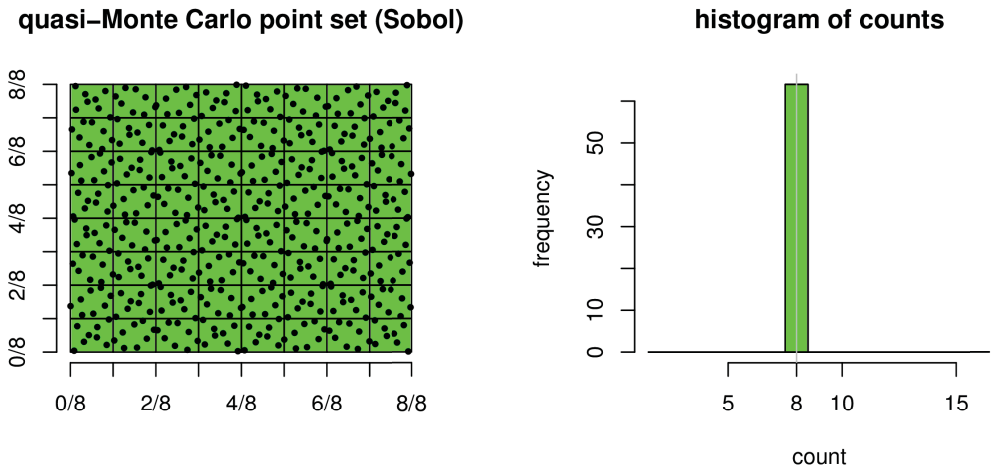


Figure 4.3.: The same experiment as shown in figure 4.1 but with (deterministic) quasi-Monte Carlo samples, for further explanation see description, figure 4.1

We have to admit that the number of squares used for the partioning of the unit square was not chosen completly arbitrary in this example. In fact, a partitioning based on powers of 2 and natural numbers for the average count of seeds per rectangle always leads to a delta-histogram as in the right plot of figure 4.3. This corresponds to a situation where each little square contains exactly the same amount of points. But the qualitative features we found remain even true if we would have chosen a less advantageous partitioning of $13 \times 13$ for example. The resulting histograms for a pseudo-random sampling and a Sobol' sampling, we would obtain for such a partition, are shown in figure 4.4.

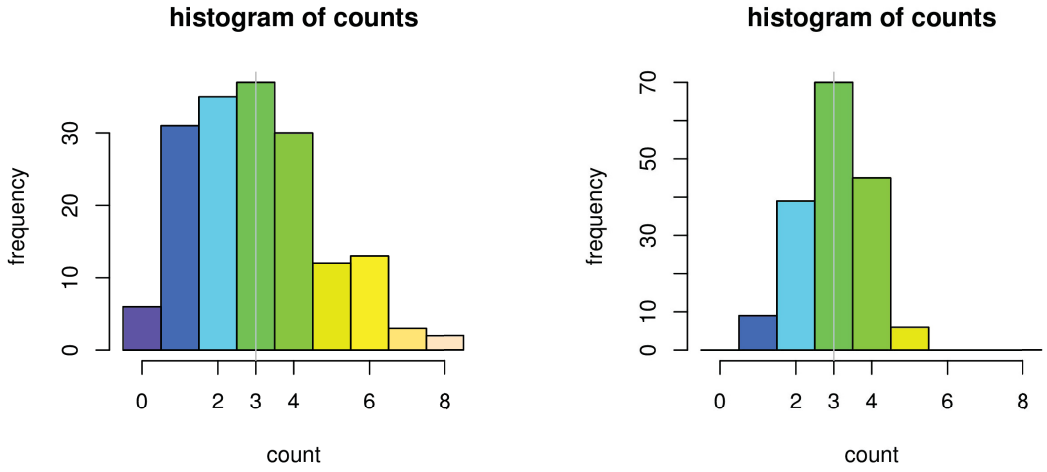


Figure 4.4.: Results of a similar experiment as shown in figures 4.1 and 4.3 but with a partitioning of $13 \times 13$ squares and 507 seeds in total, **left:** conventional pseudo-random sampling, **right:** QMC sampling, (take into acount the different scales on the y-axis in both plots, see also description of figure 4.1)

In the QMC case (right plot) the counts are not peaked at only one value, as it was the case for a $8 \times 8$ partitioning, but we can still observe a significant difference to the plot on the left, the pseudo-random result. We can see that the counts in the QMC case are much stronger focused around the expectation value of 3 in contrast to the pseudo-random sampling, where we have almost equal probabilities for the counts $1, 2, 3$ and 4.

For the reason of a good illustration we have performed this experiment in two dimensions. But the general observations could be reproduced also in much higher dimensions. This demonstration should suffice to make some of the advantageous properties of quasi-Monte Carlo sequences more clear. In the next section we want to discuss briefly the two physical models to which we want to apply the QMC approach.

## 4.2. The harmonic and anharmonic oscillator on the lattice

The path integral quantisation of the harmonic and anharmonic oscillator on the lattice has been discussed in detail by Creutz and Freedman [46]. Hence, we will repeat the basic steps very briefly in the following and refer the reader to this literature and to ref. [16] for further details.

In classical mechanics the Lagrangian of the anharmonic oscillator formulated in eu-

clidean space-time ($t \to it$) is

$$L(x,t) = \frac{M_0}{2}\left(\frac{dx(t)}{dt}\right)^2 + \frac{\mu^2}{2}x(t)^2 + \underbrace{\lambda x(t)^4}_{\text{quartic term}} \quad , \tag{4.2}$$

for a particle of mass $M_0$ passing along the path $x(t)$. $\mu^2$ is the spring constant of a *harmonic* oscillator. $\lambda$ is the coupling constant controlling the strength of the *anharmonic* or *quartic* term (last term in (4.2)). Hence, $\lambda > 0$ describes an anharmonic oscillator and $\lambda = 0$ a harmonic oscillator. The action $S$ for a system with a finite evolution time $T$ is just $S = \int_0^T L(x,t)dt$. For the construction of a partition function we need to imply the periodic boundary conditions $x(0) = x(T)$.

The next step is the discretisation of the path $x(t)$

$$x(t) \to x(t_i) \to x_i \tag{4.3}$$

on the finite time lattice

$$t_i = a(i-1) \quad i = 1 \dots d \, , \tag{4.4}$$

with $d$ equidistant time slices $t_i$ of separation $a$. Periodic boundary conditions can be achieved by defining $t_0 := t_d$ and $x_0 := x_d$. The time derivative $\dot{x}(t)$ is formulated on the lattice as

$$\dot{x}(t_i) \to \nabla x_i := \frac{1}{a}(x_{i+1} - x_i) \, . \tag{4.5}$$

Finally, we can formulate the lattice action:

$$S^{\text{latt}} = \sum_{i=0}^{d} a\left(\frac{M_0}{2}\frac{(x_{i+1} - xi)^2}{a^2} + \frac{\mu^2}{2}x_i^2 + \lambda x_i^4\right) \, . \tag{4.6}$$

In the following we will drop the index "latt" on the lattice action, as this is the only action we will consider. For later applications we want to rewrite the quadratic part[4] of the action (4.6) in terms of a bi-linear form in the vector $\mathbf{x} = (x_1, \dots, x_d)^t$:

$$S(\mathbf{x}) = \frac{1}{2}\mathbf{x}^t C^{-1}\mathbf{x} + \sum_{i=1}^{d} a\lambda x_i^4 \, , \tag{4.7a}$$

$$\text{with} \quad (C^{-1})_{i,j} = \frac{2M_0}{a}\left(u\delta_{i,j} - \frac{1}{2}(\delta_{i,j+1} + \delta_{i+1,j})\right) \, , \tag{4.7b}$$

$$\text{and} \quad u = 1 + \frac{a^2\mu^2}{2M_0}. \tag{4.7c}$$

We will see in section 4.3 why we defined the inverse of $C$ instead of $C$ itself. The quantisation is now performed through the lattice path integral which can be conveniently

[4] These are all terms excluding the quartic terms $x_i^4$.

expressed as the partition function

$$Z = \int e^{-S(\mathbf{x})} dx_1 \dots dx_d \ , \tag{4.8}$$

where the integral extends over the whole d-dimensional real space $\mathbb{R}^d$. An observable $\mathcal{O}(\hat{x})$, defined as a function of the position operator $\hat{x}$ in the quantised theory, can be measured by the insertion of suitable functions $O(\mathbf{x})$ into the partition function (4.8) :

$$\langle \mathcal{O}(\hat{x}) \rangle = Z^{-1} \int_{\mathbb{R}^d} O(\mathbf{x}) e^{-S(\mathbf{x})} dx_1 ... dx_d \ , \tag{4.9}$$

and normalising to $Z$. We will discuss in the next subsection how the functions $O(\mathbf{x})$ can be constructed.

### 4.2.1. Observables

The most interesting observables of the aforementioned models are the energies of the ground and first excited state. Those however, have to be constructed from primary observables such as

$$X^2 = \frac{1}{d} \sum_{i=1}^{d} x_i^2 \ , \tag{4.10}$$

$$X^4 = \frac{1}{d} \sum_{i=1}^{d} x_i^4 \quad \text{and} \tag{4.11}$$

$$\Gamma(\tau) = \frac{1}{d} \sum_{i=1}^{d} x_i x_{i+\frac{\tau}{a}} \ , \tag{4.12}$$

which are observable functions corresponding to the quantum mechanical operators $\hat{x}^2$, $\hat{x}^4$ and $\hat{x}(t+\tau)\hat{x}(t)$ respectively. The ground state energy $E_0$ can then be measured through

$$E_0 = \mu^2 \langle X^2 \rangle + 3\lambda \langle X^4 \rangle + \frac{\mu^4}{16} \ , \tag{4.13}$$

whereas the energy gap $\Delta E = E_1 - E_0$ to the first excited state with energy $E_1$ has to be extracted from the asymptotic behaviour of the correlator $\Gamma(\tau)$ (4.12),

$$\Gamma(\tau) \sim C_0 \frac{1}{2} \left( e^{-\Delta E \tau} + e^{-\Delta E (T-\tau)} \right) \ , \tag{4.14}$$

using exactly the same procedure as in the analysis of the pseudoscalar correlators in the previous chapters (see chapter 2, section 2.3).

In the next section we want to discuss the method for the generation of lattice paths for the harmonic oscillator.

## 4.3. Gaussian sampling in the QMC approach

When considering the harmonic oscillator one can see that the partition function (4.8) is a multidimensional Gaussian integral which can be explicitly written as

$$Z = \int e^{-\frac{1}{2}\mathbf{x}^t C^{-1}\mathbf{x}} dx_1 \dots dx_d \; . \tag{4.15}$$

This partition function then describes a multivariate normal distribution $\mathcal{N}(0, C)$ in the variables $x_i$, $C$ being the correlation matrix[5] of these variables, define through its inverse in (4.7b). (This implies $\langle x_i x_j \rangle = C_{i,j}$.) If $M_0$, $a$ and $\mu^2$ are strictly positive, $C$ is a symmetric positive definite matrix with the eigenvalues:

$$\lambda_i = \left( \frac{2M_0}{a} \left( u - cos(2\pi i/d) \right) \right)^{-1} \; , \tag{4.16}$$

which can be obtained from the discrete Hartley transform of $C^{-1}$. This transformation is defined through the matrix $G = Re(F) + Im(F)$, where $F_{k,l} = \frac{1}{\sqrt{d}} \exp(-2\pi i k l/d)$ is the discrete Fourier transformation matrix. Then, $GC^{-1}G^t$ yields a diagonal matrix with the inverse of the eigenvalues (4.16) on the diagonal. Corresponding to this, the partition function (4.15) can be transformed into a product of $d$ one-dimensional Gaussian integrals through the orthonormal transformation $\mathbf{w} = G\mathbf{x}$ :

$$Z = \int e^{-\frac{w_1^2}{2\lambda_1}} dw_1 \dots \int e^{-\frac{w_d^2}{2\lambda_d}} dw_d \; . \tag{4.17}$$

At this point it should be straightforward to follow the algorithm for the generation of lattice paths for the harmonic oscillator, which we will discuss now.

### 4.3.1. Generation algorithm for lattice paths

1. The starting point for the generation of a lattice path is always a point $\tilde{\mathbf{z}} = (\tilde{z}_1, \dots, \tilde{z}_d)^t$ generated uniformly in the hypercube $[0,1]^d$ by a quasi-Monte Carlo or conventional Monte Carlo method. We will discuss in the next section in more detail which methods we have used for the generation of $\tilde{\mathbf{z}}$.

2. The next step is the calculation of $\tilde{\mathbf{w}}$ distributed according to the separable measure of the partition function (4.17). This is realised by the transformation of $\tilde{\mathbf{z}}$ with the inverse of the standard normal cumulative distribution function $\Phi(y) = \frac{1}{\sqrt{2\pi}} \int_{-\infty}^{y} e^{-\frac{x^2}{2}}$ and multiplication with the standard deviation[6] $\sigma_i = \sqrt{\lambda_i}$ of $w_i$:

$$\tilde{w}_i = \sqrt{\lambda_i} \Phi^{-1}(\tilde{z}_{\pi^{-1}(i)}) \; , \quad \forall i = 1 \dots d \; . \tag{4.18}$$

[5] Here we see the reason for the way we defined the matrix $C$ in (4.7b), namely that the correlation matrix enters through its inverse into the multivariate gaussian distribution $p(\mathbf{x}) \sim \exp\left(-\frac{1}{2}\mathbf{x}^t C^{-1}\mathbf{x}\right)$.

[6] The standard deviation $\sigma_i$ of each $w_i$ can be read off from the denominator in the exponential terms in (4.17).

As depicted by $\pi^{-1}(.)$, the components of $\tilde{\mathbf{z}}$ have to be reordered such that $\tilde{z}_1$ comes upon the largest eigenvalue, $\tilde{z}_2$ comes upon the second largest eigenvalue and so on until the last component $\tilde{z}_d$ meets the smallest eigenvalue in (4.18). This is achieved by finding a permutation $\pi(.)$ which brings the eigenvalues in decreasing order such that $\lambda_{\pi(1)} > \ldots > \lambda_{\pi(d)}$. $\pi^{-1}(.)$ is then just the inverse permutation, fulfilling $\pi^{-1}(\pi(i)) = i \ , \ \forall i = 1 \ldots d$.

3. Finally the lattice path $\tilde{\mathbf{x}}$, as described by the original partition function (4.15) of the harmonic oscillator, is obtained through the Hartley transform[7] of $\tilde{\mathbf{w}}$:

$$\tilde{\mathbf{x}} = G\tilde{\mathbf{w}} \ . \tag{4.19}$$

This algorithm forms the basis of all the numerical investigations which we discuss in the next section. But as we have seen, the considerations we have undertaken would also apply to any other problem that can be formulated as a multidimensional integral with a multivariate Gaussian measure, such as the stochastic estimation of the fermion propagator in lattice-QCD for example. The only special feature we exploited here was that the matrix $C^{-1}$ (as well as $C$) is a Toeplitz matrix[8] and that this matrix can be diagonalised trivially through the discrete Hartley (discrete Fourier) transform. In more general cases, including also the fermion propagator estimation in lattice-QCD, one needs to determine the eigenvalues and eigenvectors with costlier methods or methods that only lead to approximate diagonalisations. But if such methods turn out to be efficient enough one could also apply the QMC approach to such generalised models.
But for the moment we want to come back to to the harmonic and anharmonic oscillator and the numerical results we obtain when we apply the aforementioned algorithm.

## 4.4. Numerical results

In this section we want to compare conventional Monte Carlo and quasi-Monte Carlo methods at the example of the harmonic and anharmonic oscillator.
For both models, the Mersenne Twister pseudo random number generator [47], as a representative for conventional Monte Carlo, has been chosen for the generation of uniform samples in the unit cube $[0,1]^d$. Sobol' sequences [43] are being used as quasi-Monte Carlo technique, also described in ref. [16], using the approach by F. Y. Kuo and S. Joe [44] [45] for the selection of direction numbers. We obtained these direction numbers from the web site `http://web.maths.unsw.edu.au/~fkuo/sobol/index.html` by F. Kuo.
As a first test of the superiority of the QMC approach we want to investigate the harmonic oscillator.

[7] As the Hartley transform is symmetric and orthonormal it holds that $G = G^t = G^{-1}$, meaning that $G$ is self-inverse.

[8] A Toeplitz matrix $T_{i,j}$ is a matrix whose entries $t_{i,j}$ only depend the difference $i - j$ of the indices. Hence, the main diagonal and all sub-diagonals each contain the same value.

### 4.4.1. Harmonic oscillator

Although rather trivial but still a real physical problem, the harmonic oscillator turns out to be a perfect test ground for the quasi-Monte Carlo approach in comparison with conventional Monte Carlo techniques. This comes generally from the fact, that we can directly sample paths according to the Boltzmann weight $e^{-S}$, which is basically the density of a multivariate normal distribution. Hence, we can apply directly all considerations we made in the previous section and especially the algorithm we established there. The only peculiar point in this algorithm is the first step, where we either use the Monte Carlo or the quasi-Monte Carlo approach to chose the point $\tilde{\mathbf{z}}$. The following parameters have been chosen for this first test:

$$M_0 = 0.5 \; ; \; a = 0.5 \; ; \; \mu^2 = 2.0 \; ; \; d = 100 \; (; \; \lambda = 0) \; . \tag{4.20}$$

To investigate the asymptotic error behaviour of the QMC aproach we performed simulations with a given number of samples, namely $N = 2^7,\ 2^{10},\ 2^{13},\ 2^{16}$ and $2^{19}$. We chose powers of 2 for the number of samples due to the special properties of the QMC sequences (see [16]). Then for each number of samples $N$ we perform 300 simulations to determine the error and the error of the error of a single simulation with such an $N$. This procedure is repeated in exactly the same way for conventional Monte Carlo samples. In the QMC case we have used a scrambling technique (see [16], section 5) in each of the 300 repetitions to generate a new set of $N$ samples. The result from both methods for the error of the observable $X^2$ in dependence of $N$ is plotted in figure 4.5.

As both axes in this plot are logarithmic, the asymptotic behaviour can be distinguished through the slope of a line passing through all the points. As an aid, we have plotted the solid lines, describing $CN^{-1}$ error behaviours with different constants $C$ (as we expect for QMC), and the dashed lines describing a $N^{-\frac{1}{2}}$ error behaviour, expected for MC simulations. In fact, we can observe that the triangle symbols (QMC) are parallel to the solid lines, whereas the circle symbols (MC) follow quite closely a dashed line. An explicit fit of the errors verifies our observation we made by eye. A fit of the points of figure 4.5 to $\sim N^{\alpha}$ gives an exponent of $\alpha = -0.485(10)$ for the Monte Carlo errors and $\alpha = -1.008(15)$ for the QMC errors. Similar results are obtained for the other observables, $X^4$ and $E_0$. The strongly improved error scaling is the explanation for the fact, that a single simulation with $N = 2^{10} = 1024$ QMC samples gives already the same precision that one would achieve with an ordinary Monte Carlo simulation with $N = 2^{19} = 524288 = 512 \times 1024$ samples. This result demonstrates impressively what the quasi-Monte Carlo approach can achieve under optimal conditions, namely a drastic reduction of the required number of samples sufficient to achieve a given accuracy. Although this problem is rather trivial and analytic solutions for it exist already, making the treatment by Monte Carlo methods completely redundant, we can still say that quasi-Monte Carlo *can* be applied to physical problems in lattice systems. A rather non-trivial problem, for which *no* analytic solutions in closed form exist, is the anharmonic oscillator. We will see now how efficient the QMC approach will be there.

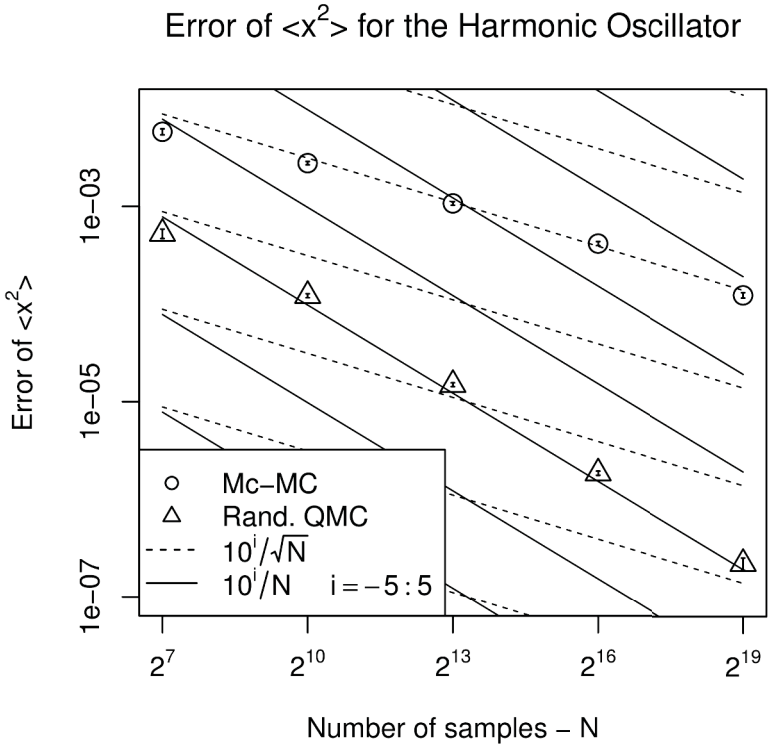


Figure 4.5.: Comparison of the asymptotic error scaling of $\langle X^2 \rangle$ for the QMC and MC aproach at the example of the harmonic oscillator, see text for further description

### 4.4.2. Anharmonic oscillator

In the case of the anharmonic oscillator the quartic coupling constant is set to $\lambda = 1.0$. This brings us to a fundamental problem when we want to construct lattice paths that are distributed according to the Boltzmann weight $e^{-S}$, which is *not* a Gaussian measure anymore, due to the quartic terms $x_i^4$ in the action. In general, one would need to find more sophisticated approaches to map from the space of variables $x_i$ to the $d$-dimensional unit cube, as we did it in the case of the harmonic oscillator, where no correlation among the variables is present anymore. Such advanced methods are under investigation at the moment, but no definite conclusions about their efficiency can be drawn now, but a more simple approach exists, which is used quite commonly in the lattice community, and is often referred to as the reweighting technique. To the knowledge of the author, this method was first mentioned and used in [48], but is also explained in [49], chapter 8, at the example of the fermion determinant in lattice-QCD. This approach allows us to use exactly the same sampling algorithm as for the harmonic oscillator by only changing the observables. The basic idea can be outlined again through the anharmonic oscillator's

partition function:

$$Z = \int e^{-S(\mathbf{x})}\, dx_1 \ \ldots \ dx_d \ . \tag{4.21}$$

The insertion of $1 = \exp(-S'(\mathbf{x}))\exp(+S'(\mathbf{x}))$, which is the ratio of a Boltzmann factor with a different action $S'$, yields:

$$Z = \int e^{-S(\mathbf{x})+S'(\mathbf{x})}\, e^{-S'(\mathbf{x})}\, dx_1 \ldots dx_d \ . \tag{4.22}$$

Now the second exponential is interpreted as the probability distribution of the variables $x_i$, and the first exponential is considered as an insertion into the partition function and will be treated as a weighting cofactor

$$W(\mathbf{x}) = e^{-S(\mathbf{x})+S'(\mathbf{x})} \tag{4.23}$$

for observables that one aims to determine. Hence, the expression for some observable $\mathcal{O}$ of the anharmonic oscillator, including the previous considerations, can be written as

$$\langle \mathcal{O} \rangle = \frac{\int O(\mathbf{x})\, W(\mathbf{x})\, e^{-S'(\mathbf{x})}\, dx_1 \ldots dx_d}{\int W(\mathbf{x})\, e^{-S'(\mathbf{x})}\, dx_1 \ldots dx_d} \ . \tag{4.24}$$

In general the action $S'$ could be chosen freely. But it should fulfil two criteria. First, it should be simple to generate samples corresponding to the Boltzmann weight $e^{-S'}$. And second, $S'$ should be as similar as possible to the original action $S$, such that the weight factor (4.24) fluctuates as few as possible. An obvious possibility one could try in place of $S'$ is the action of a harmonic oscillator, but with a different set of parameters: $M_0'$, $(\mu')^2$ and $a'$. $S'$ is then again a bi-linear form in $\mathbf{x}$:

$$S' = \frac{1}{2}\mathbf{x}^t (C')^{-1}\mathbf{x} \ , \tag{4.25}$$

with $C'^{-1}$ defined in exactly the same way as $C^{-1}$ in (4.7b) but with $\mu^2$ replaced by $(\mu')^2$. To keep it as simple as possible and to reduce the tuning effort we left $M_0$ and $a$ unchanged at this stage.

This brings us to the strategy we used to treat the anharmonic oscillator.

First, $N$ *harmonic* oscillator paths $(\mathbf{x}_i)_{i=1\ldots N}$ are generated, as described in section 4.3, but with the parameters $M_0$, $a$ and $(\mu')^2$ (corresponding to the action $S'$). Then, along with the observables $X^2$ , $X^4$ and $\Gamma(\tau)$ for each $\mathbf{x}_i$, also the weight factors $W(\mathbf{x}_i)$ are determined. The approximation of any observable $\mathcal{O}$ of the *anharmonic* oscillator is then calculated through the weighted average

$$\langle \mathcal{O} \rangle \approx \frac{\sum_i O(\mathbf{x}_i) W(\mathbf{x}_i)}{\sum_i W(\mathbf{x}_i)} \quad \text{(cf. (4.24))}. \tag{4.26}$$

In this way one can avoid the non-Gaussian action in the sampling procedure and postpones it completely to the weight factor $W$. The delicate point of the reweighting technique is basically the question how strong the fluctuations of $W$ are in practice, and

if the approximation (4.26) actually converges for larger and larger number of samples $N$. But as we will see in the results below, this procedure can in fact be used to calculate precise determinations of the ground and first excited state energy of the anharmonic oscillator. We set up our experiment with the following parameters:

$$M_0 = \frac{1}{2} \tag{4.27}$$

$$a = \begin{cases} 0.015 & \text{for} \quad d = 100 \\ 0.0015 & \text{for} \quad d = 1000 \end{cases} \tag{4.28}$$

$$\mu^2 = -16 \tag{4.29}$$

$$\lambda = 1 \; . \tag{4.30}$$

As indicated, two different numbers of dimensions (time slices) have been used to investigate the error scaling behaviour towards the continuum limit. $a$ and $d$ were chosen correspondingly such that the physical situation ($T = 1.5$) was kept fixed. The least fluctuations of the weight factor were found for $\mu' = 0.176$ when simulating with $d = 100$ and $\mu' = 0.2$ for $d = 1000$. In a first investigation [16] we have determined the observ-

| $d$ | $O$ | $\alpha$ | $\log C$ | $\chi^2$/dof |
|---|---|---|---|---|
| $d = 100$ | $X^2$ | -0.763(8) | 2.0(1) | 7.9 / 6 |
| | $X^4$ | -0.758(8) | 4.0(1) | 13.2 / 6 |
| | $E_0$ | -0.737(9) | 4.0(1) | 8.3 / 6 |
| 1000 | $X^2$ | -0.758(14) | 2.0(2) | 5.0 / 4 |
| | $X^4$ | -0.755(14) | 4.0(2) | 5.7 / 4 |
| | $E_0$ | -0.737(13) | 4.0(2) | 4.0 / 4 |

Table 4.1.: Results for the error scaling of the observalbes $X^2$, $X^4$ and $E_0$ for the model of the anharmonic oscillator, simulated through reweighting, observable errors fitted to the model $\sim CN^\alpha$.

ables $X^2$,$X^4$ and $E_0$ and their errors using the same procedure as for the harmonic oscillator. The results are shown in table 4.1. Similarly to the harmonic oscillator, we have fitted the errors of each observable to the model $\sim CN^\alpha$ (a constant $C$ times the number of samples $N$ to the power of $\alpha$), as shown exemplarily for $X^2$ and $E_0$ with $d = 1000$ in figure 4.6. We find very consistent results throughout all observables for both experiments: $d = 100$ and $d = 1000$. The error seems to scale with a power of $N$ of approximately $\alpha = -\frac{3}{4}$. This is exactly in the middle between the Monte Carlo expectation of $\alpha = -\frac{1}{2}$ and the QMC result under optimal conditions, namely $\alpha = -1$. So we can assess that, QMC significantly improves the error behaviour also in the case of the *anharmonic* oscillator using the reweighting approach.

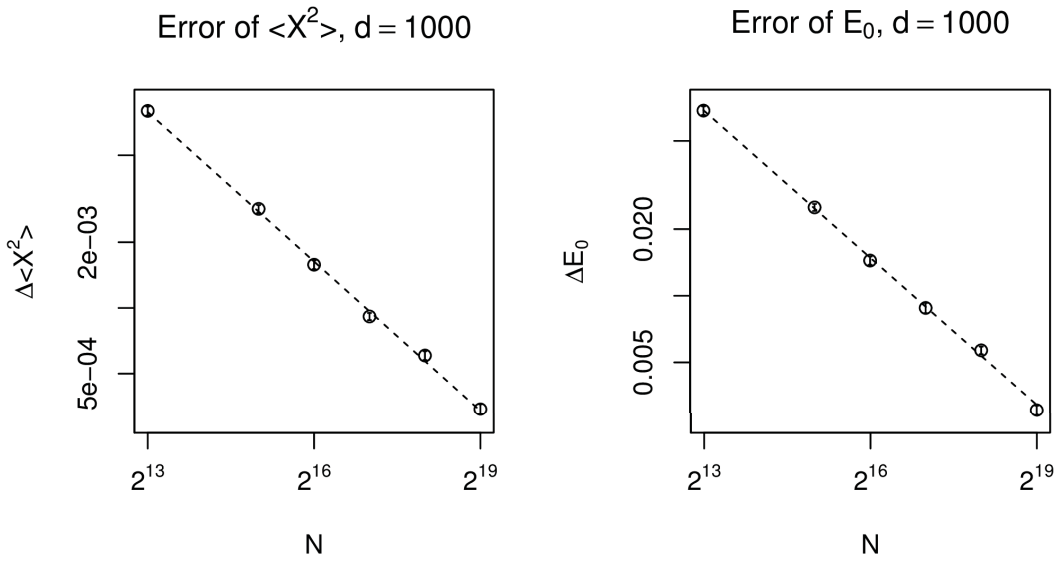


Figure 4.6.: The error of the observables $X^2$ (left) and $E_0$ (right) as a function of $N$, the number of samples, for the anharmonic oscillator. The dashed line (double-log plot) represents a fit describing the errors with the model $CN^{\alpha}$. Detailed results are listed in table 4.1.

### Energy gap

In a further investigation [50], we also found an improved error scaling for the energy gap $\Delta E = E_1 - E_0$, measured through the correlation function (4.12) (see section 4.2.1). The result of $\alpha = -0.738(13)$ [50], obtained with $N = 2^5, 2^8, 2^{11}, 2^{14}$, is in complete agreement with the results in table 4.1. Whereby we have to note that the parameter $\mu^2 = -16$ in our original setup had to be changed to $\mu^2 = -4$ due to the fact that the energy gap is too small to be measurable through the correlator $\Gamma(\tau)$ in the former case[9].

Coming back to the discussion about all results, we find, that our results for the ground state energy $E_0 = 3.857(4)$ ($d = 100$) and $E_0 = 3.862(4)$ ($d = 1000$) compare very well to the continuum ($T \to \infty$, $a \to 0$) result $E_0 = 3.863$, computed in [51] through an iterative algorithm, and encourages us to assume that we are already very close to the continuum limit. Nevertheless, we also considered different values of $T$, ranging from 0.2 to 5.0, to investigate the applicability of the reweighting technique to a wider range of physical situations. These investigations indicate, that our present approach for the determination of observables of the anharmonic oscillator is rather sensitive to $T$. We

[9] From $\mu^2 = -16$ to $\mu^2 = -4$ the energy gap changes from 0.0015 to 1.576. If one wants to measure $\Delta E$ from $\Gamma(\tau) \sim e^{-\Delta E \tau}$, one needs at least a $T \approx \frac{1}{\Delta E}$ such that $\Gamma(\tau)$ decays at least to $\sim e^{-1}$. For $\Delta E = 0.0015$ $T$ would need to be $\approx 700$, which is unfeasible to simulate with our present setup!

found very good error convergence rates of $\alpha \approx -1$ for $T \leq 0.2$ and rather bad results of $\alpha \approx -\frac{1}{2}$ for $T > 5$. A better understanding of these observations might also be the key to the understanding of this "in-between-behaviour" $\alpha = -\frac{3}{4}$ that is observed at $T = 1.5$. Such investigations are left to future works.
Another interesting point is the choice of the action $S'$. As mentioned above, we have only varied the parameter $\mu'$ of the action $S'$, used for the generation of the "harmonic" samples $\mathbf{x}_i$. First investigations give strong indications that one can achieve even further improvements, if one also seeks in the space of all three parameters, $M_0'$, $a'$ and $\mu'$. In a more general approach one could give even more freedom to the choice of $C'$ by altering directly the eigenvalues of $C'$ with the only requirement that they should be strictly positive. We imagine improvements in this direction, but have to leave it to future investigations to check whether such techniques do in fact lead to a further improvements of the error scaling.
With these final remarks we want to come to the conclusions and the next steps of this project.

## 4.5. Outlook and conclusions

In this chapter we have demonstrated the successful application of QMC methods to quantum mechanical lattice problems, namely the harmonic and anharmonic oscillator. We have verified a perfect error scaling of $O(N^{-1})$ in the case of the harmonic oscillator. Although the outcome of this experiment was as expected, it can be seen as a first application of QMC to a real physical problem in a lattice system. We then passed on to the anharmonic oscillator to investigate the performance of QMC in a more elaborate non-trivial problem. Also in this case we found a significantly improved error scaling of $O(N^{-\frac{3}{4}})$, as compared to $O(N^{-\frac{1}{2}})$ one achieves with conventional Monte Carlo methods. This error scaling behaviour holds for all observables, including the energy gap $\Delta E$, which can be considered as a rather non-trivial observable, as it is obtained from a non-linear regression of the correlator $\Gamma(\tau)$.
These first, very successful investigations encourage us to continue our work in the direction of QMC applications in lattice field theory. Corresponding to the discussion in this chapter, the next steps could head to basically three different directions.
First of all, one could directly continue investigations of further improvements in the sampling procedure of the anharmonic oscillator. As indicated previously, we know already from first test that the tuning of the quadratic action (4.25), respectively the matrix $C'$, can lead to a reduction of the weight fluctuations, and hence, to smaller errors of the average (4.24). Future investigations could check explicitly whether it is achievable to apply the QMC method in this way even more efficiently to the anharmonic oscillator, leading possibly to an even better asymptotic error scaling or making it possible to achieve similar good convergence rates (of $O(N^{-\frac{3}{4}})$) over a wider range of time extents $T$. It would then be also most interesting to understand theoretically the quantitative values of the error scaling exponent.
Initially, we have entered the discussion about QMC through the problem of stochastic

estimations of disconnected diagrams for the neutral pion correlation function (1.32) in subsection 1.2.3, chapter 1. Many other interesting observables in QCD, like the correlation functions of the $\eta$ and $\eta'$ meson, the strange content of the nucleon and other flavour singlet quantities, also involve disconnected diagrams, and hence, would also benefit from improvements. In order to apply the QMC approach for this kind of problem, more work is needed towards investigations of approximate diagonalisations of the lattice Dirac operator (respectively the fermion propagator). Only if one can achieve a sufficiently good diagonalisation one has access to the essential degrees of freedom of a matrix, namely its eigenvalues and eigenvectors. This is crucial, in the opinion of the author, for the successful setup of QMC based stochastic methods for the evaluation of disconnected diagrams. Dedicated analyses also have to show how one can judge what *can be* considered as a sufficiently good diagonalisation, and which leads in fact to smaller errors than conventional stochastic approximation techniques. Nevertheless, potentially suitable techniques exist already. Possible, promising candidates are the approximate diagonalisation of the Fourier transformed lattice Dirac operator through gauge fixing to Landau gauge [42] and inexact deflation methods using the feature of local coherence [41].

The third direction, comprising the largest potential for the saving of computational expenditures, goes directly towards the application of QMC to simulations of lattice field theories. This can be seen as the next logical step after applications in quantum mechanics. An application of QMC methods to, for example the Schwinger model without dynamical fermions, seems to be in reach. But before doing this, we will stay in quantum mechanics for one further step, and want to consider a one-dimensional spin model or equivalently a quantum mechanical rotator, given by the action

$$S = \frac{I}{a} \sum_{i=1}^{d} \left(1 - \cos(\phi_{i+1} - \phi_i)\right) \ , \tag{4.31}$$

where $I$ is the moment of inertia and $a$ the lattice spacing. The ratio $I/a$ could be interpreted as the coupling strength of the spins, which is effectively the only free parameter of this model apart from $d$. We imply periodic boundary conditions for the angular variables $\phi_i$: $\phi_0 = \phi_d$. In contrast to the oscillator models, we discussed in the previous sections, this model exhibits *topological* features. This can be seen through the non-vanishing of the topological charge:

$$Q^{top} = \frac{1}{2\pi} \sum_{i=1}^{d} (\phi_{i+1} - \phi_i) \bmod 2\pi \tag{4.32}$$

in an actual lattice simulation. The "mod $2\pi$" operation shifts any differences $\phi_{i+1} - \phi_i$ to the half open interval $(-\pi, \pi]$ by adding or subtracting suitable multiples of $2\pi$. This model with slightly different lattice discretisations was also discussed in more detail in [52]. We think the investigation of this model with respect to the treatment by QMC methods is a sensible intermediate step prior to the Schwinger model.

Conclusively, we can say that these first investigations give rise to an optimistic attitude

concerning the possibilities of applying the quasi-Monte Carlo approach in lattice field theory. But one really has to await the outcome of further investigations in the future before reliable conclusions can be drawn.
With this chapter we have discussed the last of the three major topics of this work. In a final conclusion we want to summarise the quintessences of *all* chapters the reader should take along.

# Conclusions

This work investigated a spectrum of quite different topics ranging from non-perturbative studies of pseudoscalar meson masses and decay constants up to conceptually innovative simulation techniques for lattice systems.
The purpose of chapter 1, "Theoretical basis", was the introduction to the topic of lattice-QCD simulations with twisted mass fermions. We presented our approach for the non-perturbative determination of pseudoscalar meson masses and decay constants. This is one of the first approaches to simulate *four* dynamical quark flavours, the up/down, strange and charm quark, in the sea.
In connection with the discussion of the neutral pion correlation function, which is difficult to determine due to disconnected contributions, we suggested a new approach, based on the quasi-Monte Carlo method, having the potential to a dramatic reduction of the number of samples necessary to achieve a given error criterion.
In chapter 2 we discussed in detail the determination of $f_\pi$ and $m_\pi$ on the lattice, and then used these values in combination with the chirally extrapolated values of $r_0$ to perform chiral fits with formulae from Wilson twisted mass $\chi$PT. This $\chi$PT description was used to perform the continuum limit and the extrapolation to the physical point at which we could set the scale of our lattice simulations. The main result (2.19) can be found at the end of this chapter on page 42. In conjunction with the determination of the lattice spacings

$$\begin{aligned} a(\beta = 1.90) &= 0.0899\ (10)_{stat.}\ (8)_{sys.}\text{fm} \\ a(\beta = 1.95) &= 0.0812\ (9)_{stat.}\ (6)_{sys.}\text{fm} \\ a(\beta = 2.10) &= 0.0624\ (6)_{stat.}\ (4)_{sys.}\text{fm}\ , \end{aligned}$$

involving statistical ("stat.") and systematic ("sys.") errors, we also investigated the applicability range of the next-to-leading order $\chi$PT description to the extent our data allowed such a study. We find very good agreement with the results obtained in [3] and [21], namely that the description is reasonable up to about five times the physical light quark mass, or equivalently pion masses upt to 300 MeV. The agreement of our determined low energy constants with these references (for $f_0$, $l_3$, $l_4$ and $M_\pm^{\text{phys}}$) and reference [24] (for $c_2$) completes the picture of a consistent description.
We then used these results for the determination of the decay constant of the $D_s$-meson in chapter 3. We discussed briefly the developments on the experimental and theoretical side in the past years and concluded, that the tension in the determination of $f_{D_s}$ between both sides newly increased in 2012 since 2010 from 1.6 to $2.2\sigma$. Based on our present approach, we investigated the influence of a strange *and* a charm quark, present in the sea quark action, on $f_{D_s}$. This is in contrast to most other determinations, which only

included the light quarks ($N_f = 2$) or additionally a strange quark ($N_f = 2 + 1$). The main result

$$f_{D_s} = 248.9(5.3)_{\text{comb.}}\ \text{MeV}\ , \tag{3.6}$$

with systematic and statistical uncertainties, added in quadrature to the combined error ("comb."), is shown in comparison with other lattice determinations and the PDG average in figure 3.7 on page 62. We find a rather small upward shift compared to the previous lattice determinations [4] [5], perfect agreement with another preliminary $N_f = 2+1+1$ prediction [40] and a deviation of approximatly $2\sigma$ from the experimental average [6]. Future investigations should aim to decrease the uncertainties of $f_{D_s}$. Only then one will be able to judge whether a discrepancy between theory and experiment remains, which could then be explained, as one possibility, by the neglecting of electromagnetic effects in the lattice setup, and furthermore, to which degree the number of dynamical quark flavours play a significant role.

In the last chapter we came back to the applications of the quasi-Monte Carlo (QMC) approach, and studied this method at the example of the harmonic and anharmonic oscillator, as these models are quite straightforward to simulate, and exact results exist in the literature, which could be used to compare with. We verified the perfect error scaling of $O(N^{-1})$ with the number of samples $N$, as seen in figure 4.5 on page 78, for the harmonic oscillator when applying the QMC method. For the anharmonic oscillator we could still achieve an improved error scaling of $O(N^{-\frac{3}{4}})$ in the QMC approach, as compared to $O(N^{-\frac{1}{2}})$ when using a conventional Monte Carlo method. Our final results for the anharmonic oscillator are listed in table 4.1 on page 80 and subsection 4.4.2, page 81. Further promising directions have been given that could possibly lead eventually to an application of QMC in lattice-QCD simulations, and already now we see realistic chances that this method could lead to improvements in the estimation of fermionic observables involving disconnected contributions, such as flavour singlet quantities or the quark contents of the nucleon.

Finally, we think that very interesting results have been obtained within this work. We have continued investigations that commenced long ago in the past. We looked at present into new approaches, opening, maybe, completely new possibilities for lattice simulations and we revealed several new directions worth to be investigated in the future.

# Danksagung

Ich möchte mich an dieser Stelle bei denen bedanken die das Zustandekommen dieser Arbeit maßgeblich unterstützt oder überhaupt erst ermöglicht haben.
Karl Jansen möchte ich besonders danken, für seine geduldige und vertrauensvolle Betreuung während meiner Zeit als Doktorand und beim Schreiben dieser Arbeit. Seine Ideen und Anregungen haben meine tägliche Arbeit bereichert und wesentlich zum gelingen dieser Arbeit beigetragen.
Ich möchte auch Michael Müller-Preußker für seine vielseitig Unterstützung und die herzliche Aufnahme in seine Arbeitsgruppe danken, was diese Arbeit ja überhaupt erst ermöglicht hat.
Ich danke der DFG, insbesondere dem SFB/TR9, für die finanzielle Unterstützung und die Ermöglichung der Teilnahme an unterschiedlichen Konferenzen und Dienstresien.
Ebenso danke ich dem Graduiertenkolleg “Masse Spektrum Symmetrie” (GK 1504) für die Veranstaltung der sehr informativen Blockkurse, der Unterstützung bei Dienstreisen und Teilnahme an Konferenzen.
Ein wesentlicher Teil dieser Arbeit ist im Rahmen der European Twisted Mass Collaboration entstanden. So soll auch ein wesentlicher Teil meines Dankes allen Mitgliedern der ETMC gelten. Sicher haben alle durch ihre spezielle Arbeit zum Erfolg des $N_f = 2+1+1$-Programms, und aller nötigen Vorarbeiten, beigetragen.
Die im Zusammenhang mit dieser Arbeit untersuchten Messergebnisse konnten nur mit einem großen rechentechnischen Aufwand gewonnen werden. Die nötigen Ressourcen wurden größtenteils durch das Forschungszentrum Jülich bereitgestellt, weshalb ich auch allen Mitarbeitern dieses Rechenzentrum danken möchte.
Auch dem DESY in Zeuthen danke ich für die Bereitstellung der äusserst zuverlässigen Computerkapazitäten die bei der Erstellung der Ergebnisse für diese Arbeit hilfreich und unerlässlich waren. Ebenso möchte ich mich für den angenehmen Arbeitsplatz in der Nähe meines Betreuers bedanken.
Thanks to all the hardworking readers of my manuscript. The positive suggestions from Krzysztof Cichy, Gregorio Herdoíza, Michael Müller-Preußker and especially Karl Jansen helped significantly to improve and complete my thesis.
Zu guter letzt möchte ich mich auch bei meiner Familie bedanken. Ein wesentlicher Teil der Kreativität die ich in dieser Arbeit eingebracht habe, wurde durch den Ausgleich hervorgebracht den mir meine Familie neben der Arbeit gegeben hat. Durch die Verstärkung meiner lieben Frau Bettina konnte ich die nötige Zeit und Ruhe finden, die ich brauchte um diese Arbeit anzufertigen.

# A. Conventions

## A.1. Euclidean gamma matrices

In this work we have chosen to use the gamma matrices in the Chiral representation [1]

$$\gamma_0 = \begin{pmatrix} 0 & -\mathbb{I} \\ -\mathbb{I} & 0 \end{pmatrix} \quad \text{and} \quad \gamma_k = \begin{pmatrix} 0 & -i\sigma_k \\ i\sigma_k & 0 \end{pmatrix}, \tag{A.1}$$

where $\mathbb{I}$ is the $2 \times 2$ unit matrix and $\sigma_{1,2,3}$ are the Pauli matrices in their standard form. The fifth gamma matrix $\gamma_5$ is defined as follows:

$$\gamma_5 = \gamma_0\gamma_1\gamma_2\gamma_3 = \begin{pmatrix} \mathbb{I} & 0 \\ 0 & -\mathbb{I} \end{pmatrix} \tag{A.2}$$

## A.2. Generators of $SU(2)$

The three generators of the $SU(2)$ group are denoted by $\tau^i$, $i = 1, 2, 3$, also often referred to as Pauli matrices.

$$\tau^0 = \begin{pmatrix} 1 & 0 \\ 0 & 1 \end{pmatrix} \tag{A.3}$$

$$\tau^1 = \begin{pmatrix} 0 & 1 \\ 1 & 0 \end{pmatrix} \tag{A.4}$$

$$\tau^2 = \begin{pmatrix} 0 & -i \\ i & 0 \end{pmatrix} \tag{A.5}$$

$$\tau^3 = \begin{pmatrix} 1 & 0 \\ 0 & -1 \end{pmatrix} \tag{A.6}$$

A zeroth Pauli matrix, the $2 \times 2$ identity matrix, has been defined for notational convenience.

[1] This representation is similar to the Weyl basis in Minkowsky space-time.

## A.3. Notation

### A.3.1. Covariant vectors

$$x_\mu = (x_0, x_1, x_2, x_3)^T = (x_0, \vec{x})^T \tag{A.7}$$

$$p_\mu = (p_0, p_1, p_2, p_3)^T = (p_0, \vec{p})^T \tag{A.8}$$

### A.3.2. Covariant unit vectors

It is often convenient to define four-component unit vectors $\hat{\mu}$ and $\hat{k}$.

$$\hat{\mu}_\nu = \delta_{\mu,\nu} = \begin{cases} (1,0,0,0)^T & \nu = 0 \\ (0,1,0,0)^T & \nu = 1 \\ (0,0,1,0)^T & \nu = 2 \\ (0,0,0,1)^T & \nu = 3 \end{cases} \tag{A.9}$$

$$\hat{k}_\nu = \delta_{k,\nu} = \begin{cases} (0,1,0,0)^T & \nu = 1 \\ (0,0,1,0)^T & \nu = 2 \\ (0,0,0,1)^T & \nu = 3 \end{cases} . \tag{A.10}$$

### A.3.3. Fermion fields

If not denoted differently, $\chi$ always describes the Dirac spinors of a doublet of quarks $q_1$ , $q_2$:

$$\chi = \begin{pmatrix} q_1 \\ q_2 \end{pmatrix} \tag{A.11}$$

$$\bar{\chi} = (\bar{q_1}, \bar{q_2}) . \tag{A.12}$$

A superscript $l$ on $\chi$ and $\bar{\chi}$ indicates, that $q_1$ represents the up and $q_2$ the down quark (the light doublet):

$$\chi^l = \begin{pmatrix} u \\ d \end{pmatrix} \tag{A.13}$$

$$\bar{\chi}^l = (\bar{u}, \bar{d}) . \tag{A.14}$$

On the other hand $\chi^h$ and $\bar{\chi}^h$ represent the heavy quark doublet, namely the strange and charm quark:

$$\chi^h = \begin{pmatrix} c \\ s \end{pmatrix} \tag{A.15}$$

$$\bar{\chi}^h = (\bar{c}, \bar{s}) . \tag{A.16}$$

# B. Tables of measured masses and decay constants of pseudoscalar mesons

## B.1. Pion Masses and Decay Constants

| Ensemble | $aM_\pi$ | $af_\pi$ |
|---|---|---|
| A30.32 | 0.12376(45) | 0.06445(36) |
| A40.24 | 0.14475(47) | 0.06570(48) |
| A40.32 | 0.14115(35) | 0.06824(22) |
| A60.24 | 0.17322(43) | 0.07190(24) |
| A80.24 | 0.19905(39) | 0.07554(16) |
| A100.24 | 0.22166(36) | 0.07900(15) |
| B25.32 | 0.10714(45) | 0.05713(41) |
| B35.32 | 0.12511(30) | 0.06094(21) |
| B55.32 | 0.15416(30) | 0.06525(12) |
| B75.32 | 0.18064(36) | 0.06891(16) |
| B85.24 | 0.19290(74) | 0.07013(35) |
| D15.48 | 0.06971(25) | 0.04365(22) |
| D20.48 | 0.08003(24) | 0.04482(18) |
| D30.48 | 0.09808(23) | 0.04726(17) |

Table B.1.: charged pion masses and decay constants determined from the charged pseudoscalar correlator

## B.2. Unitary Kaon and D-meson masses

| Ensemble | $aM_K$ | $aM_D$ |
|---|---|---|
| A30.32 | 0.25150(29) | 0.9230(440) |
| A40.32 | 0.25666(23) | 0.9216(109) |
| A50.32 | 0.26225(38) | 0.9348(173) |
| A60.24 | 0.26695(52) | 0.9298(118) |
| A80.24 | 0.27706(61) | 0.9319(94) |
| A100.24 | 0.28807(34) | 0.9427(99) |
| A80.24s | 0.25503(33) | 0.939(74) |
| A100.24s | 0.26490(74) | 0.9326(431) |
| B35.32 | 0.21840(28) | 0.8286(85) |
| B55.32 | 0.22799(34) | 0.8532(62) |
| B75.32 | 0.23753(32) | 0.8361(127) |
| B85.24 | 0.24392(59) | 0.8524(103) |
| D15.48 | 0.16897(85) | - |
| D30.48 | 0.17760(23) | 0.6731(90) |

Table B.2.: kaon and D-meson masses in the unitary setup (sea-quark action = valence-quark action)

# C. Fit parameters of chiral fits to $\Phi_{D_s}$ and $R_1$

Fits to $\Phi_{D_s}$, formula (3.3a)

| fit label | $D_{1,0}$ $[\frac{3}{2}]$ | $D_{1,m}$ $[\frac{3}{2}]$ | $D_{2,0}$ [0] | $D_{2,m}$ [0] |
|---|---|---|---|---|
| ↓ | $D_{a,0}$ [2] | $D_{a,m}$ [2] | $D_{ah}$ [0] | $D_3$ $[\frac{5}{2}]$ |
| I | 1.88(38) | 0.9(8) | 0.6(8) | -1.3(3.8) |
| | 0.5(4.0) | -3(14) | 0.02(14) | -3.6(1.6) |
| III | 1.84(40) | 1.0(1.0) | 1.4(2.5) | -5(12) |
| | 0(6) | -1(15) | 0.03(20) | -3.6(1.7) |

Fits to $R_1$ with HM-$\chi$PT, formula (3.3b)

| fit label | $D_{1,0}$ $[\frac{1}{2}]$ | $D_{1,m}$ $[\frac{1}{2}]$ | $A_1$ [2] | $A_2$ [1] |
|---|---|---|---|---|
| ↓ | $D_{2,0}$ [0] | $D_{2,m}$ [0] | $D_3$ $[\frac{5}{2}]$ | |
| II | 3.7(9) | 0.1(1.0) | -20(16) | 4.4(3.5) |
| | 0.4(8) | -0.8(4.2) | -0.6(3.8) | |
| IV | 4.7(1.0) | 0.6(1.7) | -7(9) | 1.6(2.0) |
| | 1.5(1.6) | -4(8) | -6.0(4.3) | |

Table C.1.: This table shows the detailed fit parameters of the chiral fits to $\Phi_{D_s}$ (formula (3.3a)) and $R_1$ (formula (3.3b)). All fit parameters have been made dimensionless by multiplication with suitable powers (indicated in square brackets after the parameter label) of $r_0 = 0.47\,\text{fm}$, which is approximatly the value we would obtain from the lattice spacing (2.19a) and a value of $r_0^\chi/a = 5.215$ (the average of the combined pure quadratic fit in table 2.4 and the single-lattice-spacing fit from table 2.5 at $\beta = 1.90$) in chapter 2. As mentioned in the previous chapters, the parameters $D_1$, $D_2$ and $D_a$ are fitted as linear functions in the strange quark mass. Hence, these paramters are related to the corresponding ones in the table through $D_p = D_{p,0} + \xi_{ss} D_{p,m}$, with $p$ being a placeholder for 1,2 or $a$.

# D. Calculation of the error behaviour of $\chi^2_\lambda$

In chapter 4 we defined the weighted $d$-dimensional $\chi^2$ function

$$\chi^2_\lambda = \lambda_1 X_1^2 + \ldots + \lambda_d X_d^2 \,, \tag{D.1}$$

$\lambda_i \geq 0$ being the weights and $X_i$ standard normal random variables. As we will only consider this weighted $\chi^2$-function in this chapter, we will drop the subscript $\lambda$ in the following.
A stochastic approximation $\tilde{\chi}^N$ of $\chi^2$ based on $N$ samples $x^{j=1\ldots N} \in X$ would be expressed as:

$$\chi^2 \approx \tilde{\chi}^2(N) = \frac{1}{N} \sum_{j=1}^{N} \sum_{i=1}^{d} \lambda_i (x_i^j)^2 \tag{D.2}$$

The variance of $\tilde{\chi}^2(N)$ is

$$Var(\tilde{\chi}^2(N)) = E\left((\tilde{\chi}^2(N))^2\right) - E(\tilde{\chi}^2(N))^2 \tag{D.3}$$

This expression can be simplified by using the fact that $\tilde{\chi}^2(N)$ can be expressed as a sum of $\chi^2$ functions but each with an independent set of random variables.

$$\tilde{\chi}^2(N) = \frac{1}{N}\left(\chi_1^2 + \ldots + \chi_N^2\right) \tag{D.4}$$

For a better distinction of the $\chi^2$ functions we have assigned an index to them: $\chi^2 \to \chi^2_k$.
Now D.3 can be expressed as:

$$Var(\tilde{\chi}^2(N)) = E\left(\frac{1}{N^2} \sum_{i,j=1}^{N} \chi_i^2 \chi_j^2\right) - E(\sum_{i=1}^{N} \chi_i^2)^2 \tag{D.5}$$

$$= \frac{1}{N^2} \sum_{i,j=1}^{N} E(\chi_i^2 \chi_j^2) - \frac{1}{N^2}\left(\sum_{i=1}^{N} E(\chi_i^2)\right)^2 \,. \tag{D.6}$$

The expectation value of $\chi_i^2$ is:

$$E(\chi_i^2) \overset{\forall i}{=} E(\chi^2) = \sum_{j=1}^{d} \lambda_j E(X_j^2) = \sum_{j=1}^{d} \lambda_j \,, \tag{D.7}$$

as $E(X_j^2) \overset{\forall j}{=} 1$ for standard normal random variables. Furthermore we need to calculate

$E((\chi^2_K)^2)$:

$$E((\chi^2_k)^2) \overset{\forall k}{=} E\left((\chi^2)^2\right) \tag{D.8}$$

$$= \sum_{i,j=1}^{d} \lambda_i \lambda_j E(X_i^2 X_j^2) \tag{D.9}$$

$$= \sum_{i,j=1} \lambda_i \lambda_j E(X_i^2) E(X_j^2) - \sum_{i=1}^{d} \lambda_i^2 E(X_i)^2 + \sum_{i=1}^{d} \lambda_i^2 E(X_i^4) \tag{D.10}$$

$$= \left(\sum_{i=1}^{d} \lambda_i\right)^2 - \sum_{i=1}^{d} \lambda_i^2 + 3\sum_{i=1}^{d} \lambda_i^2 \tag{D.11}$$

$$= \left(\sum_{i=1}^{d} \lambda_i\right)^2 + 2\sum_{i=1}^{d} \lambda_i^2 = E(\chi^2)^2 + 2\sum_{i=1}^{d} \lambda_i^2 \,, \tag{D.12}$$

where we have used that $E(O_1 O_2) = E(O_1)E(O_2)$ if $O_{1,2}$ are two statistically independent variables (possibly constructed from other random variables) and that $E(X^4) = 3$ for a standard normal random variable. Using (D.7) and (D.12) to evaluate (D.6) we find

$$Var(\tilde{\chi}^2(N)) = \frac{1}{N^2}\left(\sum_{i,j=1}^{N} E(\chi_i^2)E(\chi_j^2) - \sum_{i=1}^{N} E(\chi_i^2)^2 + \sum_{i=1}^{N} E(\chi_i^2)\right) - \frac{1}{N^2}\left(NE(\chi^2)\right)^2 \tag{D.13}$$

$$= \frac{1}{N^2}\left(N^2 E(\chi^2)^2 - NE(\chi_i)^2 + NE(\chi^2)^2 + N2\sum_{i=1}^{d} \lambda_i^2\right) - \frac{1}{N^2}\left(NE(\chi^2)\right)^2 \tag{D.14}$$

$$= \frac{2\sum_{i=1}^{d} \lambda_i^2}{N} \,. \tag{D.15}$$

Thus, we see that the error of $\tilde{\chi}^2(N)$, which is the square root of the variance, is proportional to $\frac{1}{\sqrt{N}}$. This result is basically the same for any other probability distribution of the variables $X$ and the conditions $E(X) = 0$ and $E(X^2) = 1$. The only difference is the numerical factor "2" in D.15 which is in general $E(X^4) - 1$ and can be even zero in some special cases.

# List of Figures

1.1. Maximally allowed ratio $\chi^2$/dof for confidence levels (diamond symbols) of 95% (black) , 68% (orange) and 50% (blue). $\chi^2$/dof = 1 is shown as open circles. . . . . 26

2.1. We show the plots of the chiral fits of $r_0$ for the linear fit (see text). The circle symbols correspond to the measured data whereas the star symbol represents the chirally extrapolated value of $r_0$. **(upper-left)** : combined fit of all lattice spacings → as shown in table 2.4 ; The remaining three plots correspond to the fits with a single lattice spacing (as in table 2.5). **(upper-right)** : $\beta = 1.90$ ; **(lower-left)** : $\beta = 1.95$ ; **(lower-right)**: $\beta = 2.10$ . . . . . 43

2.2. These plots show the chiral fits of $r_0$ for the quadratic fit *without* the linear term. The circle symbols correspond to the measured data whereas the star symbol represents the chirally extrapolated value of $r_0$. **(upper-left)** : combined fit of all lattice spacings → as shown in table 2.4 ; The remaining three plots correspond to the fits with a single lattice spacing (as in table 2.5). **(upper-right)** : $\beta = 1.90$ ; **(lower-left)** : $\beta = 1.95$ ; **(lower-right)**: $\beta = 2.10$ . . . . . 44

2.3. The chiral fits of $r_0$ of the quadratic kind *including* the linear term are displayed in these plots. The circle symbols correspond to the measured data whereas the star symbol represents the chirally extrapolated value of $r_0$. **(upper-left)** : combined fit of all lattice spacings → as shown in table 2.4 ; The remaining three plots correspond to the fits with a single lattice spacing (as in table 2.5). **(upper-right)** : $\beta = 1.90$ ; **(lower-left)** : $\beta = 1.95$ ; **(lower-right)**: $\beta = 2.10$ . . . . . 45

2.4. The ratio of the first excited state contribution to the statistical error on the correlator (for ensemble B25.32, see criterion in formula (2.9)). This illustrates the selection of $x_0^{min}$, the optimal starting time slice for the extraction of the pion mass and decay constant from the pseudoscalar correlator. The black line corresponds to a ratio of 0.2. In this specific case $x_0^{min} = 11$ has been determined. . . . . 46

2.5. The error of the pion mass (left) and decay constant (right) as a function of the block size (x-axis) in the blocked bootstrap analysis (ensemble B25.32). 47

2.6. The curves show the chiral fit describing the charged pion **decay constant** for fit **I**. The symbol shapes correspond to the lattice spacings as follows: **circle** $\rightarrow \beta = 1.90$, **triangle** $\rightarrow \beta = 1.95$, **cross** $\rightarrow \beta = 2.10$. The **star** symbol represents the physical point. **Gray** and **blue** symbols refer to the original data and the finite-volume corrected data respectively. The black symbols are finite-volume corrected with discretisation effects taken into account with a term proportional to $a^2$. The remaining discretisation effects only stem from the $a^2$ term in the LO neutral pion mass. The dashed ($\beta = 1.90$), dotted ($\beta = 1.95$) and dash-dotted ($\beta = 2.10$) curves represent the predictions of twisted mass Wilson $\chi$PT at finite lattice spacing. The solid curve shows the continuum $\chi$PT prediction (extrapolation). Look at table 2.9 for numerical results. . . . . 48
2.7. The notation is the same as in figure 2.6 with the only difference that the pion mass (respectively its square scaled with $\chi_\mu$) is shown. . . . . 49
2.8. Chiral fits for fit **II**, for details see description of figures 2.6 and 2.7 . . . . 50
2.9. Chiral fits for fit **III**, for details see description of figures 2.6 and 2.7 . . . 50
2.10. Chiral fits for fit **IV**, for details see description of figures 2.6 and 2.7 . . . 51

3.1. Kaon and D-meson masses determined on our ensembles as a result of the strange and charm quark mass tuning . . . . . 55
3.2. Kaon masses determined from ensemble A40.32 in the mixed action setup for various strange quark masses, enclosing the region of the physical kaon/strange mass, **x-axis:** unrenormalised strange quark mass in lattice units as given in table 3.2, **y-axis:** measured kaon mass in physical units, **dashed line:** experimental kaon mass, bracketed by the points at $am_s = 0.015$ and $am_s = 0.017$ . . . . . 57
3.7. Comparison of our result for $f_{D_s}$ with others obtained with the same or less numbers of sea quark flavours from lattice-QCD: [4] ($N_f = 2$, ETMC, 2009), [5] ($N_f = 2 + 1$, HPQCD collaboration, 2010), [40] ($N_f = 2 + 1 + 1$, Fermilab/MILC collaborations, 2013, preliminary results) and experimental average from PDG [6] . . . . . 62
3.3. The curves are the results for the chiral fit of $\Phi_{D_s}$ (described by formula (3.3a)) with pion masses up to $\approx 485MeV$. We note, that all data points and the describing fit funtion have been multiplied with $\sqrt{M_{D_s}^{\text{phys}}}$, such that the y-axis is in units of $f_{D_s}$. The circle, triangle and cross symbols represent the fitted data points at the corresponding value of $\beta$ as indicated in the legend. The dashed ($\beta = 1.9$), the dotted ($\beta = 1.95$) and the dash-dotted ($\beta = 2.1$) line show the predictions at finite lattice spacing whereas the solid black line stands for the continuum prediction which leads at the physical pion mass to the extrapolation result for $f_{D_s}$ depicted by the asterisk symbol (with error bars accounting for statistical errors). The experimental point from the 2012 revision [6] of the PDG average is shown as the diamond symbol, and the grey shaded area is the overall uncertainty of the experimental average. . . . . 63

3.4. The chiral fit of $R_1$ corresponding to formulae (3.3b) (blue curve) ( $M_\pi \leq 485MeV$). The meaning of the symbols is as in the previous figure 3.3. The dashed, dotted and dash-dotted curves represent the prediction of formula (3.3b) at finite lattice spacing, $\beta = 1.9;\ 1.95;$ and 2.1 in this order. The continuum prediction for $R_1$ is shown as the blue asterisk. The black asterisk symbol with dashed error bars represents the continuum extrapolation result from the fit to formulae (3.3a) (shown in figure 3.3 ). Both asterisk symbols are supposed to lie at the physical pion mass marked by the grey dashed vertical line at $\frac{M_\pi^2}{(M_\pi^{\mathrm{phys}})^2} = 1$. Only the black point has been slightly set off from this line for a better visibility. . . . . 64
3.5. These curves show the fit results for $\Phi_{D_s}$ with pion masses only up to $\approx 380MeV$. The notation is as in the description of figure 3.3, where the fit was performed with pion masses up to 485MeV. . . . . 65
3.6. The chiral fit of $R_1$ corresponding to formulae (3.3b) (blue curve) with pion masses $M_\pi \leq 380MeV$. Notation is as in the description of figure 3.4 where the same fit was performed with pion masses up to 485MeV. . 66

4.1. **Left:** 512 rice seeds thrown (pseudo)randomly onto a square of edge length 1, subdivided into $8 \times 8$ equal smaller squares, each colour corresponds to the number of seeds contained in the square; **right:** histogram, showing the number of squares with a certain number of seeds, colour code corresponding to figure on the left . . . . . 69
4.2. Poisson distribution for the expectation value $\bar{n} = 8$ . . . . . 70
4.3. The same experiment as shown in figure 4.1 but with (deterministic) quasi-Monte Carlo samples, for further explanation see description, figure 4.1 . . . . . 71
4.4. Results of a similar experiment as shown in figures 4.1 and 4.3 but with a partitioning of $13 \times 13$ squares and 507 seeds in total, **left:** conventional pseudo-random sampling, **right:** QMC sampling, (take into acount the different scales on the y-axis in both plots, see also description of figure 4.1) . . . . . 72
4.5. Comparison of the asymptotic error scaling of $\langle X^2 \rangle$ for the QMC and MC aproach at the example of the harmonic oscillator, see text for further description . . . . . 78
4.6. The error of the observables $X^2$ (left) and $E_0$ (right) as a function of $N$, the number of samples, for the anharmonic oscillator. The dashed line (double-log plot) represents a fit describing the errors with the model $CN^\alpha$. Detailed results are listed in table 4.1. . . . . 81

# List of Tables


1.1. This table shows the mapping of mesons to quark mass values $\mu_1$ and $\mu_2$ in the valence quark action (1.16). $m_{up/down}$, $m_{strange}$ and $m_{charm}$ correspond to the up/down, strange and charm quark mass. . . . . 17

2.1. The three $\beta$-values used in our lattice simulations and the approximate lattice spacing . . . . . 31
2.2. This table shows the set of simulated ensembles used for the scale determination in the pion sector. Columns two to five contain the simulation parameters, whereas columns six and seven contain the approximate pion mass (rounded to units of 5 MeV) and lattice size in units of the Compton wavelength of the pion. . . . . 32
2.3. The table shows the measured values of the Sommer scale $r_0$ for each ensemble in lattice units. . . . . 33
2.4. Shown are the results for global fits of $r_0$ to formula (2.1) on all lattice spacings simultaneously. The first data column ("linear") shows results for a linear fit in $x$ ($h_2$ set to zero). The following column ("quadratic") shows a pure quadratic fit ($h_1$ set to zero); and the last column ("both") investigates the case where $h_1$ and $h_2$ are free fit parameters. Instead of $r_0^\chi(\beta = 1.95)$ and $r_0^\chi(\beta = 2.10)$ we give the ratios $R_{1,2} = \frac{r_0^\chi(\beta=1.90)}{r_0^\chi(\beta=1.95,2.10)}$ . . 34
2.5. The table shows fits of $r_0$ performed separately for each lattice spacing. The second column indicates the applied fit ansatz (see description table 2.4). As in Table 2.4 we have given the ratios $R_1$ and $R_2$ for $\beta = 1.95$ and $\beta = 2.10$ formed from $r_0^\chi$ values obtained from the same type of fit. Braces indicate statistical errors calculated from 100 bootstrap samples. . 35
2.6. Values used for the pseudoscalar current renormalisation constant $Z_P$ for the three lattice spacings, required for the renormalised light quark mass $\mu^R = \frac{\mu_l}{Z_P}$ . . . . . 38
2.8. This table shows an overview of the pion mass cuts we applied to our data in the chiral fits. In the second column we list the ensembles we used for a certain fit. The third column shows the corresponding fit labels, referred to in the discussion. . . . . 39
2.9. Results of the chiral fits are shown for four different pion mass cuts. See table 2.8 for the list of ensembles used. . . . . 40

3.1. Parameters of $\mu_\sigma$ and $\mu_\delta$ used in our simulations for the different values of $\beta$ . . . . . 54

3.2. Strange quark masses $\mu_s$ in lattice units used for the measurement of kaon and $D_s$ meson correlators . . . . . 56
3.3. Charm quark masses $\mu_c$ in lattice units used for the measurement of $D_s$ meson correlators . . . . . 58
3.5. Fit results of the chiral fits to $\Phi_{D_s} = f_{D_s}\sqrt{M_{D_s}}$ and $R_1 = \frac{\Phi_{D_s}}{f_K}$ and extrapolation result in the continuum for $f_{D_s}$. . . . . 60

4.1. Results for the error scaling of the observalbes $X^2$, $X^4$ and $E_0$ for the model of the anharmonic oscillator, simulated through reweighting, observable errors fitted to the model $\sim CN^\alpha$. . . . . 80

B.1. charged pion masses and decay constants determined from the charged pseudoscalar correlator . . . . . 91
B.2. kaon and D-meson masses in the unitary setup (sea-quark action = valence-quark action) . . . . . 92

C.1. This table shows the detailed fit parameters of the chiral fits to $\Phi_{D_s}$ (formula (3.3a)) and $R_1$ (formula (3.3b)). All fit parameters have been made dimensionless by multiplication with suitable powers (indicated in square brackets after the parameter label) of $r_0 = 0.47\,\mathrm{fm}$, which is approximatly the value we would obtain from the lattice spacing (2.19a) and a value of $r_0^\chi/a = 5.215$ (the average of the combined pure quadratic fit in table 2.4 and the single-lattice-spacing fit from table 2.5 at $\beta = 1.90$) in chapter 2. As mentioned in the previous chapters, the parameters $D_1$, $D_2$ and $D_a$ are fitted as linear functions in the strange quark mass. Hence, these paramters are related to the corresponding ones in the table through $D_p = D_{p,0} + \xi_{ss} D_{p,m}$, with $p$ being a placeholder for 1,2 or $a$. . . . . 93

# Bibliography


[1] O. Bär, "Chiral logs in twisted mass lattice QCD with large isospin breaking," *Phys.Rev.* **D82** (2010) 094505, arXiv:1008.0784 [hep-lat].

[2] **ETM** Collaboration, R. Baron *et al.*, "Light hadrons from Nf=2+1+1 dynamical twisted mass fermions," *PoS* **LATTICE 2010** (2010) 123, arXiv:1101.0518 [hep-lat].

[3] S. Borsányi, S. Dürr, Z. Fodor, S. Krieg, A. Schäfer, E. E. Scholz, and K. K. Szabó, "SU(2) chiral perturbation theory low-energy constants from 2+1 flavor staggered lattice simulations," *Phys.Rev.* **D88** (2013) 014513, arXiv:1205.0788 [hep-lat].

[4] **ETM** Collaboration, B. Blossier *et al.*, "Pseudoscalar decay constants of kaon and D-mesons from $N_f = 2$ twisted mass Lattice QCD," *JHEP* **0907** (2009) 043, arXiv:0904.0954 [hep-lat].

[5] **HPQCD** Collaboration, C. Davies, C. McNeile, E. Follana, G. Lepage, H. Na, *et al.*, "Update: Precision $D_s$ decay constant from full lattice QCD using very fine lattices," *Phys.Rev.* **D82** (2010) 114504, arXiv:1008.4018 [hep-lat].

[6] **Particle Data Group** Collaboration, J. Beringer *et al.*, "Decay Constants of Charged Pseudoscalar Mesons," *Phys.Rev.* **D86** (2012) 010001. http://pdg.lbl.gov. second revised version of [53].

[7] G. Colangelo, S. Dürr, A. Juttner, L. Lellouch, H. Leutwyler, *et al.*, "Review of lattice results concerning low energy particle physics," *Eur.Phys.J.* **C71** (2011) 1695, arXiv:1011.4408 [hep-lat].

[8] R. Frezzotti and G. Rossi, "Chirally improving Wilson fermions. 1. O(a) improvement," *JHEP* **0408** (2004) 007, arXiv:hep-lat/0306014 [hep-lat].

[9] R. Frezzotti, G. Martinelli, M. Papinutto, and G. Rossi, "Reducing cutoff effects in maximally twisted lattice QCD close to the chiral limit," *JHEP* **0604** (2006) 038, arXiv:hep-lat/0503034 [hep-lat].

[10] A. Shindler, "Twisted mass lattice QCD," *Phys.Rept.* **461** (2008) 37–110, arXiv:0707.4093 [hep-lat].

[11] Y. Iwasaki, "Renormalization Group Analysis of Lattice Theories and Improved Lattice Action: Two-Dimensional Nonlinear O(N) Sigma Model," *Nucl.Phys.* **B258** (1985) 141–156.

[12] **ETM** Collaboration, R. Baron *et al.*, "Computing K and D meson masses with $N_f = 2+1+1$ twisted mass lattice QCD," *Comput.Phys.Commun.* **182** (2011) 299–316, arXiv:1005.2042 [hep-lat].

[13] R. Frezzotti and G. Rossi, "Chirally improving Wilson fermions. II. Four-quark operators," *JHEP* **0410** (2004) 070, arXiv:hep-lat/0407002 [hep-lat].

[14] H. J. Rothe, *Lattice Gauge Theories*, vol. 74. World Scientific Lecture Notes in Physics, 2005.

[15] J. G. López, "Cutoff effects and continuum limit at tree-level of perturbation theory for wilson twisted mass fermions at maximal twist," 2007. PhD Thesis Preparation Report.

[16] K. Jansen, H. Leovey, A. Ammon, A. Griewank, and M. Müller-Preussker, "Quasi-Monte Carlo methods for lattice systems: a first look," arXiv:1302.6419 [hep-lat]. accepted for publication in Comput.Phys.Commun.

[17] F. Kuo, C. Schwab, and I. Sloan, "Quasi-monte carlo methods for high-dimensional integration: the standard (weighted hilbert space) setting and beyond," *ANZIAM Journal* **53** no. 0, (2012) 1–37. http://journal.austms.org.au/ojs/index.php/ANZIAMJ/article/view/5230.

[18] P. L'Ecuyer and C. Lemieux, "Recent advances in randomized quasi-monte carlo methods," in *Modeling Uncertainty*, M. Dror, P. L'Ecuyer, and F. Szidarovszky, eds., vol. 46 of *International Series in Operations Research & Management Science*, pp. 419–474. Springer US, 2005. http://dx.doi.org/10.1007/0-306-48102-2_20.

[19] R. Sommer, C. Alexandrou, F. Jegerlehner, S. Güsken, and K. Schilling, "A Scaling analysis of heavy - light meson properties," *Nucl.Phys.Proc.Suppl.* **26** (1992) 387–390.

[20] T. DeGrand and C. E. Detar, *Lattice methods for quantum chromodynamics*. World Scientific, 2006.

[21] **Budapest-Marseille-Wuppertal** Collaboration, S. Dürr, Z. Fodor, C. Hoelbling, S. Krieg, T. Kurth, *et al.*, "Lattice QCD at the physical point meets SU(2) chiral perturbation theory," arXiv:1310.3626 [hep-lat].

[22] H. Leutwyler, "Nonlattice determinations of the light quark masses," *Nucl.Phys.Proc.Suppl.* **94** (2001) 108–115, arXiv:hep-ph/0011049 [hep-ph].

[23] G. Colangelo and S. Dürr, "The Pion mass in finite volume," *Eur.Phys.J.* **C33** (2004) 543–553, arXiv:hep-lat/0311023 [hep-lat].

[24] **ETM** Collaboration, G. Herdoíza, K. Jansen, C. Michael, K. Ottnad, and C. Urbach, "Determination of Low-Energy Constants of Wilson Chiral Perturbation Theory," *JHEP* **1305** (2013) 038, arXiv:1303.3516 [hep-lat].

[25] **ETM** Collaboration, B. Blossier, V. Lubicz, C. Tarantino, and S. Simula, "Pseudoscalar meson decay constants f(K), f(D) and f(D(s)), from N(f) = 2 twisted mass Lattice QCD," *PoS* **LATTICE 2008** (2008) 285, arXiv:0810.3145 [hep-lat].

[26] **ALPHA** Collaboration, U. Wolff, "Monte Carlo errors with less errors," *Comput.Phys.Commun.* **156** (2004) 143–153, arXiv:hep-lat/0306017 [hep-lat].

[27] H. Flyvbjerg and H. Petersen, "Error estimates on averages of correlated data," *J. Chem. Phys.* **91** (1989) 461.

[28] R. G. Miller, "The jackknife - a review," *Biometrika* **61** no. 1, (1974) 1–15.

[29] B. Efron and R. Tibshirani, "Bootstrap methods for standard errors, confidence intervals, and other measures of statistical accuracy," *Statistical science* (1986) 54–75.

[30] D. W. Marquardt, "An algorithm for least-squares estimation of nonlinear parameters," *Journal of the Society for Industrial and Applied Mathematics* **11** (1963) 431–441.

[31] **ALPHA** Collaboration, P. Fritzsch, F. Knechtli, B. Leder, M. Marinković, S. Schäfer, *et al.*, "The strange quark mass and Lambda parameter of two flavor QCD," *Nucl.Phys.* **B865** (2012) 397–429, arXiv:1205.5380 [hep-lat].

[32] S. Capitani, M. Della Morte, G. von Hippel, B. Knippschild, and H. Wittig, "Scale setting via the $\Omega$ baryon mass," *PoS* **LATTICE2011** (2011) 145, arXiv:1110.6365 [hep-lat].

[33] M. Luscher, "Properties and uses of the Wilson flow in lattice QCD," *JHEP* **1008** (2010) 071, arXiv:1006.4518 [hep-lat].

[34] **ETM** Collaboration, R. Baron, P. Boucaud, J. Carbonell, A. Deuzeman, V. Drach, *et al.*, "Light hadrons from lattice QCD with light (u,d), strange and charm dynamical quarks," *JHEP* **1006** (2010) 111, arXiv:1004.5284 [hep-lat].

[35] **ETM** Collaboration, K. Ottnad *et al.*, "$\eta$ and $\eta'$ mesons from $N_f = 2 + 1 + 1$ twisted mass lattice QCD," *JHEP* **1211** (2012) 048, arXiv:1206.6719 [hep-lat].

[36] **ETM** Collaboration, C. Alexandrou, M. Constantinou, V. Drach, K. Jansen, C. Kallidonis, *et al.*, "Nucleon generalized form factors with twisted mass fermions," arXiv:1312.2874 [hep-lat].

[37] **Particle Data Group** Collaboration, K. Nakamura *et al.*, "Decay Constants of Charged Pseudoscalar Mesons," *JPG* **37** (2010) 075021. http://pdg.lbl.gov. revised version of [53].

[38] **Particle Data Group** Collaboration, J. Beringer *et al.*, "Review of Particle Physics (RPP)," *Phys.Rev.* **D86** (2012) 010001. `http://pdg.lbl.gov`.

[39] **ETM** Collaboration, R. Baron *et al.*, "First results of ETMC simulations with N(f) = 2+1+1 maximally twisted mass fermions," *PoS* **LATTICE 2009** (2009) 104, `arXiv:0911.5244 [hep-lat]`.

[40] **Fermilab lattice and MILC** Collaboration, C. Bernard, J. Kim, J. Komijani, D. Toussaint, *et al.*, "$D$ and $D_s$ decay constants from a chiral analysis on `HISQ` ensembles," *Proceedings of Science* . Talk presented at 31. International Symposium on Lattice Field Theory.

[41] M. Lüscher, "Local coherence and deflation of the low quark modes in lattice QCD," *JHEP* **0707** (2007) 081, `arXiv:0706.2298 [hep-lat]`.

[42] G. Katz, G. Batrouni, C. Davies, A. S. Kronfeld, P. Lepage, *et al.*, "Fourier Acceleration. 2. Matrix Inversion and the Quark Propagator," *Phys.Rev.* **D37** (1988) 1589.

[43] I. M. Sobol', "The distribution of points in a cube and the approximate evaluation of integrals," *U.S.S.R. Comput. Math. and Math. Phys.* **7** no. 4, (1967) 86–112.

[44] S. Joe and F. Y. Kuo, "Remark on algorithm 659: Implementing sobol's quasirandom sequence generator," *ACM Trans. Math. Softw.* **29** no. 1, (Mar., 2003) 49–57. `http://doi.acm.org/10.1145/641876.641879`.

[45] S. Joe and F. Y. Kuo, "Constructing sobol sequences with better two-dimensional projections," *SIAM J. Sci. Comput.* **30** no. 5, (Aug., 2008) 2635–2654. `http://dx.doi.org/10.1137/070709359`.

[46] M. Creutz and B. Freedman, "A STATISTICAL APPROACH TO QUANTUM MECHANICS," *Annals Phys.* **132** (1981) 427.

[47] M. Matsumoto and T. Nishimura, "Mersenne twister: a 623-dimensionally equidistributed uniform pseudo-random number generator," *ACM Trans. Model. Comput. Simul.* **8** no. 1, (Jan., 1998) 3–30. `http://doi.acm.org/10.1145/272991.272995`.

[48] A. M. Ferrenberg and R. H. Swendsen, "New monte carlo technique for studying phase transitions," *Phys. Rev. Lett.* **61** (Dec, 1988) 2635–2638. `http://link.aps.org/doi/10.1103/PhysRevLett.61.2635`.

[49] C. Gattringer and C. B. Lang, "Quantum chromodynamics on the lattice," *Lect.Notes Phys.* **788** (2010) 1–343.

[50] A. Ammon, T. Hartung, K. Jansen, H. Leovey, A. Griewank, and M. Müller-Preussker, "Applicability of quasi-monte carlo for lattice systems," *Proceedings of Science* . In preparation, Talk presented at 31. International Symposium on Lattice Field Theory, 2013.

[51] R. Blankenbecler, T. A. DeGrand, and R. L. Sugar, "Moment Method for Eigenvalues and Expectation Values," *Phys.Rev.* **D21** (1980) 1055.

[52] W. Bietenholz, U. Gerber, M. Pepe, and U.-J. Wiese, "Topological Lattice Actions," *JHEP* **1012** (2010) 020, `arXiv:1009.2146 [hep-lat]`.

[53] **Particle Data Group** Collaboration, J. L. Rosner and S. Stone, "Decay Constants of Charged Pseudoscalar Mesons," `arXiv:0802.1043 [hep-ex]`.